ABSTRACT

Title of Dissertation: DIRECT AND LARGE-EDDY SIMULATION AND ANALYSIS OF SHOCK-SEPARATED FLOWS

Clara M. Helm
Doctor of Philosophy, 2021

Dissertation Directed by: Professor M. Pino Martín
Department of Aerospace Engineering

The in-house CRoCCo code is used to generate a database of high-fidelity direct numerical simulation (DNS) and large eddy simulation (LES) data of shock wave and turbulent boundary layer interactions (STBLI) at supersonic to hypersonic conditions. The DNS data is employed in the validation of the LES method and the assessment of the sub-grid-scale (SGS) models in application to the STBLI flow problem. It is determined that, under hypersonic conditions, a scale similar model term in both the shear stress and heat transfers SGS terms is necessary to produce the correct STBLI separation flow. The use of the dynamic eddy viscosity term alone produced as much as 30% error in separation length. The high grid-resolving efficiency (equivalently the practicality over the DNS) of the CRoCCo code LES method for the simulation of STBLI flows is also demonstrated with a typical reduction of 95% grid size and 67% in number of time steps as compared to the DNS, a feature that makes spectral convergence of the STBLI low-frequency cycle feasible.

The thorough documentation of DNS-validated, high-fidelity LES solutions of hypersonic STBLI flows is a unique contribution of this work. Thanks to the detail in the turbulence data afforded by the LES, an extensive and novel characterization of the sepa-

ration shear layer in the STBLI flows is possible and the results are related to compressible mixing layer theory. In addition, visualizations of the numerical data show the form of the inviscid instability in hypersonic shock-separated flows. These visualizations combined with the extended CRoCCo Lab numerical database provide significant insight into the nature of the separation length scaling in STBLI at hypersonic Mach numbers.

DIRECT AND LARGE-EDDY SIMULATION DATA AND ANALYSIS OF SHOCK-SEPARATED FLOWS

by

Clara M. Helm

Dissertation submitted to the Faculty of the Graduate School of the
University of Maryland, College Park in partial fulfillment
of the requirements for the degree of
Doctor of Philosophy
2021

Advisory Committee:
Professor M. Pino Martìn, Chair/Advisor
Professor James Baeder
Professor Johan Larsson, Dean's Representative
Professor Stuart J. Laurence
Professor Kenneth Yu

Acknowledgments

It is not possible for me to properly thank or acknowledge in this short space all the people in my life, past and present, who have positively influenced what is essentially a documentation of my life's work as it is. I would like to, instead, acknowledge here only those individuals who have played a direct part in making the completion of this, my Ph.D. dissertation, possible. This starts first and foremost with my adviser Dr. Pino Martin. All of the research contained herein stands on her scientific achievements, abilities, and vision, and it is my hope that, thanks to her guidance, this thesis will evince the same traits in my own work. I would also like to thank several labmates from the CRoCCo Lab whose timely advice and input may very well have made the difference between success or failure in my ability to complete the research contained in this dissertation. These are Stephan Priebe, Nathan Grube, and Owen Williams. I am also indebted to two talented high school inters, Amelia Heesen and Sofia Gonzalez-Kosasky, who have provided much assistance in developing several of the visualizations included in this work. I must also acknowledge those who supported my research financially with special thanks to Dr. Michael Kendra and Dr. Ivett Leyva from the AFOSR, and also Dr. John Lafferty and Dr. Eric Marineau with the AEDC CoTE. And lastly, I would like to thank the committee members for your time and effort you have afforded to review this thesis. Your expert feedback is essential for the overall quality of this work and is greatly appreciated.

Table of Contents

List of Tables

List of Figures

Chapter 1: Introduction

1.1 Motivation

In the practical design of aerospace vehicles, the simultaneous occurrence of both turbulent boundary layers and compression shock waves is an all but unavoidable phenomenon. The shock and turbulent boundary layer interaction (STBLI) is a nontrivial engineering challenge for several reasons. First, the shock produces large step changes in both pressure and temperature on the vehicle surface. These step changes increase significantly with Mach number. This problem is exaggerated in the case of separated STBLI by the occurrence of a low-frequency unsteadiness in the separated region causing the foot of the shock to oscillate in the streamwise direction with rather large excursions from its time averaged location (among many references, see for example [1, 2, 3]). The resulting fluctuations in both the pressure and heat loads on the vehicle surface can lead to catastrophic structure failures [4, 5, 6].

This problem is further complicated by the fact that practical engineering simulation methods such as Reynolds Averaged Navier Stokes (RANS) methods are notoriously unreliable for simulating separated STBLI and can produce large errors in both the separation length [7] and wall heat transfer [8]. In addition, the accuracy of heat transfer prediction relations that are largely applicable in the supersonic condition, such as the Reynolds Analogy relating the heat transfer to the shear stress, is uncertain at higher

Mach number conditions [8, 9, 10]. The primary reason for the failure of these simulation and scaling techniques is the fact that there are many complex phenomena associated with the STBLI that are not fully understood, and as a result, the assumptions made in the development of the turbulence models and scaling methods do not correctly represent the physics of the turbulence. Such phenomena include the mechanism involved in producing the strong amplification of the turbulence across the shock, the turbulence behaviors that determine the heat transfer rates at the wall, the dynamics and form of the unstable low-frequency mode that occurs in the separated condition, and the effects of compressibility on the development of the separation shear layer.

The past several decades has seen a large amount of research on the STBLI flow at freestream Mach numbers in the range of 1.5-5, predominantly Mach 2 and 3. Out of these efforts have come many significant contributions towards improving our understanding of this complex flow and in particular the nature of the low-frequency unsteadiness. Our understanding of the low-frequency unsteadiness in separated STBLI has advanced considerably concerning the variation in frequency content through the interaction (among many references see [11, 12] and review articles [1, 10, 13]), scaling of the mean separation length [14, 15], influences by both the upstream [16, 17, 18] and downstream [12, 19, 20, 21, 22, 23, 24], and the identification of the inviscidly unstable nature of the flow [12, 22, 25].

The extrapolation of our knowledge of the supersonic STBLI flow into the hypersonic regime is largely uncertain as hypersonic conditions introduce additional complexity to the STBLI flow. Figure 1.1 shows diagrams of a typical supersonic, ramp-generated separated STBLI flow compared to its hypersonic counterpart. Because of the higher Mach number, the shocks produced by the flow deflection are at a much shallower angle

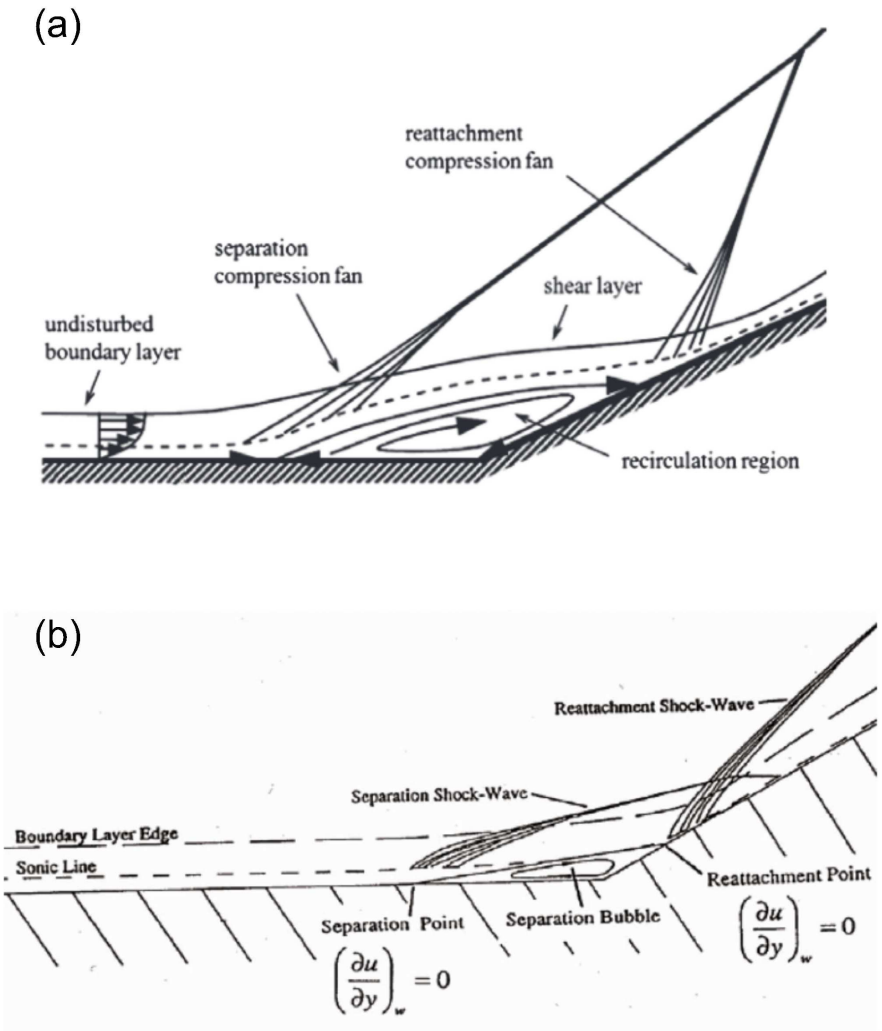

Figure 1.1: Schematic of a compression ramp STBLI flow at (a) supersonic conditions (reproduced from [26]) and (b) hypersonic conditions (reproduced from [27]).

increasing the spatial extent of the interaction between the incoming turbulence and the shock front. The diagram shows that the initial separation shock remains embedded in the incoming turbulence and, unlike in the supersonic case, reflects off of the ramp surface. Large fluctuations in pressure and temperature occur on the surface at this point of shock reflection. In addition, the hypersonic STBLI experiences a much greater strength of pressure jump across the shock. In supersonic STBLI, at say Mach 3, the pressure jump across the shock is on the order of a few times the upstream static pressure, whereas for hypersonic conditions at say Mach 10, the pressure jump can easily be an order of magnitude greater. Compressibility effects such as the occurrence of shocklets in the turbulence are also more prevalent at higher Mach number. At high enthalpy conditions, physical-chemical processes can alter the turbulence.

In order to advance the state of the art in hypersonic vehicle design, new sophisticated numerical methods and novel experimental techniques capable of accommodating the increased complexity of the hypersonic regime must be developed. This necessarily requires an improved understanding of the fundamental physics involved in hypersonic STBLI. For this effort, there is an undeniable need for high fidelity turbulence data, both experimental and numerical, of basic canonical STBLI configurations at hypersonic conditions. Only high-fidelity turbulence data can reveal the details in the turbulence necessary for the identification of the energetically important physics and provide a reliable reference point against which turbulence models and scaling derivations can be tested. It is also essential that classic canonical configurations such as the two-dimensional compression wedge, reflected shock, or the axi-symmetric cylinder with flare be studied as these configurations produce STBLI data at the most simplified level without three-dimensional flow effects clouding the interpretation of the data [28]. The simultaneous availability of

both experimental and numerical data at the same flow conditions and Reynolds number is also essential for cross-validation of results [1, 10, 29, 30].

1.2 Background

Currently, there are a only a few experimental studies of turbulent shock and boundary layer interactions in the hypersonic regime ($M > 5$) and even fewer reporting turbulence data. Settles & Dodson [31, 32, 33] and later Roy & Blottner [8] have provided reviews of the available hypersonic STBLI experimental datasets. Only a fraction of the available datasets were identified as having error margins sufficient for use as reference for turbulence model validation.

High fidelity simulation methods such as Large Eddy Simulation (LES) and Direct Numerical Simulation (DNS) are ideal for the investigation of turbulence statistics because they produce a three-dimensional flowfield that is resolved in both time and space. Very few DNS of fully turbulent STBLI exist in the literature and two notable studies are mentioned here. In a recent article, Priebe & Martin [34] used DNS to reproduce the experimental conditions of Bookey *et al.* [35] of an attached Mach 7 freestream over an 8^o compression wedge. Details of the turbulence through the interaction and heat transfer data were reported. The DNS showed good qualitative comparison with experimental visualizations of Bookey *et al.* [35]. Volpiani *et al.* [36] used DNS to generate data of reflected shock conditions at freestream of Mach 5. Comparison with experimental wall pressure, skin friction, and wall heat transfer data from Schülein [9] showed that the DNS produced a significantly smaller separation size. The authors explained the difference by noting that there could be as much as 20% uncertainty in the experimental separation length due to possible three-dimensional flow effects from the test article. So far, the DNS

method has been much more widely used for studying laminar hypersonic shock boundary layer interactions [25, 37, 38, 39, 40].

The LES technique has been well established for the simulation of supersonic STBLI [41, 42, 43, 44] and has a significant advantage over DNS in that it requires only a fraction of the computational grid size yet still produces high resolution turbulence statistics. This feature is even more attractive in the case of separated STBLI for which the ability to resolve the low-frequency shock motion is a concern. Running a DNS of a separated STBLI flow long enough to spectrally converge the lowest energized turbulence motions is essentially impossible from a practical standpoint. The DNS is also severely limited by Reynolds number due to the grid sizes required to resolve the entire range of turbulence motions from the viscous length scales to the outer length scales. Because the LES uses model equations to simulate the behavior of the smallest length scales, much larger Reynolds numbers are possible compared to DNS for similar computational cost. With LES, matching simulation to experimental Reynolds number is achievable.

LES of hypersonic STBLI seems at this point to still be in the developmental stage. Some preliminary works include the following. Shreyer *et al.* [45] and also Kim *et al.* [46] used Stanford University's CharLES code with eddy viscosity model of Vreman *et al.* [47] for the sub grid scale (SGS) model closure to reproduce the Mach 7 STBLI experiments by Schreyer *et al.* [48] of a compression ramp/expansion corner test article. The comparison with the experimental PIV data showed a stronger reverse flow in the separation bubble [45] and the turbulence intensity solution under-predicted the PIV data [46]. The authors do note that the PIV data of Schreyer *et al.* [48] suffered from insufficient particle density particularly at the wall surface and in the separated region making the comparison a bit vague. Ritos *et al.* [49] later attempted to simulate the same flow with an implicit

LES method by which the numerical properties of the inviscid flux scheme is used to estimate the dissipation by the unresolved SGS turbulence [49]. The LES of Ritos showed somewhat improved comparison with the PIV data from Schreyer, however the accuracy of the PIV profiles remains in question. Fang *et al.* [50] used an LES method with the dynamic eddy viscosity SGS models of Moin *et al.* [51] to simulate a single fin STBLI interaction at Mach 5 freestream and reported good comparison of mean flow structure and wall pressure with the experimental data of the same conditions by Schülein [9]. The peak skin friction near reattachment, however, was found to be significantly under-predicted.

1.3 Scope of the Present Work

In this work, an LES method employing a dynamic mixed SGS model [52] is used to simulate hypersonic STBLI compression ramp flows. All simulated flows considered throughout this thesis are low enthalpy and non-reacting as is typical of the flow conditions of many ground-based test facilities. In addition, all simulated flows are two-dimensional in the sense that they are of a flat plate boundary layer over a 2D wedge and are assumed to be homogeneous in the spanwise direction.

This work begins in Chapter 2 with a thorough validation of the LES computational method for the accurate simulation of STBLI flows including subsonic to hypersonic conditions and attached to fully separated interactions. Comparison with available DNS data demonstrates that the LES produces accurate low-frequency separation dynamics as well as wall heat transfer rates at elevated Mach number. After establishing the reliability of the LES method, in Chapter 3, two new LES datasets of separated hypersonic STBLI at freestream Mach numbers of 7.2 and 9.1 and at experimentally achievable conditions are presented. Mean flow statistics, turbulence intensities, wall quantities, turbulent

kinetic energy budgets, and anisotropy tensor properties are documented with the intention of making this information available to the scientific community for reference in cross-validation with experimental data, validation of other simulation methods, and the calibration of new turbulence models and experimental diagnostic techniques. Also in Chapter 3, it is demonstrated that the modeling of the local conservative energy exchange via a scale-similar SGS model is ncecessary in order to achieve correct shear layer spreading rate at high Mach number interactions for which the convective Mach number of the separation shear layer is found to be as high as 2.

In the remaining chapters of this thesis, the resulting database of hypersonic STBLI flows afforded by the current LES method is used for the investigation of several specific aspects of the STBLI flow. In Chapter 4, a low-pass filtering operation is performed on the time-resolved, three-dimensional flow field in order to identify the form of the low-frequency unstable mode in the hypersonic compression ramp interaction. The hypersonic STBLI mode is found to be similar to that previously identified in the subsonic regime [12, 22] allowing for generalizations to be made on the nature of the low-frequency instability. In Chapter 5, mean separation data from an LES database of varying shock strengths at Mach 7 and 10 was combined with a compilation of available hypersonic experimental data to investigate a generalized scaling method that relates separation length to interaction strength. The results provide new physical insight into the nature of the separation scaling. The topic of Chapter 6 is the characterization of the free shear layer that exists in the STBLI separated flow and the presentation of the results in the context of canonical mixing layer theory. The turbulence levels, spreading rate, and vortex structure in the shear layer were found to scale with convective Mach number in a manner consistent with available compressible mixing layer data. The benefits of the shear layer study are two-fold. The

results provide information on the generalization of separated STBLI flow behavior as well as new turbulence data for the study of compressible canonical mixing layers. Concluding remarks are given in Chapter 7

Chapter 2: Large Eddy Simulation Method and Validation

§The majority of this chapter is reproduced from Helm & Martin [53].

2.1 Chapter Overview

In this chapter, the accuracy of the LES method is demonstrated by testing it against a DNS database of compressible turbulent boundary layer and compression ramp solutions. For this purpose, two DNS solutions by Priebe & Martin are referenced which include a fully separated Mach 3 compression ramp STBLI flow [12] and an attached hypersonic Mach 7 compression ramp STBLI flow [34]. Each flow solution under consideration is reproduced with the LES code using the same computational domain size and boundary conditions as the corresponding DNS solution.

In Section 2.2 is a presentation of the LES numerical method and model equations for the SGS closure. The SGS models of the LES use a mixed model for both the unclosed shear stress in the momentum equation and the unclosed heat flux in the total energy equation. The mixed model uses a combination of an eddy viscosity term and a scale-similar model. The dissipative drain of turbulence energy from the resolved turbulence scales to the SGS scales are accounted for by the eddy viscosity while the conservative (non-dissipative) energy exchange between resolved and SGS scales is accounted for by the scale-similar model. Later in Chapter 3, which is concerned with the separated hypersonic STBLI condition, the importance of including the scale-similar term at high Mach number

conditions is further discussed and emphasized.

In Section 2.3, we provide a list of the conditions of our DNS and LES database followed by the description of the computational domains and setup. A statistical comparison is presented between the LES and Favre-filtered DNS solutions of the incoming boundary layer solutions in Section 2.4, the separated supersonic STBLI in Section 2.5, and the attached hypersonic STBLI in Section 2.6. The importance of the LES/DNS comparison of the separated STBLI is the demonstration that the same low-frequency unsteadiness is resolved by the LES in terms of frequency content, skin friction distribution, shear layer profiles, and separation length. It is also shown in Section 2.4 that the tophat filter of Eqn. 2.12 applied to the DNS data is an acceptable approximation of the LES filtered flow solution thus demonstrating that this is an appropriate method of DNS-to-LES comparison. A summary of the conclusions from this chapter are given in Section 2.7.

2.2 Numerical Method

The LES governing equations are derived by applying the filtering operation of Leonard [54] to the Navier Stokes equations for the conservation mass, momentum, and total energy. A filtered variable is defined as

$$\bar{f}(\xi) = \int_D f(\xi') G(\xi, \xi'; \bar{\Delta}) d\xi'. \tag{2.1}$$

In Eqn. 2.1, the variable f is filtered in space over the domain $D(\xi)$ by the function represented by $G(\xi)$. The filter width $\bar{\Delta}$ is representative of the smallest length scale retained by the filter $G(\xi)$. The filtered set of equations in conservative form and in a

generalized curvilinear coordinate system can be written as the following.

$$\frac{\partial \bar{U}}{\partial t} + \frac{\partial \bar{F}}{\partial \xi} + \frac{\partial \bar{G}}{\partial \eta} + \frac{\partial \bar{H}}{\partial \zeta} = \frac{\partial F_{SGS}}{\partial \xi} + \frac{\partial G_{SGS}}{\partial \eta} + \frac{\partial H_{SGS}}{\partial \zeta}. \tag{2.2}$$

The coordinate system (ξ,η,ζ) represent the computational space coordinates in which ξ is the streamwise body-tangential direction, η the spanwise direction, and ζ the body-normal direction. These are transformed from the real space coordinates (x, y, z) using the method outlined by Hirsch[55]. We use the convention that in real space, x is in the streamwise direction, y the spanwise direction, and z the wall-normal direction. In Eqn. 2.2, $\bar{U}$ is the vector of conserved quantities while $\bar{F}$, $\bar{G}$, and $\bar{H}$ are the flux vectors in their respective computational coordinate direction ξ, η, or ζ. The vectors F_{SGS}, G_{SGS}, and H_{SGS} are the unclosed sub-grid-scale (SGS) flux terms that result from the filtering operation.

The governing equations are expressed in terms of Favre-filtered variables defined as $\hat{f} = \overline{\rho f}/\bar{\rho}$. Using Favre-filtered variables prevents additional SGS terms from appearing in the filtered equation for the conservation of mass. Using the Favre-filtered notation,

the vectors from Eqn. 2.2 are

$$\bar{U} = J \begin{pmatrix} \bar{\rho} \\ \bar{\rho}\hat{u} \\ \bar{\rho}\hat{v} \\ \bar{\rho}\hat{w} \\ \bar{E} \end{pmatrix}, \; \bar{F}_c = Jr_\xi \begin{pmatrix} \bar{\rho}\hat{u}' \\ \bar{\rho}\hat{u}\hat{u}' + \bar{p}s_x \\ \bar{\rho}\hat{u}\hat{v}' + \bar{p}s_y \\ \bar{\rho}\hat{u}\hat{w}' + \bar{p}s_z \\ (\bar{E} + \bar{p})\hat{u}' \end{pmatrix},$$

$$\bar{F}_v = -Jr_\xi \begin{pmatrix} 0 \\ \hat{\sigma}_{xx}s_x + \hat{\sigma}_{xy}s_y + \hat{\sigma}_{xz}s_z \\ \hat{\sigma}_{yx}s_x + \hat{\sigma}_{yy}s_y + \hat{\sigma}_{yz}s_z \\ \hat{\sigma}_{zx}s_x + \hat{\sigma}_{zy}s_y + \hat{\sigma}_{zz}s_z \\ (\hat{\sigma}_{xx}\hat{u} + \hat{\sigma}_{xy}\hat{v} + \hat{\sigma}_{xz}\hat{w})s_x + \\ (\hat{\sigma}_{yx}\hat{u} + \hat{\sigma}_{yy}\hat{v} + \hat{\sigma}_{yz}\hat{w})s_y + \\ (\hat{\sigma}_{zx}\hat{u} + \hat{\sigma}_{zy}\hat{v} + \hat{\sigma}_{zz}\hat{w})s_z - \\ (\hat{q}_x s_x + \hat{q}_y s_y + \hat{q}_z s_z) \end{pmatrix}, \tag{2.3}$$

$$\text{and } F_{SGS} = -Jr_\xi \begin{pmatrix} 0 \\ \tau_{xx} \\ \tau_{yx} \\ \tau_{zx} \\ \gamma c_v Q_x + \frac{1}{2}\mathcal{J}_x - \mathcal{D}_j \end{pmatrix}$$

where

$$s_x = \xi_x / r_\xi, \; r_\xi = \sqrt{{\xi^2}_x + {\xi^2}_y + {\xi^2}_z}, \\ \text{and } \hat{u}' = \hat{u}s_x + \hat{v}s_y + \hat{w}s_z. \tag{2.4}$$

In Eqn. 2.3, the flux vector $\bar{F}$ has been split into a convective flux term ($\bar{F}_c$) and a viscous

flux term ($\bar{F}_v$) so that $\bar{F} = \bar{F}_c + \bar{F}_v$. Both $\bar{G}$ and $\bar{H}$ have equivalent expressions in their respective coordinate directions. The other terms in the expression for the flux vector $\bar{F}$ are the grid transformation Jacobian matrix J, the total filtered energy $\bar{E} = c_v\bar{\rho}\hat{T} + \bar{\rho}\frac{1}{2}\hat{u}_i\hat{u}_i + \frac{1}{2}\tau_{kk}$ (specific heat at constant volume c_v), the filtered shear stress tensor $\hat{\sigma}_{ij} = 2\hat{\mu}\hat{S}_{ij} - \frac{2}{3}\hat{\mu}\delta_{ij}\hat{S}_{kk}$ (strain-rate tensor $\hat{S}_{ij} = \frac{1}{2}(\partial\hat{u}_i/\partial x_i + \partial\hat{u}_j/\partial x_i$ and temperature dependent dynamic viscosity $\hat{\mu}$), and the heat flux $\hat{q}_j = -\hat{k}\partial\hat{T}/\partial x_j$ (temperature-dependent thermal conductivity $\hat{k}$). The definitions of the additional grid transformation terms are given in Eqn. 2.4. The kinematic viscosity is a function of the Favre-filtered temperature $\hat{T}$ and the exact relation is dependent on the conditions of the flow being simulated as will be explained further in Section 2.3. The thermal conductivity is related to the kinematic viscosity by $\hat{k} = \hat{\mu} * (2.5 * c_v - 1.5)$ The filtered pressure $\bar{p}$ is determined from the ideal gas law in terms of the filtered flow solution so that $\bar{p} = \bar{\rho}R\hat{T}$. The SGS flux vector F_{SGS} is expressed in terms of the SGS shear stress tensor τ_{ij}, the SGS heat flux $\partial\mathcal{Q}_j/\partial\xi_j$, the SGS turbulent diffusion $\partial\mathcal{J}_j/\partial\xi_j$, and the SGS viscous diffusion $\partial\mathcal{D}_j/\partial\xi_j$. From the derivation of the filtered LES governing equations, these unclosed terms are by definition

$$\tau_{ij} \equiv \bar{\rho}\Big(\widehat{u_i u'_j} - \hat{u}_i\hat{u}'_j\Big), \tag{2.5}$$

$$\mathcal{Q}_j \equiv \bar{\rho}\Big(\widehat{u'_j T} - \hat{u}'_j\hat{T}\Big), \tag{2.6}$$

$$\mathcal{J}_j \equiv \bar{\rho}\Big(\widehat{u'_j u_k u_k} - \hat{u}'_j\widehat{u_k u_k}\Big). \tag{2.7}$$

$$\mathcal{D}_j \equiv \overline{\sigma_{ij}u'_i} - \hat{\sigma}_{ij}\hat{u}'_i \tag{2.8}$$

The selection of the LES SGS closure models is based on the work of Martin *et al.* [52]. A one-coefficient dynamic mixed model containing both an eddy viscosity term

and a scale-similar term is used for the estimation of τ_{ij}. A similar formulation is used for the estimation of $\mathcal{Q}_j$. The SGS turbulent diffusion is approximated from the model proposed by Knight *et al.* [56]. The corresponding model equations for these three terms are

$$\tau_{ij} = -C_1 2\bar{\Delta}^2 \bar{\rho}|\hat{S}'|\left(\hat{S}'_{ij} - \frac{\delta_{ij}}{3}\hat{S}'_{kk}\right) + \rho\left(\widehat{\hat{u}_i\hat{u}'_j} - \hat{\hat{u}}_i\hat{\hat{u}}'_j\right), \tag{2.9}$$

$$\mathcal{Q}_j = -C_2\frac{\bar{\Delta}^2\bar{\rho}|\hat{S}'|}{Pr_T}\frac{\partial\hat{T}}{\partial\xi} + \bar{\rho}\left(\widehat{\hat{u}'_j\hat{T}} - \hat{\hat{u}}'_j\hat{\hat{T}}\right), \tag{2.10}$$

and

$$\mathcal{J}_j = \hat{u}'_k\tau_{jk}. \tag{2.11}$$

Here $\hat{S}'_{ij}$ is the coordinate-transformed strain rate tensor, the magnitude of which is defined as $|S'| = (2\hat{S}'_{ij}\hat{S}'_{ij})^{1/2}$. The filter width is indicated by $\bar{\Delta} = (\bar{\Delta}_\xi\bar{\Delta}_\eta\bar{\Delta}_\zeta)^{1/3}$ for which $\bar{\Delta}_\xi$, $\bar{\Delta}_\eta$, and $\bar{\Delta}_\zeta$ are the LES grid spacings in the three computational coordinate directions. The SGS viscous diffusion term (Eqn. 2.8) is not modeled as it is typically an order of magnitude smaller than the SGS heat flux [52]. Because of its relative insignificance and because there are currently no reliable models available for this term (the uncertainty of the models is on the order of the magnitude of the term itself [52]), the SGS viscous diffusion is excluded from our LES governing equations. The LES solution is implicitly filtered meaning that the coarse, under-resolved grid alone produces the filtered variables of Eqn 2.3. An explicit filtering operation is needed, however, to determine the dynamic coefficients (C_1, C_2) and the turbulent Prandtl number (Pr_T). For this purpose, we use a tophat filter defined as

$$\bar{f}_i = \frac{1}{2n}\left(f_{i-n/2} + 2\sum_{i-n/2+1}^{i+n/2+1} f_i + f_{i+n/2}\right). \tag{2.12}$$

In Eqn. 2.12, the subscript i is the central grid point, and $n\bar{\Delta}_\xi$ determines the width of the filter. The tophat filter is performed in computational coordinate space. For further details on the calculation of the dynamic coefficients and turbulent Prandtl number, the reader is referred to Martìn *et al.* [52]. For more information on the transform of the model coefficients into the generalized coordinate system, please see Armenio *et al.* [57]. Note that for the flows considered in this paper, namely the turbulent boundary layer and two-dimensional compression ramp STBLI configuration, the averaging operation in the definitions of C_1, C_2, and Pr_T is calculated locally as an ensemble average in the spanwise (homogeneous) direction only.

In an a priori study of isentropic compressible turbulence, Martin *et al.* [52] showed that both the correlation coefficient and the 'rms' amplitude of the solutions of τ_{ij} and $\mathcal{Q}_j$ were improved by including the scale-similar model as compared to an eddy diffusion term only. The first term in both Equations 2.9 and Eqn. 2.10 is the eddy viscosity contribution to the estimates of τ_{ij} and $\mathcal{Q}_j$, respectively, while the second term is the scale-similar contribution. Further demonstration of the importance of including the scale-similar terms for the accurate LES of STBLI flows will be given in in Chapter 3.

The following discretizations schemes are used to solve Eqn. 2.3 numerically. The inviscid flux terms are discretized using a 4th-order linearly and non-linearly optimized weighted essentially non-oscillatory (WENO) scheme [58, 59]. Both absolute and relative limiters are used for efficient application of the WENO scheme, thus significantly reducing the numerical dissipation caused by WENO throughout the flow [60]. Further reduction of the numerical dissipation in the boundary layer is obtained by what is referred to as filtering of the WENO candidate flux weights near the wall as was done by Martin [61]. The viscous fluxes and SGS terms are discretized using a 4th-order central differencing

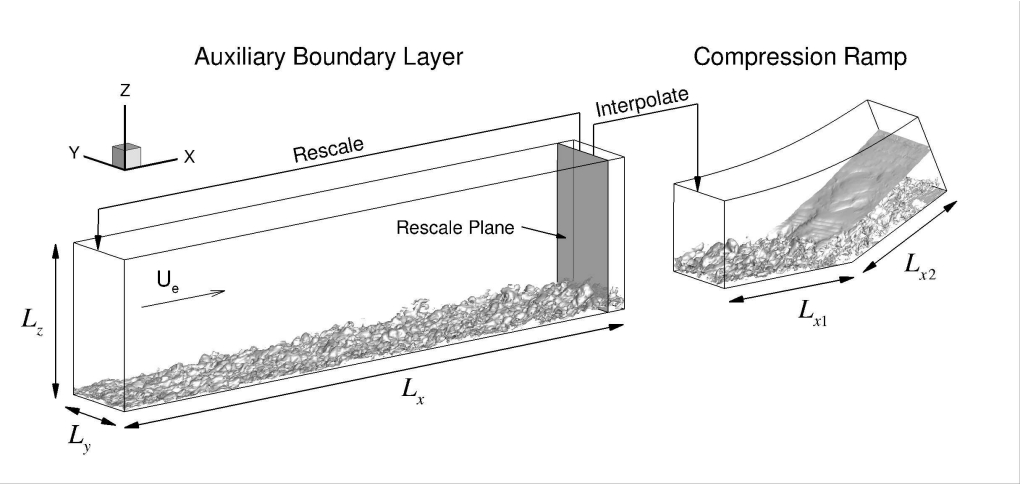

Figure 2.1: Schematic of LES computational domain and simulation strategy.

scheme. A low-storage, 3rd-order Runge Kutta method [62] is used for time advancement of the solution.

2.3 Computational Database

Following the work of Priebe & Martin [12, 34], the LES compression ramp solutions are run in two parts. These include an "auxiliary" boundary layer simulation which in turn provides the inflow condition for the "principle" simulation of the ramp geometry. This strategy is shown schematically in Fig. 2.1. The auxiliary boundary layer is run on a long computational box, and the recycling/rescaling method of Xu & Martin [63] is used for the assignment of the box inflow boundary condition. The solution at the rescaling plane near the outlet of the auxiliary boundary layer domain is interpolated in time and space onto the inlet of the grid of the compression ramp run as depicted in Fig. 2.1. The long rescaling length of the auxiliary simulation allows the turbulence eddies to develop spatially and to decorrelate as they convect the length of the box, thus minimizing any forcing that might be caused by recycling the turbulence. The recycling/rescaling inflow technique also ensures that the same boundary layer conditions are maintained at the exit over long

simulation times. This feature is necessary in order to resolve the low-frequency cycle of separated STBLI. By comparison, with purely streamwise periodic boundary conditions, the boundary layer thickness steadily grows over time.

Four auxiliary boundary layers are considered in our LES/DNS comparison. Freestream Mach numbers of 3, 7, and 10 are included. Each boundary layer condition is computed as a DNS and again as an LES with the same freestream conditions, wall temperature, and Reynolds numbers. The freestream conditions and boundary layer properties of each run are listed in Table 2.1. Included in Table 2.1 are the boundary layer edge (subscript "e") Mach number M_e, streamwise velocity U_e, temperature T_e, and density ρ_e. Wall temperature is given as a fraction of the adiabatic recovery temperature $T_r = (1+0.9(\gamma-1)M_e^2/2)$. Notice that the Mach 3 flows are approximately adiabatic while the Mach 7 and 10 flows are cold walls. The inner friction velocity $u_\tau = (\tau_w/\rho_e)^{1/2}$ is included together with the boundary layer thickness δ, displacement thickness δ^*, momentum thickness θ, and Reynolds numbers $Re_\tau = \delta u_\tau/\nu_w$, $Re_\theta = U_e\theta/\nu_e$, and $Re^* = \delta(\tau_w/\rho_e)^{1/2}/\nu_e$. The boundary layer length scales and Reynolds numbers are measured at the rescaling plane located approximately one boundary layer thickness upstream of the box outlet. All cases are fully turbulent.

The simulation case names in Table 2.1 indicate the freestream Mach number and the simulation type: "D" for DNS and "L" for LES. Two Mach 3 boundary layer cases are included in the database with the only significant difference between them being the spanwise width of the computational domain. These two conditions are labeled as M3n for "narrow" and M3w for "wide". The purpose of running two different Mach 3 auxiliary boundary layers is made clear in section 2.5 where the sensitivity of the Mach 3 STBLI mean flow to the spanwise domain width is addressed. The boundary layer runs M3n-D

and M7-D are borrowed from Priebe & Martin references [12, 34] as indicated by the superscript next to their casenames in Table 2.1. For the purpose of evaluating the LES solution of turbulent boundary layers at hypersonic conditions, a new DNS boundary layer with a Mach 10 freestream is run together with an LES dataset of the same; however, no DNS of a STBLI at the Mach 10 conditions are provided at this time due to the computational resources that would be needed to run this case. Instead, this LES Mach 10 boundary layer is used later in Chapter 3 as the inflow condition to a new Mach 10 STBLI configuration. The DNS box M10-D is used solely for the evaluation of the LES boundary layer solution M10-L.

The computational domain size and grid resolution of each boundary layer simulation is provided in Table 2.2. The outer dimensions are listed in terms of a reference boundary layer thickness δ_o. As shown in Fig. 2.1, the streamwise, spanwise, and wall-normal dimensions are specified by L_x, L_y, and L_z respectively. The M3n runs are $2\delta_o$ wide and the M3w runs are $4\delta_o$ wide. Both the Mach 7 and Mach 10 are run with extra wide domains for which $L_y = 10\delta_o$. All boundary layer computational grids have uniform resolution in the streamwise and spanwise directions and geometric stretching in the wall-normal direction. Streamwise and spanwise grid spacings are listed in terms of the inner boundary layer length scale $z_\tau = \nu_w/u_\tau$ as indicated by the '+' superscript. The distance from the wall surface to the first wall-normal grid point is listed as z_2^+. The total number of grid points in each simulation is indicated by N.

Our compression ramp DNS and LES database is detailed in Table 2.3. The compression ramp casenames begin with "R" followed by a number indicating the ramp deflection angle in degrees and ending with the case name of the boundary layer run that was used as the inflow condition. In Table 2.3, ϕ is the ramp deflection angle in degrees.

Case	M_e	U_e (m s^{-1})	T_e (K)	ρ_e (kg m^{-3})	T_w/T_r	u_τ (m s^{-1})	δ (mm)	δ^* (mm)	θ (mm)	Re_τ	Re_θ	Re^*
M3n-D [12]	2.91	609.7	108.9	0.0757	1.1	33.0	7.16	2.56	0.460	336	2809	1406
M3w-D	2.92	609.9	108.9	0.0755	1.1	33.4	7.29	2.69	0.489	346	2971	1446
M7-D [34]	7.16	1146.2	63.8	0.0771	0.52	62.4	4.61	2.50	0.173	202	3342	2091
M10-D	9.04	1410.7	58.6	0.0403	0.33	62.9	17.9	10.5	0.543	495	7486	4870
M3n-L	2.92	610.3	108.8	0.0753	1.1	33.7	7.51	2.69	0.498	359	3030	1502
M3w-L	2.92	610.4	109.0	0.0754	1.1	33.0	8.47	2.93	0.566	400	3447	1666
M7-L	7.16	1145.9	63.7	0.0763	0.52	62.3	4.56	2.47	0.170	197	3254	2041
M10-L	9.05	1410.6	58.5	0.0401	0.33	60.4	19.1	11.2	0.585	503	8038	4958

Table 2.1: Boundary layer edge and wall conditions for the LES and DNS database.

Case	δ_o (mm)	L_x/δ_o	L_y/δ_o	L_z/δ_o	Δx^+	Δy^+	z_2^+	$N \times 10^{-6}$
M3n-D [12]	7.1	8.3	2.0	8.2	6.8	4.2	0.21	7.3
M3w-D	7.1	8.3	4.0	8.2	6.9	4.3	0.21	13.4
M7-D [34]	5.0	27.0	10.0	14.2	7.1	2.9	0.24	96.7
M10-D	18.0	30.0	10.0	10.5	7.8	3.0	0.31	361.3
M3n-L	7.1	15.0	2.1	7.4	27.2	14.8	0.44	0.5
M3w-L	7.1	30.7	4.0	7.6	26.2	10.7	0.49	3.2
M7-L	5.0	26.6	9.5	13.6	27.8	10.7	0.48	3.0
M10-L	18.0	30.0	10.0	7.0	26.9	11.0	0.67	14.8

Table 2.2: Boundary layer grid size and resolution for the LES and DNS database.

As drawn in Fig. 2.1, L_{x1} is the computational domain length from the inlet to the corner and L_{x2} is the length measured from the corner, along the ramp surface, to the outlet plane. The width of each ramp computational domain is equal to that of its auxiliary boundary layer. The computational grid is stretched in the streamwise and wall-normal directions so that grid points are clustered near the corner and near the wall surface. The grid spacing is uniform in y. The grid resolution properties are given in "+" units nondimensionalized by the z_τ of the incoming boundary layer provided in Table 2.1. The total number of grid points for the compression ramp grids is indicated as N in Table 2.3. For the Mach 3 runs, the mean separation length L_{sep} is provided in units of the inflow δ from Table 2.1. The simulation duration over which mean statistics are computed is provided in time units δ/U_e. For the separated Mach 3 runs, the simulation time is also given in units of L_{sep}/U_e. All simulations, both auxiliary boundary layers and compression ramps, were run with spanwise periodicity and supersonic exit conditions at the top and outlet boundaries. No-slip velocity and constant temperature were assigned at the wall surfaces.

As noted in Section 2.2, the kinematic viscosity is specified as a function of the LES filtered temperature. For the flows considered in this work, one of three different viscosity laws is used depending on the range of temperatures occurring in the flow being

Case	ϕ	L_{x1}/δ_o	L_{x2}/δ_o	Δx^+	Δy^+	z_2^+	$N \times 10^6$	L_{sep}/δ	tU_e/δ	tU_e/L_{sep}
R24-M3n-D [12]	24^o	7.9	6.4	7.3-3.39	4.2	0.19	21.0	2.93	1058	361
R24-M3w-D	24^o	7.9	6.4	7.4-3.44	4.3	0.19	21.0	3.56	1000	281
R8-M7-D [34]	8^o	12.0	10.6	7.2-3.6	2.9	0.19	138.4	*attached*	88	-
R24-M3n-L	24^o	7.9	6.4	26.7-12.5	15.0	0.37	0.9	3.05	1070	350
R24-M3w-L	24^o	7.9	6.4	27.1-12.6	10.7	0.37	2.3	3.71	871	223
R8-M7-L	8^o	12.0	12.4	27.2-12.3	8.4	0.23	6.1	*attached*	146	-

Table 2.3: Compression ramp simulation details.

simulated and on the working fluid. Sutherland's law (Eqn. 2.13) is used for the Mach 3 simulations for which the temperatures does not drop below $100K$ and the working fluid is air. For flows experiencing temperatures below this threshold, Keyes temperature-viscosity relations [64] are more accurate than Sutherland's law [8, 34]. Keyes relation for air (Eqn. 2.14) is used for the Mach 7 simulations. The working fluid of the Mach 10 flows is pure Nitrogen for which Keyes law for Nitrogen is used (Eqn. 2.15).

$$\hat{\mu} = 1.458 \times 10^{-6} \frac{\hat{T}^3}{\hat{T} + 110.3} \tag{2.13}$$

$$\hat{\mu} = 1.488 \times 10^{-6} \frac{\hat{T}^{1/2}}{1 + (122.1/\hat{T})10^{-5/\hat{T}}} \tag{2.14}$$

$$\hat{\mu} = 1.418 \times 10^{-6} \frac{\hat{T}^{1/2}}{1 + (116.4/\hat{T})10^{-5/\hat{T}}} \tag{2.15}$$

The reader is directed to the references indicated in Tables 2.1-2.3 for further details on the compuational setup and initialization of the Mach 3 and Mach 7 DNS runs. We now describe the initialization method of the datasets that are new to this article. The M3w-D boundary layer run was initialized from an instantaneous volume solution of the M3n-D run streteched in the streamwise and spanwise directions. The M10-D boundary layer was initialized using the method of Martin *et al.* [65] in which a mean boundary layer profile obtained from a RANS solution is added to the fluctuation flowfield of an incompressible turbulent boundary layer DNS scaled by the mean density according to Morkovin's hypothesis. All LES auxiliary boundary layer runs (M3n-L, M3w-L, and M7-L) were initialized by selecting a single instantaneous volume solution of the corresponding DNS flow, applying a tophat filter in space, and then interpolating the filtered solution onto the LES grid. In all cases, the initial boundary layer flow volume was allowed to

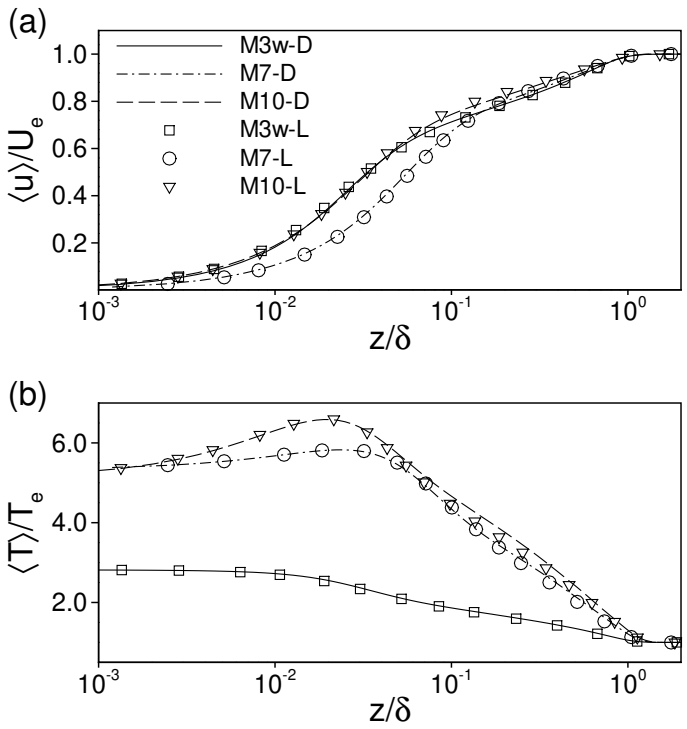

Figure 2.2: Auxiliary boundary layer mean profiles of (a) streamwise velocity and (b) temperature normalized by the freestream value. Profiles are taken from the rescaling plane near the outlet of the box. The DNS profiles are not filtered.

run through a transient. Establishment of a statistically accurate boundary layer flow was determined by the convergence of the spatial correlation lengths, the skin friction level, and the displacement and momentum thicknesses. The new compression ramp runs (R24-M3w-D, R24-M3n-L, R24-M3w-L, and R8-M7-L) were initialized by taking a volume solution from their respective inflow boundary layer runs and interpolating it along the entire length of the ramp surface. The ramp flow was then run through a transient phase until the skin friction distribution showed that the interaction region had reached its natural separated state.

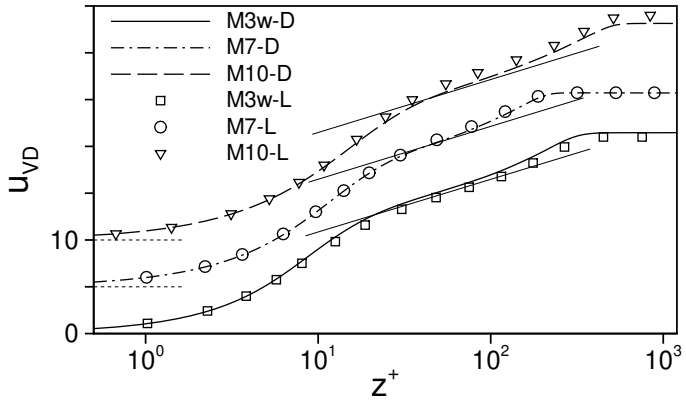

Figure 2.3: Van Driest transformed velocity profiles at the auxiliary boundary layer rescaling plane. The DNS profiles are not filtered.

2.4 Turbulent Boundary Layer

In this section we present the statistical evaluation of the mean flow at the rescaling plane of the auxiliary boundary layer simulations from Table 2.1. As can be determined from the grid resolution information listed in Table 2.2, the resolution of the LES auxiliary boundary layers is reduced from that of the DNS by a factor of (approximately) 4, 4, and 2 in the i, j, and k-directions respectively. In order to obtain a filtered DNS flowfield to compare to the LES solution, the tophat filter of Eqn. 2.12 was applied to the DNS solution in computational space with filter widths corresponding to the grid size of the LES. We found that the first-order mean flow statistics of the DNS data were unaffected by the filtering operation. Time- and spanwise-averaged profiles of streamwise velocity and temperature nondimentionalized by the freestream are plotted versus z/δ in Fig. 2.2 together with the unfiltered DNS data. Because the M3w and M3n boundary layer conditions are so similar, only the profiles from M3w are shown. An excellent comparison of mean velocity and temperature is made. The discrepancy between the LES and DNS is found to be within 3% error for both the Mach 3 and Mach 7 and within 5% for the Mach

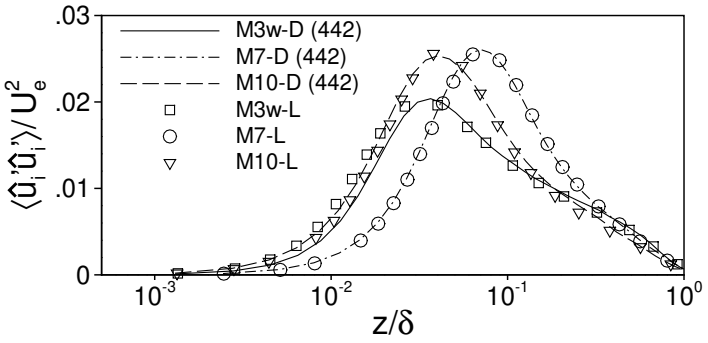

Figure 2.4: Turbulent kinetic energy profiles (TKE = $\langle \hat{u}_i' \hat{u}_i' \rangle / U_e^2$) at the auxiliary boundary layer rescaling plane. The DNS data is Favre-filtered by the tophat filter of Eqn. 2.12. The filter width in i, j and k is indicated by the number in parentheses.

10. The van Driest transformed velocity profiles are plotted in Fig. 2.3. These density-weighted and integrated mean velocity profiles also show excellent comparison with the unfiltered DNS data. All three flow conditions result in less than 3% error.

The profiles of time- and span-averaged turbulent kinetic energy, defined as TKE = $\langle \hat{u}_i' \hat{u}_i' \rangle / U_e$, are plotted in Fig. 2.4. The angled brackets indicate the time and spanwise Reynolds average, and (') now represents a fluctuation about the Reynolds average and is not to be confused with the grid transform definition in Eqn. 2.4. The tophat-filtered DNS solutions are now used for the comparison of the TKE. The numbers in parentheses in the legend of Fig. 2.4 indicate the filter width of the tophat filter applied to each DNS dataset. For example, (442) refers to a tophat filter with $n = 4$, 4, and 2 in the i, j, and k grid directions respectively. The difference in the peak TKE level between the LES and the filtered DNS is less than 2%.

The percentage of total turbulent kinetic energy contained in the SGS terms of the LES can be estimated in one of two ways, either by computing the difference between the TKE profiles of the LES and DNS, or by computing the difference between the filtered DNS and the unfiltered DNS. Both of these estimates are plotted in Fig. 2.5 for the

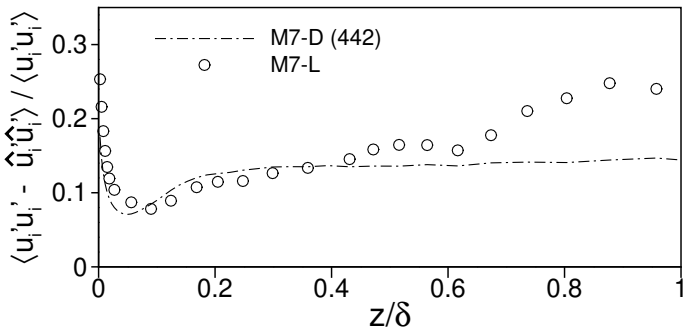

Figure 2.5: The fraction of TKE contained in the sub-grid scales for the M7-L boundary layer run. The dashed line shows the TKE difference in the filtered DNS compared to the unfiltered DNS. The symbols show the TKE difference in the LES as compared to the unfiltered DNS.

Mach 7 boundary layer. Note that the difference in TKE is expressed as a fraction of the local DNS value. The estimation from the filtered DNS shows that the percentage of unresolved TKE is approximately 14% for the majority of the boundary layer. Below $z/\delta = 0.2$, the percentage drops to a minimum of 7% and then increases to a maximum of 18% at the wall. The estimation from the LES solution matches the filtered DNS for z/δ below approximately 0.6. There is a discrepancy between the two estimates, both at the wall and at the boundary layer edge. This is at least partially due to the fact that the total TKE goes to zero at these two locations, thus increasing the error sensitivity. Similar results are obtained for the Mach 3 and Mach 10 boundary layers for which the percentage of unresolved TKE are consistently between 10% and 15%, and the local minimum near the wall does not drop below 5%.

Further information on the truncation of the turbulence fluctuations in the LES data can be obtained through spectral analysis. The pre-multiplied power spectral density of the time signal of mass fluctuations (defined as $(\bar{\rho}\hat{u})'$ for the LES and $(\rho u)'$ for the DNS) in the Mach 7 boundary layer is plotted in Fig. 2.6. The time signal is taken from a point in the center of the logarithmic layer at $z^+ = 50$ ($z/\delta = 0.25$) where the SGS TKE

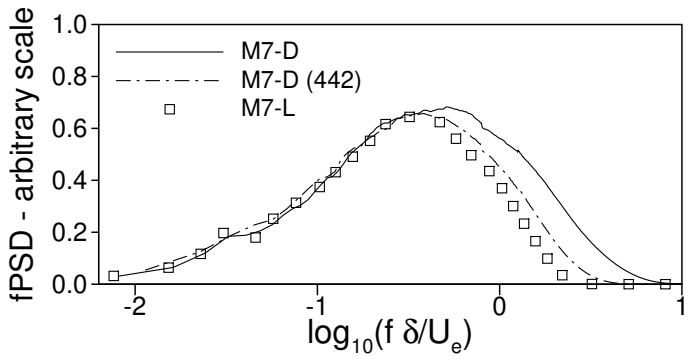

Figure 2.6: Pre-multiplied power spectral density of mass fluctuations ($(\bar{\rho}\hat{u})'$ for the LES and $(\rho u)'$ for the DNS) at the rescaling plane of the Mach 7 auxiliary boundary layers.

percentage is about 12%. In Fig. 2.6, the frequency is non-dimensionalized by δ/U_e. The spectra are calculated using Welch's method with eight overlapping time segments and bin sampled with a bin width of $\log_{10}(f\delta/U_e) = 0.1$. Included in this comparison of the spectra is the tophat-filtered DNS signal. The tophat-filtered DNS spectra was obtained by taking the full resolution DNS time signal of $(\rho u)'$ at $z^+ = 50$ at the boundary layer rescaling plane and filtering it with the tophat filter converted from space to time via Taylor's hypothesis of frozen turbulence [66]. The local mean velocity was used for the time-to-space conversion. Because the magnitude of the spectral density is arbitrary, the spectra are scaled so that the three curves coincide at the lowest frequencies. By plotting the spectra in this way, one can see how the LES truncates the solution at the highest frequencies of motion when compared to the DNS and filtered DNS. Figure 2.6 shows that the spectral content of both the LES and the filtered DNS is essentially unaffected for wavelengths below $f\delta/U_e \lesssim 0.4$. The comparison between the LES and filtered DNS spectra indicate that the tophat filter truncates the high frequency content in the DNS data in a manner very similar to the truncation of the turbulence by the LES solver. The results shown in Fig. 2.6, together with Figures 2.4 and 2.5, demonstrate that the tophat-

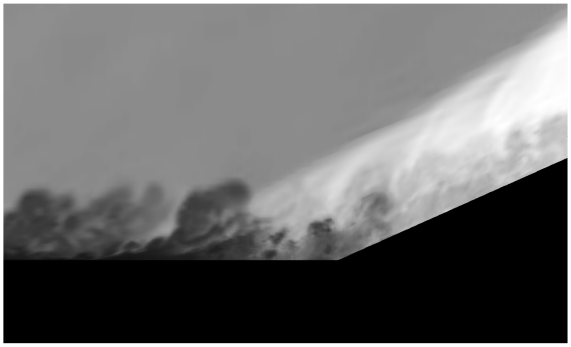

Figure 2.7: Instantaneous visualization of density in a center-span xz-plane of R24-M3-L.

filter operation applied to the DNS data closely mimics the LES solution and therefore is an acceptable method of validating the LES data.

2.5 Supersonic Separated STBLI

In this section we evaluate the LES soltuions of the Mach 3 compression ramp flows listed in Table 2.3. The resolution of the LES compression ramp grids is reduced from the DNS of Priebe & Martin [12] by a factor of approximately 4, 2, and 2 in the i, j, and k-grid directions respectively. Applying a (422) filter results in approximately a 10% to 15% reduction in the TKE throughout the interaction region and in the downstream recovering boundary layer. As with the boundary layer from Section 2.4, the first-order mean flow statistics of the DNS data were found to be unaffected by this filtering operation.

The corner flow of the R24-M3w-L run is visualized in Fig. 2.7 by a snapshot of the instantaneous density field in an xz-plane located at the center of the span width. Several of the key features of this flow are visible in Fig. 2.7. One can clearly make out the large forward-leaning turbulence structures in the incoming boundary layer, the initial compression waves upstream of the corner, the main shock front, and even several

shocklets emitting from the turbulence structures in the downstream boundary layer. A change in the length scale of the turbulence across the shock is also apparent. From this figure, it is evident that, even with the factor of 16 decrease in grid resolution, the LES solution maintains a high level of detail in the turbulence.

In Fig. 2.8 (a) is shown the time- and spanwise-averaged distribution of skin friction coefficient $C_f \equiv 2\tau_w/\rho_e {U_e}^2$ for both the wide and narrow domain solutions plotted versus x'/δ. The LES averaged skin friction distributions are compared to the DNS in Fig. 2.8. Here the x'-axis is defined as the distance measured along the wall surface with $x' = 0$ located at the ramp corner. The mean separation and reattachment points are defined as the x' locations where the C_f crosses zero. The separation length L_{sep} is the distance between these two points measured along x'. The data shows that the separation length differs significantly between the wide-domain and narrow-domain solutions. This difference in L_{sep} with spanwidth is seen in both the LES and DNS solutions. Considering this, the fact that the narrow spanwidth modifies the size of the separation is not surprising. Many studies have shown that the supersonic compression ramp STBLI flow is not strictly two dimensional but has a spanwise periodicity on the order of the boundary layer thickness (See [24] and the references therein). The sensitivity of the separation length to the spanwidth, however, it is an important behavior to be aware of in interpreting the separation data of STBLI simulations as many of the available DNS and LES simulations are computed on narrow domains. To the authors' knowledge, this spanwidth effect has not been closely addressed. For the comparison of the current Mach 3 datasets, we note that if the skin friction is plotted versus x'/L_{sep} instead of x'/δ, all four solutions collapse extremely well as in Fig. 2.8 (b) indicating that the separation length is the appropriate length scale for the comparison of the mean flow.

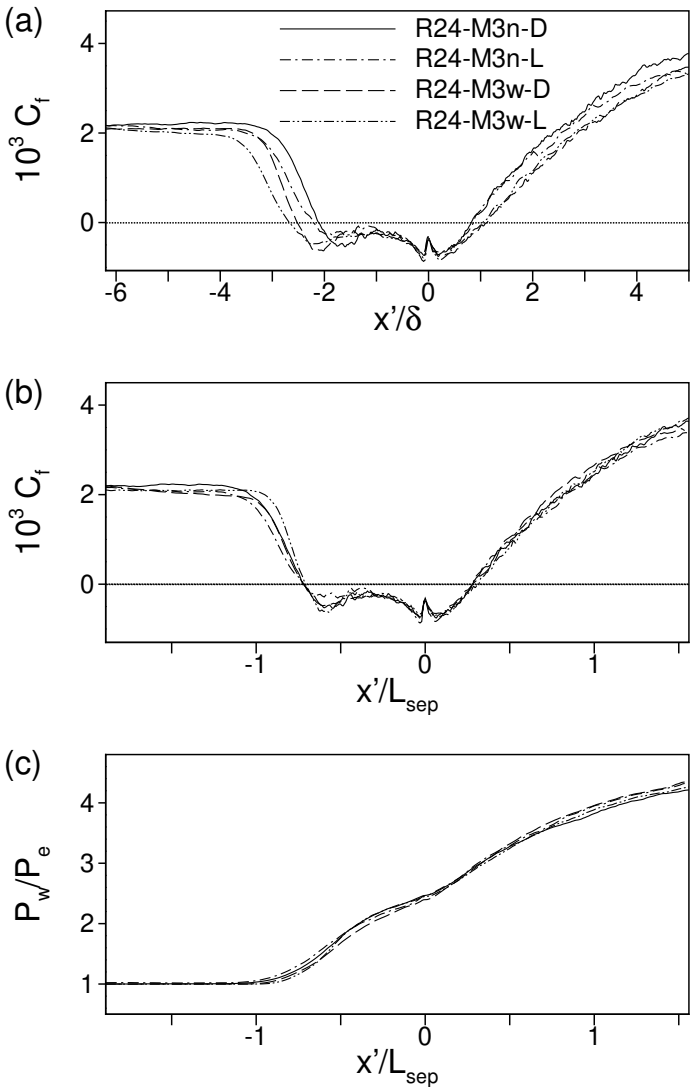

Figure 2.8: Mean wall distributions of (a) skin friction versus x/δ, (b) skin friction versus x/L_{sep}, and (c) wall pressure versus x/L_{sep} for the Mach 3 STBLI solutions. The DNS data are not filtered.

The skin friction distribution itself is characterized by a multi-inflection point curve in the separated region in which a local maximum in C_f occurs in the center of the separation bubble. Using a conditional averaging technique, Priebe & Martin [12] showed that this feature in the skin friction signature is caused by specifically the bubble collapse phase in the low-frequency oscillation cycle of the separation bubble unsteadiness. The fact that the LES captures the same C_f distribution as the DNS is an indication that the low-frequency dynamical mode is simulated correctly by the current LES method.

The time- and spanwise-averaged wall pressure distributions of the Mach 3 ramp solutions are plotted in Fig. 2.8 (c). In the separated region, a slight leveling off or "plateau" in the pressure is noticeable. Wu & Martin [60] demonstrated that excess numerical dissipation can prevent the occurrence of this feature. The quality of the comparison in 2.8 (c) provides assurance that the LES does not suffer from this problem despite the coarser grid resolution.

The separation shear layer is another feature of the supersonic STBLI separated flow that is crucial to the overall accuracy of the solution. Figure 2.9 (a) shows the comparison of the profiles of mean velocity through the separation shear layer of the LES and DNS data. These profiles were taken from the time- and spanwise-averaged mean flow solutions along a line perpendicular to the wall surface just ahead of the corner at $x'/L_{sep} = -0.15$. The excellent comparison confirms that the LES is correctly reproducing the aspect ratio of the separation bubble as well as the spreading rate of the shear layer. Streamwise and spanwise turbulence intensities taken from the same location are plotted in Fig. 2.9 (b). Here the LES is compared to the filtered DNS solutions. Again, an excellent comparison is made. The peak turbulence levels of the LES are within 6% of the DNS.

The spectral content associated with the low-frequency unsteadiness in supersonic

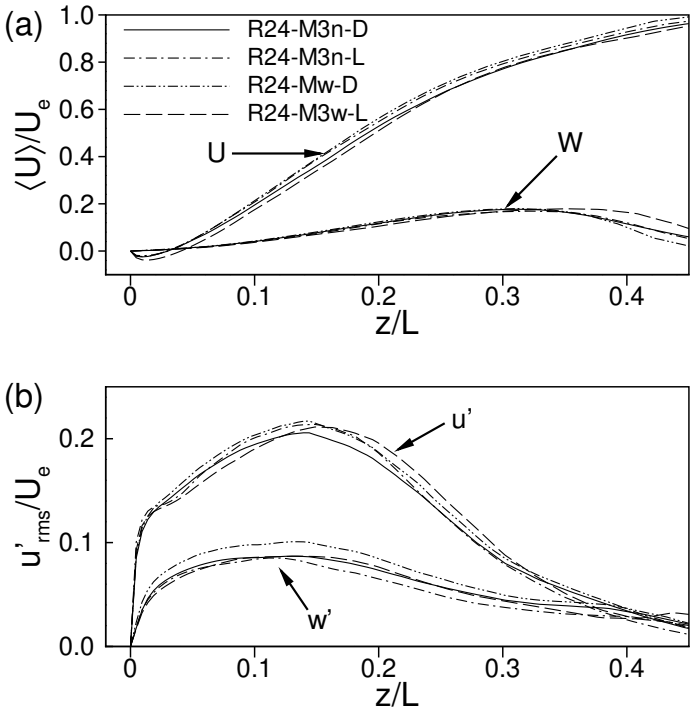

Figure 2.9: Profiles of (a) mean velocity, and (b) turbulence intensities in the shear layer of the Mach 3 STBLI solutions. The DNS in (a) is not filtered. A (422) filter is applied to the DNS data in (b).

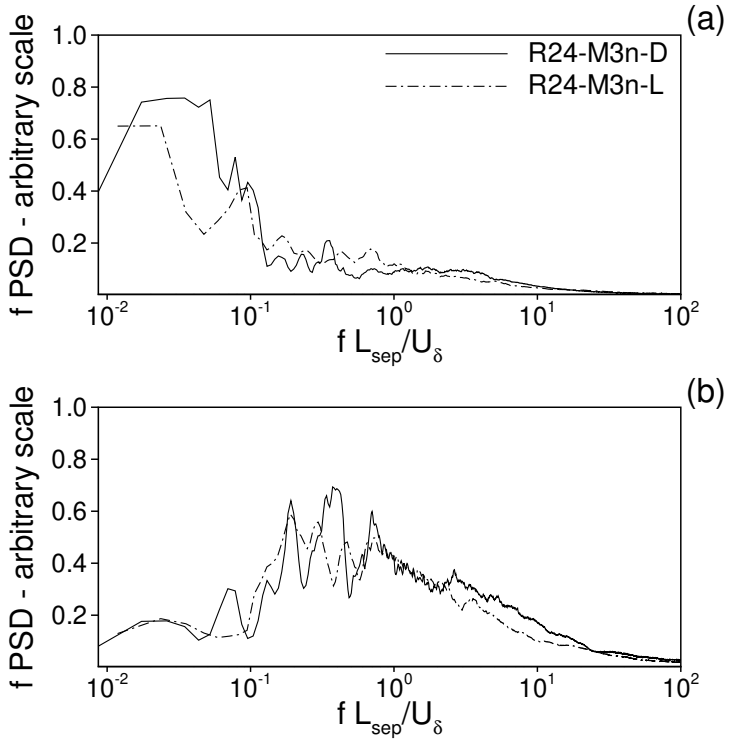

Figure 2.10: Pre-multiplied power spectral plots of the time history of (a) separation point, and (b) reattachment point in the narrow Mach 3 STBLI DNS and LES solutions.

separated STBLI is well documented both experimentally and computationally (For example see [11, 12]). The pre-multiplied power spectral density of the R24-M3n-L run separation time signal is plotted in Fig. 2.10 (a) with the DNS spectra from Preibe & Martin [12]. The nondimensionalized frequency Strouhal number is defined as $St = fL/U_e$. Because the simulation duration only resolves approximately 10 low-frequency cycles, it is not expected that the lowest frequencies are spectrally converged. However, the LES and DNS both show the dominant energy content occurs in the range of $St \approx 0.01$ to 0.03. A similar comparison is made in Fig. 2.10 (b). with the reattachment signal spectra. The compressed incoming turbulence and the spanwise-oriented mixing layer-like vortices that form in the separation shear layer both contribute to the broadband energy in the reattachment spectra. The LES matches the broadband energy content of the DNS centered at St of $\mathcal{O}(0.1)$ Some low-frequency energy is also captured in the reattachment spectra of the LES with good comparison to the DNS spectra.

2.6 Hypersonic Attached STBLI

In this section we present the LES-to-DNS comparison of the flow organization, mean wall quantities, and Reynolds stress contours of the attached Mach 7, 8^o compression ramp configuration (datasets R8-M7-L and R8-M7-D in Table 2.3). A spatial tophat filter with filter widths of 4, 4, and 1 in the i, j, and k grid directions respectively was applied to the DNS data for postprocessing. As with the bounday layer solutions of Section 2.4 and the supersonic STBLI solution of Section 2.5, the first-order mean flow statistics of the DNS solution R8-M7-D were not affected by the filter.

An instantaneous snapshots of the density field in an xz-plane located at the center span of the three-dimensional flow volume of the LES solution is plotted in Fig. 2.11.

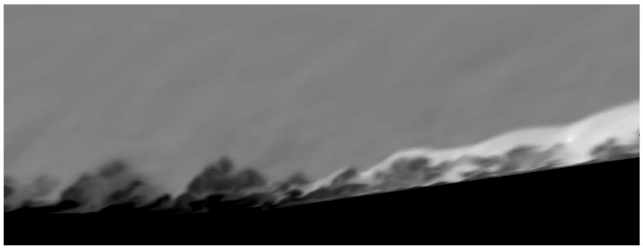

Figure 2.11: Instantaneous visualization of density in a center-span xz-plane of R8-M7-L.

As was shown in Section 2.4 with the Mach 3 STBLI, the instantaneous density field provides a descriptive image of the turbulence structure and overall flow organization. The structure of the incoming turbulence is seen as large, dark conglomerates of eddies about the size of the incoming boundary layer thickness. The main shock front is visible as a light area above the ramp surface. The main shock is seen to wrap around the large turbulence structures of the boundary layer as they pass through the interaction. Priebe & Martin [34] noted similar features in a comparison of instantaneous visualizations of the DNS solution and the experimental Filtered Rayleigh Scattering images of Bookey *et al.* [35].

Time- and spanwise-averaged wall distributions of skin friction, pressure, and heat transfer are plotted for the LES and for the unfiltered DNS in Fig. 2.12. The heat transfer coefficient, or Stanton number, is defined as $C_h \equiv q_w/\rho_e U_e c_p (T_w - T_r)$ where q_w is the rate of heat transfer at the wall and c_p is the specific heat at constant pressure. The wall quantities are plotted versus the distance measured along the wall surface from the ramp corner. The wall-distance is labeled in Fig. 2.12 as x' to distinguish it from the simulation (x, y, z) coordinates. The skin friction distribution shown in Fig. 2.12 (a) makes a sharp dip at the corner but does not drop below $C_f = 0$. This STBLI flow is therefore said to

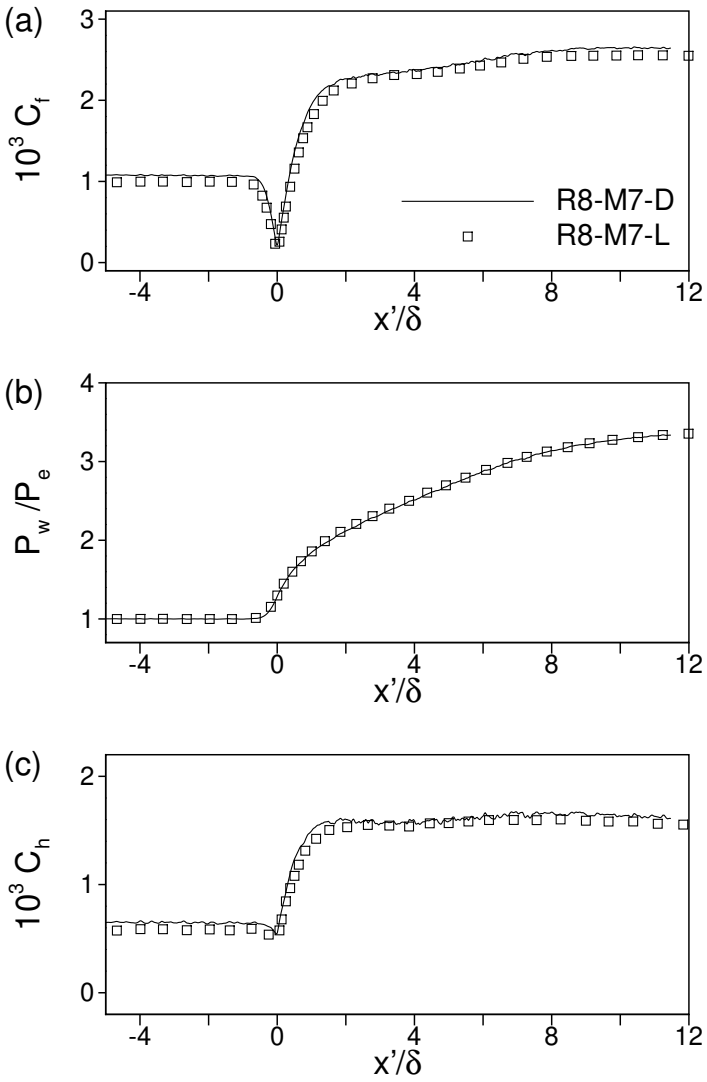

Figure 2.12: Wall distributions of (a) skin friction coefficient $C_f = 2\tau_w/\rho_e U_e$, (b) pressure, and (c) heat transfer coefficient $C_h \equiv q_w/\rho_e U_e c_p(T_w - T_r)$ of the Mach 7, 8^o compression ramp LES and (unfiltered) DNS mean flow solutions.

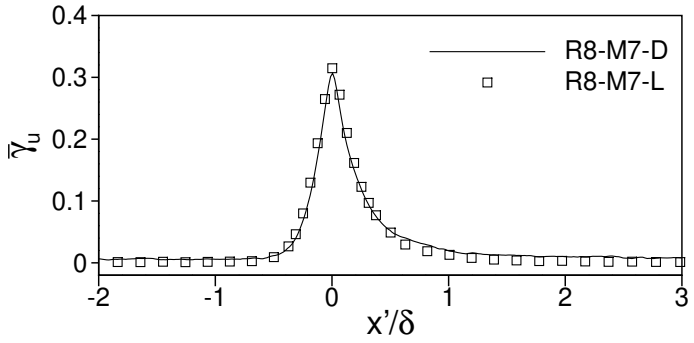

Figure 2.13: Time- and spanwise-averaged reverse probability at the wall surface of the Mach 7, 8^o compression ramp LES and (unfiltered) DNS flow solutions.

be attached in the mean sense. The LES solution closely follows the DNS skin friction dip at the corner and also the gradual increase in the recovering boundary layer further downstream. On the ramp surface, the difference in skin friction between the LES and the DNS is approximately 3%. The LES solution of wall pressure in Fig. 2.12 (b) also shows an excellent comparison with the DNS and there is no notable difference between the two. The heat transfer coefficient in Fig. 2.12 (c) is also found to be within 4% of the DNS solution on the ramp. The shallow dip at $x'/\delta = 0$ and the subsequent step-like incease to the downstream heat transfer level are well resolved in the LES data.

Although it is fully attached in the mean sense, Priebe & Martin [34] found that this particular Mach 7 STBLI configuration has a certain probaility of instantaneous separation at the corner. In Fig. 2.13, the spanwise averaged probability of flow reversal at the wall $\bar{\gamma}_u$ as reported by Priebe & Martin for R8-M7-D is compared to the same quantity calculated for R8-M7-L. The quantity $\bar{\gamma}_u$ is the fraction of flow instances over the total number of flow realization in the ensemble average for which the streamwise velocity $u < 0$. Figure 2.13 shows the distribution of $\bar{\gamma}_u$ one grid point above the wall surface. The width of the probability distribution as well as the maximum at the corner are in excellent

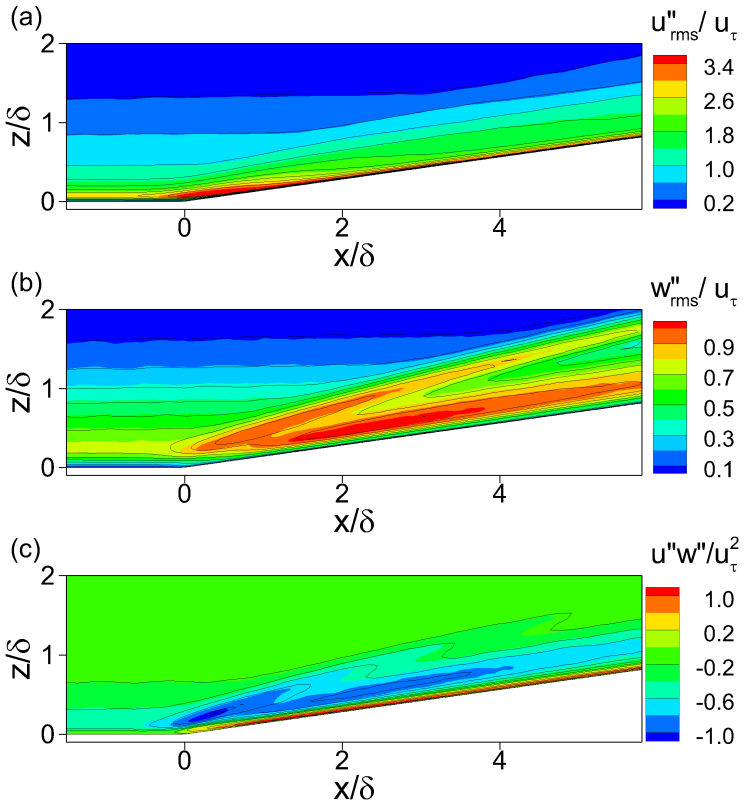

Figure 2.14: Contours of averaged (a) streamwise, (b) wall-normal, and (c) cross turbulence stresses in the Mach 7, 8^o compression ramp flow solutions. The color contour is the filtered DNS data and the solid line contour is the LES data.

agreement between the LES and DNS data. The peak probability at $x'/\delta = 0$ is 31% for both the DNS and the LES.

Next we compare the turbulence stresses $\sqrt{\widetilde{u''u''}}$, $\sqrt{\widetilde{w''w''}}$, and $\widetilde{u''w''}$ to the filtered DNS flow. Here the tilde represents a Favre averaged quantity such that $\tilde{u} = \langle \rho u \rangle / \langle \rho \rangle$ and a fluctuation about the Favre average is indicated by the double prime such that $u'' = u - \tilde{u}$. The color contours in Fig. 2.14 represent the Favre averaged turbulence stresses of the filtered DNS solution and the overlying black contour lines are the same for the LES solution. The stresses are nondimensionalized by the incoming boundary layer friction velocity u_τ. The two contours of the filtered DNS and the LES are very nearly the same for all three quantities and the areas of turbulence amplification are very well

reproduced by the LES both in the spatial extent and in magnitude. The peak turbulence in the LES contours differs from the filtered DNS peak levels by $0.2u_\tau$ in the streamwise and cross stresses, and by only $0.1u_\tau$ in the wall-normal stress. Although not included in Fig. 2.14, the error in the maximum of the spanwise stress componenet $\sqrt{\widetilde{v''v''}}$ was found to be less than $0.03u_\tau$.

2.7 Summary

In this chapter it was demonstrated that the LES method of Section 2.2 solving the Favre-filtered equations for conservation of mass, momentum, and total energy using a one-coefficient mixed model for SGS shear stress and heat flux [52], a triple correlation relation for SGS turbulence diffusion [56], and a bandwidth optimized WENO discretization scheme produces accurate solutions of hypersonic STBLI.

The LES solutions of the incoming turbulent boundary layers at Mach 3, 7 and 10 showed an excellent statistical comparison with the filtered DNS solution in the profiles of mean velocity, temperature, van Driest transformed velocity, and turbulent kinetic energy. Spectral content in the LES and filtered DNS boundary layers indicated that the tophat filter is a good approximation of the LES solution truncation of the smaller turbulence scales. In conclusion, the tophat filtered DNS solution provides a good comparison for the validation of the LES solution. A comparison among the LES, DNS, and filtered DNS solutions of TKE revealed that the LES resolution used in this study resulted in approximately 12%-25% of the total TKE being contained in the SGS terms.

The LES was shown to accurately reproduce the separated Mach 3 STBLI solution in terms of skin friction distribution (separation length), wall pressure, shear layer profiles, and frequency content at separation and reattachment. Neither the DNS solution of

Priebe & Martin [12] nor the R23-M3n-L LES solution presented here can be considered as spectrally resolved at the low frequencies associated with the shock unsteadiness as only about 10 low-frequency cycles are contained in either dataset. However, the comparison of the LES and DNS separation spectra showed that the dominant energy in both solutions is contained at the lowest frequencies in the range $fL_{sep}/U_e \approx 0.03$ to 0.1. In addition, the simulation of two different span widths for the Mach 3 separated STBLI condition ($L_y = 2\delta$ and $L_y = 4\delta$) presented in Section 2.5 of this paper indicates that the compression ramp STBLI, although a two-dimensional geometry, is not a strictly two-dimensional flow. Many studies on supersonic separated STBLI have identified a spanwise-periodic structure in the separated flow and there is evidence that this spanwise periodicity is linked to the form of the low-frequency unstable mode [1, 22, 24, 41, 67, 68]. If the domain width is too narrow, these structures may be artificially confined in the spanwise direction thus altering the separation length.

The hypersonic STBLI comparison revealed that the LES properly reproduced the mean turbulence field including the strong amplification of the Reynolds stress components as well as the wall shear stress and heat transfer. The incipient separation of this condition documented by Priebe & Martin [34] was very well reproduced by the LES as indicated by the probability of instantaneous reverse flow along the ramp surface.

Concerning the application of the LES method, we used a rather conservative filter strength. The filter strength was achieved by downsampling the i-, j-, and k-grids by approximately 4, 4, and 2 from the resolution needed to run the code in DNS mode, that is, with the SGS model terms turned off. As a result, the LES operates on a factor of 32 fewer grid points than the DNS which is equivalent to 3% of the DNS computational cost. This is a significant reduction even considering the computational overhead needed

to solve the LES model equations. Because of the coarser grid, the CFL condition of the numerical method necessarily produces a larger time step for the LES. In the case of the separated Mach 3 flow (R24-M3-L), the average LES time step was 2.8 times larger than that of the DNS. Further savings in the computational cost and runtime could be achieved by studying the limit of SGS filtering that the LES method can handle and still produce an accurate solution. The boundary layer profiles of percentage TKE in the SGS terms shown in Fig. 2.5 show there is approximately 25% energy in the SGS at the wall and 12% in the majority of the boundary layer above $z/\delta = 0.2$. The a priori studies of Martin *et al.* [52] indicate that maintaining 25%-30% TKE in the SGS throughout the boundary layer may be possible.

Chapter 3: LES of Two Separated Hypersonic STBLI

§The majority of this chapter is reproduced from Helm & Martin [53].

3.1 Chapter Overview

In light of the validation analysis presented in Chapter 2, we now proceed to use the LES method of Chapter 2 to generate two new datasets of separated hypersonic STBLI flows. The first of these is a Mach 7 flow with the same freestream and boundary layer conditions as the attached R8-M7-L ramp but the ramp angle is increased from 8^o to 33^o The M7-L turbulent boundary layer run is again used as the inflow condition. The second is a Mach 10 flow over a 34^o compression ramp for which the incoming boundary layer is the M10-L dataset. Following the naming convention introduced in Chapter 2, these two new datasets are referred to as R33-M7-L and R34-M10-L respectively.

This chapter is primarily concerned with the documentation of the time- and spanwise-averaged flow field of these two separated hypersonic datasets. Details of the computational setup and the convergence of the mean flow are given in Section 3.2. A description of the flow organization is given in Section 3.3 including a comparison of the downstream flow with the oblique shock solution. The mean solution of velocity, temperature, and density as well as averaged wall quantities are provided in Section 3.4. Wall quantities reported include the pressure, skin friction, heat transfer and the variation in the fluctuation intensities of these properties along the ramp surface. The solutions of the

averaged turbulence are the topic of Section 3.5. Turbulence data included in this chapter are the averaged Reynolds stress flow fields, the turbulent kinetic energy budgets, and the anisotropy tensors. Several turbulence modeling assumptions are evaluated for these flows including the Reynolds Analogies relating velocity and temperature fluctuations, the Reynolds Analogy Factor (RAF) relating skin friction to heat transfer, and the so-called QP85 law [69] relating wall pressure to wall heat transfer.

An important result presented in this chapter is the comparison of the LES solutions of the separated hypersonic STBLI using the current dynamic mixed model to that generated using the dynamic eddy viscosity model only. As is discussed in Section 3.7, the conservative energy exchange that is accounted for by the scale-similar term in the mixed model is necessary for the accurate simulation of the separation shear layer. Excluding the scale-similar term was found to result in as much as 30% error in the separation length at high Mach number.

This chapter concludes with a summary of results in Section 3.8.

3.2 Computational Setup and Mean Flow Convergence

Details of the computational grid, simulation duration, and mean separation length of the R33-M7-L and R34-M10-L runs are provided in Table 3.1. The computational domain of R33-M7-L has the same outer dimensions and grid resolution as the R8-M7-L simulation. The outer dimensions of the R34-M10-L grid are comparable to those of the Mach 7 ramp when expressed in units of the incoming boundary layer thickness. Both simulations are computed on wide domains where $L_y/\delta_o = 10$ for the purpose of minimizing any possible spanwise confinement effects on the separated flow region as was discussed in Section 2.5.

Case	ϕ	L_{x1}/δ_o	L_{x2}/δ_o	Δx^+	Δy^+	z_2^+	$N \times 10^6$	L_{sep}/δ	tU_{e}/δ	$tU_{\text{e}}/L_{\text{sep}}$
R33-M7-L	33^o	12.0	12.0	26.6-11.3	8.4	0.23	6.1	6.2	3153	511
R34-M10-L	34^o	13.0	12.0	27.7-10.5	7.1	0.20	51.8	4.1	451	110

Table 3.1: Hypersonic compression ramp simulation details.

The R33-M7-L flow was initialized from an instantaneous volume solution of the R8-M7-L dataset. The compression ramp angle was gradually increased from 8^o at startup to the final angle of 33^o, and the flow was allowed to develop through a transient until the separation length was no longer increasing in time. Once the separation region became established, the simulation was run for a duration of $3150\delta/U_e$ over which mean flow statistics were averaged. The mean separation length was measured to be 6.2δ. In terms of the mean separation length, the duration of the run is equivalently $510L_{sep}/U_e$. The R34-M10-L compression ramp was initialized in a similar way in that an instantaneous volume solution of the M10-L boundary layer was interpolated onto an 8^o ramp and the ramp angle was steadily increased until the final angle of 34^o was reached. The flow was then allowed to develop to its natural separation length. The R34-M10-L case was run at over twice the Reynolds number of the R8-M7-L case and, as a result, requires an order of magnitude increase in the number of grid points compared to R8-M7-L. Due to the greater computational cost, the Mach 10 simulation was only run for $450\delta/U_e$ over which mean statistics could be taken. Over this duration, the separation length averaged to 4.1δ resulting in a simulation duration of $110L_{sep}/U_e$.

The convergence of the mean flow statistics in separated STBLI is limited by the convergence of the low-frequency unsteadiness in the separation bubble which oscillates at frequencies much lower than those of the incoming turbulence. As was discussed in Section 2.5, the pre-multiplied power spectral density of the time signals of separation and reattachment provide information on the dominant frequencies in the interaction region turbulence. The pre-multiplied power spectra of the separation and reattachment points in the Mach 7 and in the Mach 10 data are plotted in Fig. 3.1. The spectra are normalized so that the area below a given curve sums to unity when integrated over the

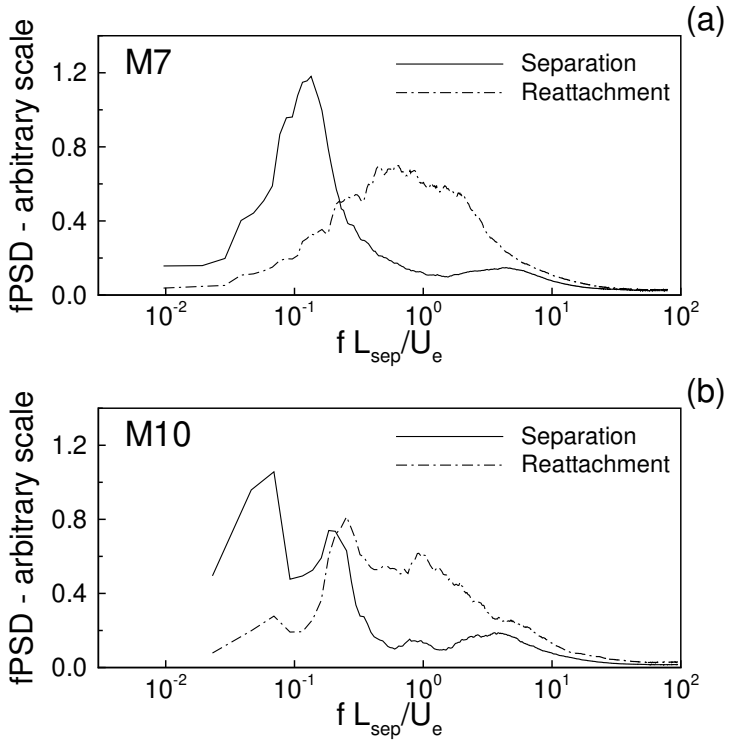

Figure 3.1: Premultiplied power spectral density of the time history of separation and reattachment in (a) R33-M7-L and (b) R34-M10-L.

logarithmic exponent of the frequency. The separation spectra are dominated by the energy in the lowest frequencies with very little energy in the fine-scale turbulence. The Mach 7 separation spectra in Fig. 3.1(a) shows a distinct low-frequency peak centered at $St_L = 0.1$ and significant energy at normalized frequencies as low as $St_L = 0.03$. Because of the shorter simulation duration, the lowest frequencies in the Mach 10 spectra shown in Fig. 3.1(b) are not as well converged as in the Mach 7 data; however, the dominant frequencies occur in the same range of St_L. Concerning the reattachment spectra, both cases show a broadband spread in energy centered at approximately $St_L = 1$. This wide energy band in the reattachment signal is seen to trail off on either side at the same frequencies that the high and low frequency energy peaks in the separation spectra trail off.

The lowest energized frequency of $St_L = 0.03$ in the separation region corresponds to a time scale of $33U_e/L_{sep}$. The Mach 7 dataset, therefore, contains at least 15 of these low-frequency cycles and the Mach 10 dataset at least 3. Samples of the separation and reattachment signals normalized by L_{sep} are plotted in Fig. 3.2 for both the Mach 7 and Mach 10 flows. Visual inspection suggests that the mean separation point is well defined by the sample length of $100L_{sep}/U_e$. If the full Mach 7 separation signal is split up into 10 overlapping segments of length $100L_{sep}/U_e$ and the average separation position $\overline{x}_s$ is calculated from each segment, we find that the largest error in $\overline{x}_s$ is within 3% of the full signal average with a standard deviation of 1.7%. We conclude that a duration of $100U_e/L_{sep}$, or approximately three low-frequency cycles, is sufficient for the convergence of the separated STBLI mean flow to within 3% error.

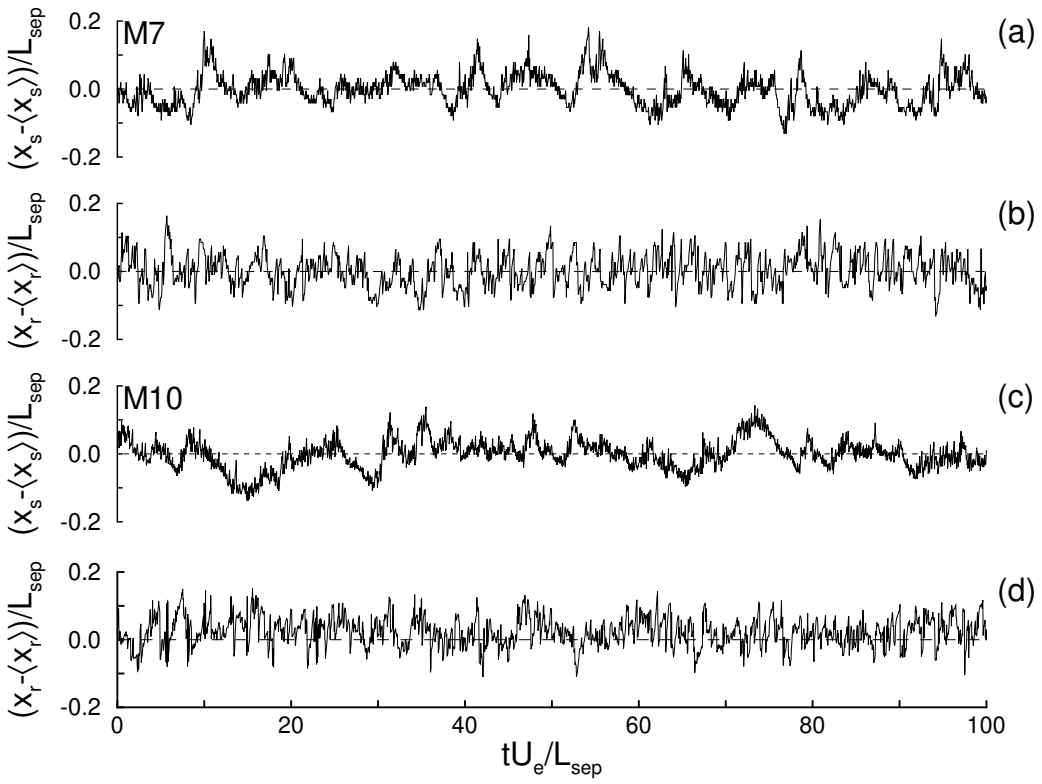

Figure 3.2: Sample time signals of spanwise-averaged separation and reattachment positions from R33-M7-L ((a) and (b) respectively) and from R34-M10-L ((c) and (d) respectively).

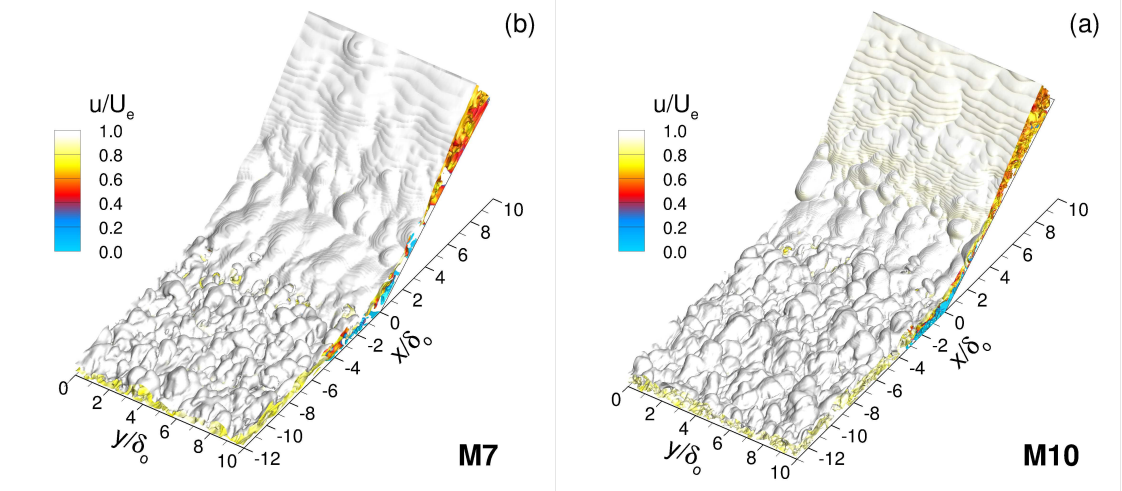

Figure 3.3: Instantaneous snapshot of the three-dimensional turbulence and shock front in (a) the R33-M7-L and (b) the R24-M10-L simulations. An isosurface of density gradient ($|\Delta\rho| = 0.7$) is colored by the magnitude of streamwise velocity. The flow direction is from the bottom left to top right of the image.

3.3 Flow Organization

The turbulence structure and flow organization of the R33-M7-L and R34-M10-L datasets are visualized in Fig. 3.3 by three-dimensional isosurfaces of the instantaneous density gradient. These isosurfaces are colored by the instantaneous streamwise velocity. The large-scale turbulence eddies in the incoming boundary layer appear as bulges in the isosurface. Reverse flow in the separation bubble can be seen as the area in blue at the corner. The isosurface also shows that the shock begins to form at a shallow angle inside of the turbulent boundary layer ahead of the separation bubble. This initial separation shock intersects the ramp surface and reflects off the wall to form the main oblique shock. The turbulence eddies in the incoming boundary layer appear to be heavily compressed below this point of reflection. A clear shift can be seen in the spatial scales of the turbulence from the incoming boundary layer eddies to the larger ripples in the shockwave above the separation bubble and just downstream of reattachment. This shift in scales was also noted by Wu & Martin [70] in the DNS of a Mach 3 compression ramp at similar conditions to the R24-M3n-D case from Section 2.5. In both flows, the main shock front becomes two-dimensional as it comes away from the ramp surface and exits the computational domain.

Many of these same features in the turbulence can also be seen in Fig. 3.4 which shows the instantaneous density field in an xz-plane cut through the center of the simulation span. The large eddies in the incoming boundary layer are seen as dark structures (lower density) and the shock front as the lighter features (higher density). The separation shock in the Mach 7 flow appears to come slightly away from the edge of the boundary layer before reflecting off the ramp surface. The separation shock of the Mach 10 flow,

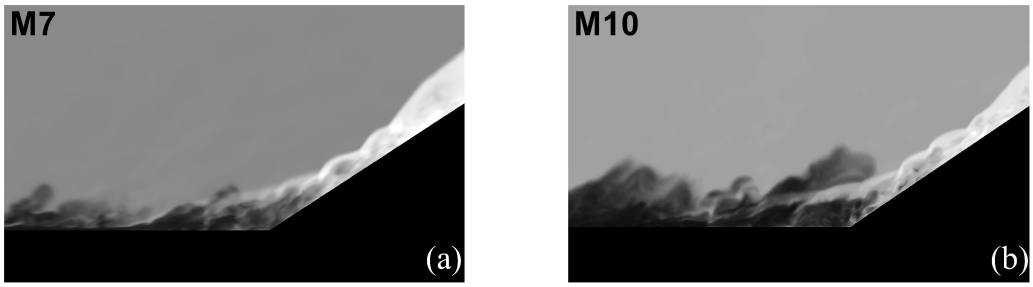

Figure 3.4: Instantaneous snapshot of density in an xz-plane through the center of the spanwidth of (a) the R33-M7-L and (b) the R34-M10-L.

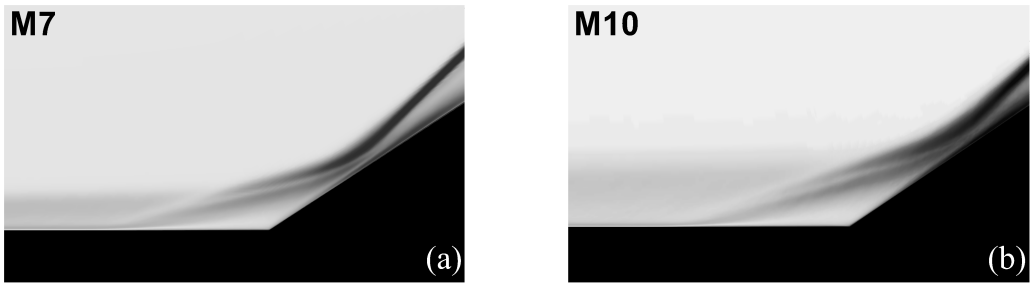

Figure 3.5: Time- and spanwise-averaged Numerical Schlieren of (a) R33-M7-L and (b) R34-M10-L. NS = $0.76\exp(-1.3|\nabla\overline{\rho}|/|\nabla\overline{\rho}|_{\max})$.

on the other hand, remains embedded in the turbulent boundary layer due to its smaller separation length. In Fig. 3.4, the shock front in both flows appears distorted by the turbulence structures in the separated region and near the shock reflection point on the ramp surface.

The time- and spanwise-averaged flowfields are visualized in Fig. 3.5 by what is referred to as a Numerical Schlieren, or the exponent of the mean density gradient field NS = $0.76\exp(-1.3|\nabla\overline{\rho}|/|\nabla\overline{\rho}|_{\max})$. In both mean flows, the angle that the main shock front makes to the freestream approaches the inviscid oblique shock solution as it comes away from the wall. The inviscid solution angle is 44^o for the Mach 7 configuration and 44.5^o for the Mach 10. Mean flow profiles taken from the exit plane of the computational domain

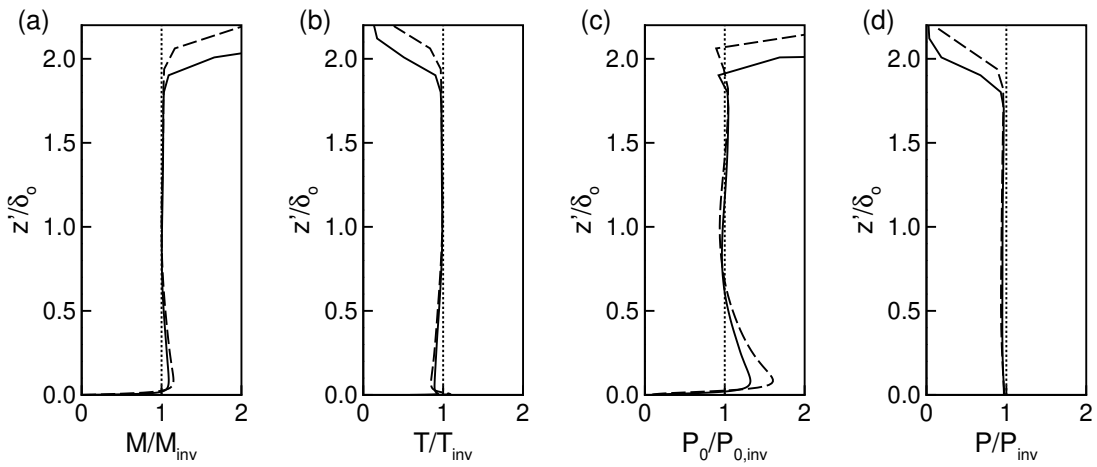

Figure 3.6: Post-shock profiles of (a) Mach number, (b) temperature, (c) total pressure, and (d) static pressure at the outlet plane of the computational domain. Profiles are normalized by the inviscid oblique shock solution. The dashed lines are the Mach 7 solution and the solid lines the Mach 10.

(Fig. 3.6) show that, outside of the boundary layer, the Mach number, temperature, and total pressure closely match the inviscid post-shock conditions. The downstream pressure comes just short of the oblique shock pressure jump. In Fig. 3.6, z' indicates the perpendicular distance from the ramp surface.

3.4 Mean Flow

Contour plots of the Favre-averaged velocities $\tilde{u}$ and $\tilde{w}$, the Favre-averaged temperature $\tilde{T}$, and the Reynolds-averaged density $\overline{\rho}$ of the R33-M7-L and R34-M10-L mean flowfields are shown in Fig. 3.7. The extent of the reverse flow region is visible as the red area (negative velocity) in Figs. 3.7 (a) and (b) of the Mach 7 and Mach 10 flows respectively. In both mean flow solutions, the maximum reverse flow is approximately 12% of U_e. The position of the averaged separation shock above the reverse flow region is visible in the contour plots of $\tilde{w}$ in Figs. 3.7 (c) and (d). A pocket of downward fluid motion on the aft end of the separation bubble is also visible. The temperature contours in Figs. 3.7(e) and

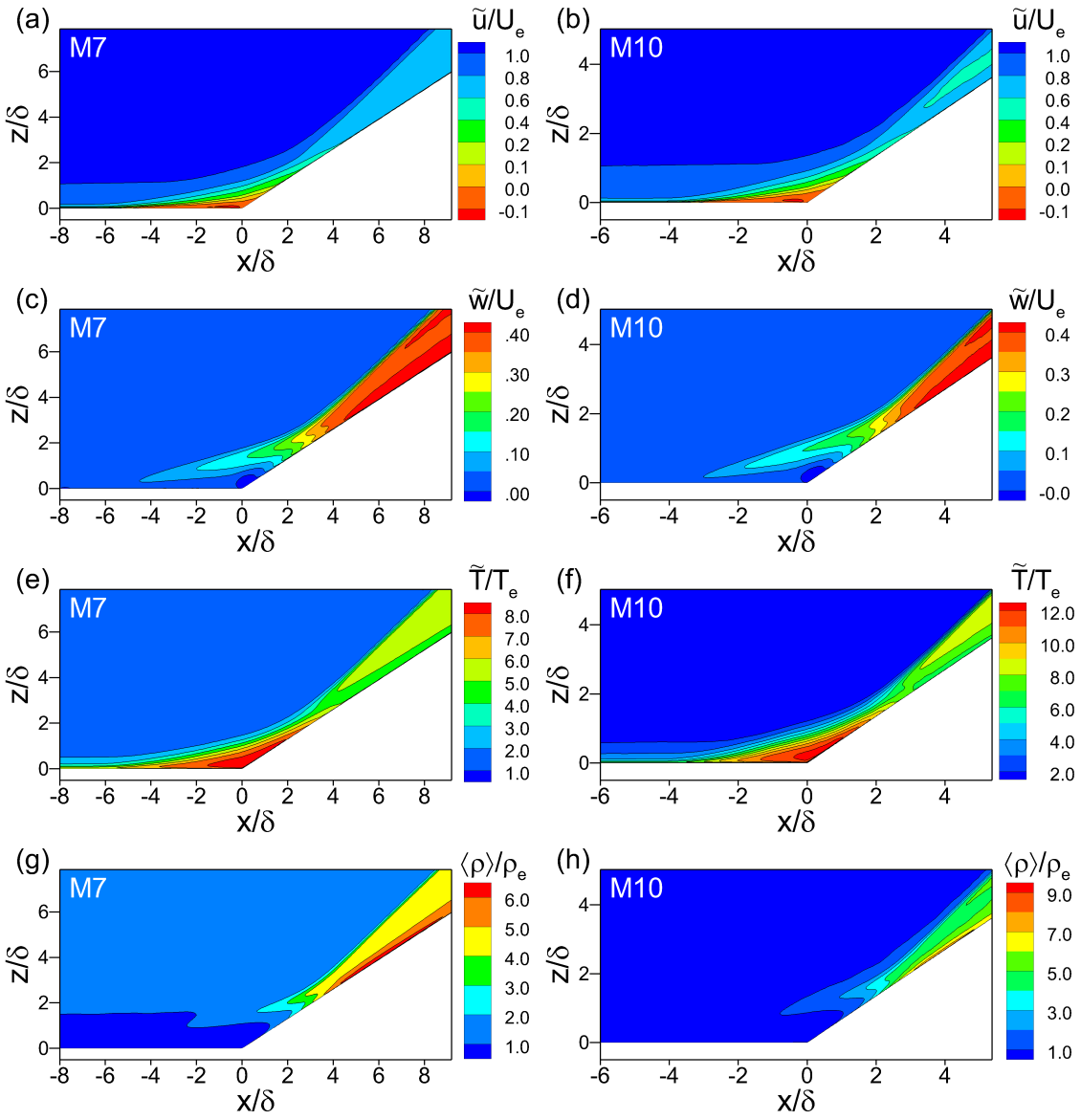

Figure 3.7: Contours of (a)-(b) Favre-averaged streamwise velcity $\tilde{u}$, (c)-(d) wall-normal velocity $\tilde{w}$, (e)-(f) temperature $\tilde{T}$, and (g)-(h) Reynolds averaged density $\langle\rho\rangle$ normalized by the freestream values. R33-M7-L are plotted on the left and R34-M10-L on the right.

(f) show that the maximum heating in the flow occurs inside the separation bubble in the dead air region. Here the Mach 7 mean flow experiences a maximum mean temperature of $8.7T_e$ and the Mach 10 a maximum of $12.5T_e$. Note that the heating inside the separation bubble exceeds the inviscid post-oblique shock temperature prediction of $5.7T_e$ (50% increase) for the Mach 7 condition and $8.7T_e$ (40% increase) for the Mach 10 condition. The contours of density in Figs. 3.7 (g) and (h) are found to change only slightly in the recirculation area. The peak value in mean density occurs in the downstream boundary layer near the wall surface reaching a peak of $6.5\rho_e$ on the Mach 7 ramp and $10.0\rho_e$ on the Mach 10 ramp. This increase in density at the wall exceeds the inviscid shock solution of $5.0\rho_e$ (30% increase) for the Mach 7 and $5.3\rho_e$ (90% increase) for the Mach 10.

The details of the mean flow fields are further highlighted by individual profiles of the velocity, temperature, and density. These profiles are plotted for R33-M7-L and R34-M10-L in Fig. 3.8. Profiles at four streamwise locations are shown and include the upstream undisturbed boundary layer ($x'/L_{sep} = -1.3$), mean separation ($x'/L_{sep} = -0.65$), the corner ($x'/L_{sep} = 0$), and the downstream recovering boundary layer ($x'/L_{sep} = 1.9$). The streamwise coordinate x' indicates the distance from the corner measured along the wall surface. The wall-normal coordinate z' is measured perpendicularly from the wall surface. This notation is maintained throughout the remainder of this article. Note that for the downstream boundary layer profiles, we rotate the velocity field coordinates so that $\tilde{u}$ represents the velocity component in the direction parallel to the ramp surface and $\tilde{w}$ the velocity component perpendicular to the ramp surface.

The profiles of $\tilde{u}$ (Fig. 3.8 (a) for the Mach 7 and Fig. 3.8 (e) for the Mach 10) show that the boundary layer thickness is significantly reduced in the downstream recovering boundary layer. The boundary layer begins to lift away from the wall at separation, as

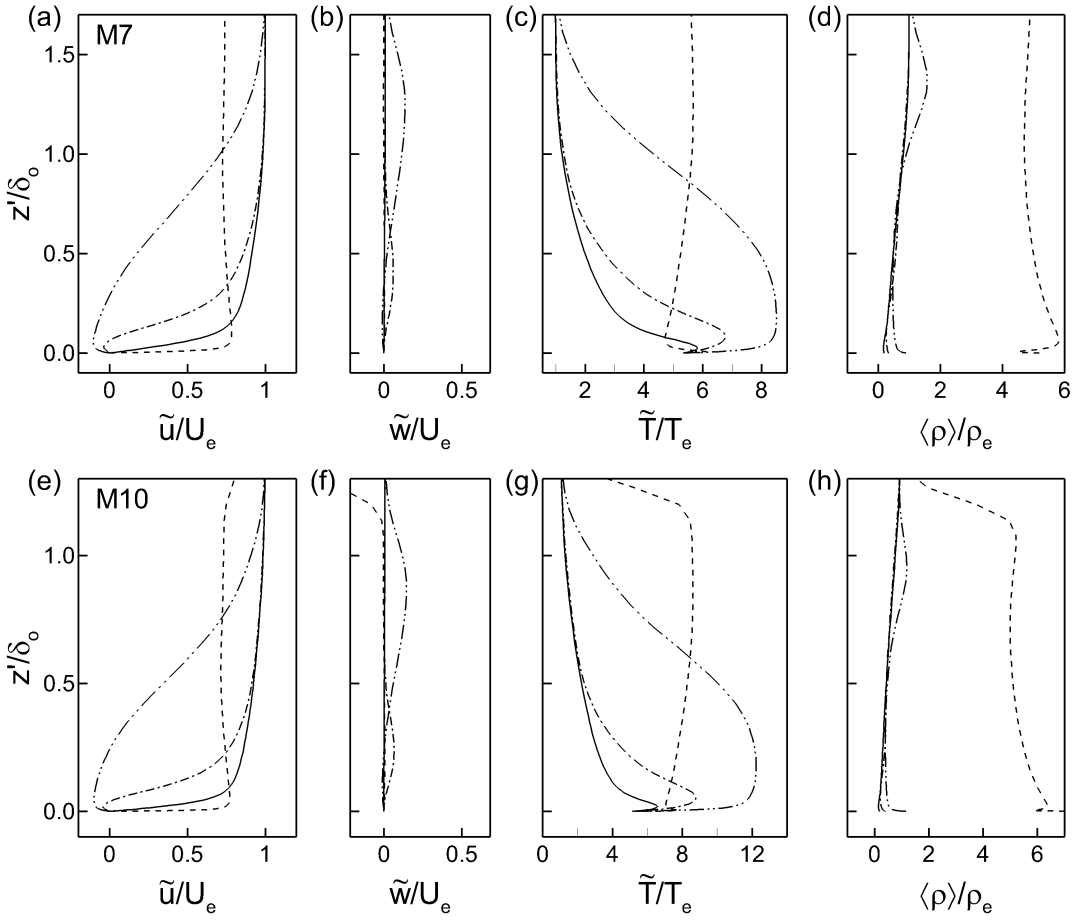

Figure 3.8: Individual profiles of (a),(e) Favre-averaged streamwise velocity $\tilde{u}$, (b),(f) wall-normal velocity $\tilde{w}$, (c),(g) temperature $\tilde{T}$, and (d),(h) Reynolds averaged density $\langle\rho\rangle$ normalized by the freestream values. The top row is R33-M7-L and the bottom row is R35-M10-L. Profile locations are upstream $x'/L_{sep} = -1.3$ (solid), separation $x'/L_{sep} = -0.65$ (dash-dot), corner $x'/L_{sep} = 0$ (dash-dot-dot), and downstream $x'/L_{sep} = -1.9$ (dashed).

indicated by the $\tilde{u}$ and $\tilde{w}$ profiles, and forms a mixing layer-type profile with a single inflection point in the center of the detached shear layer. The downstream $\tilde{w}$ profile returns to zero velocity as the flow adjusts to a direction parallel to the ramp surface. The temperature profile at the corner in panels (c) and (g) of Fig. 3.8 also develops a single inflection point profile that appears to be coincident with the streamwise velocity profile at the corner. The temperature in the downstream boundary layer experiences a very sharp positive gradient at the wall, which comes to a peak very close to the wall surface, followed by a decreases to nearly the post-shock freestream temperature. The density profiles in panels (d) and (h) of Fig. 3.8 show that the variation in density downstream is essentially a mirror image of the temperature profile. As was noted in Figs. 3.7 (g) and (h), the change in density is very small ahead of reattachment.

The mean wall pressure, skin friction, and heat transfer distributions are next plotted in Fig. 3.9. When plotted versus x'/L_{sep}, the two simulations have nearly identical distributions. In both flows, the pressure is seen to increase slightly at separation and then steeply at reattachment where it reaches a maximum before relaxing to the inviscid oblique shock solution. Downstream of the ramp, the wall pressure actually drops slightly below the inviscid level by 3%. This was also noted in the outlet profiles in Fig. 3.6 (d). In the Mach 7 mean flow, the pressure begins to increase ever so slightly just before reaching the domain outlet indicating that the boundary layer is not fully recovered yet. The 'rms' distributions of wall pressure are also included in Fig. 3.9 (a). The pressure fluctuations are essentially zero in the upstream boundary layer. Through the separation region, the variation in the P'_{rms} distribution follows the form of the mean pressure but decreases again as the boundary layer relaxes downstream. The maximum in P'_{rms} is slightly upstream of the maximum in P_w.

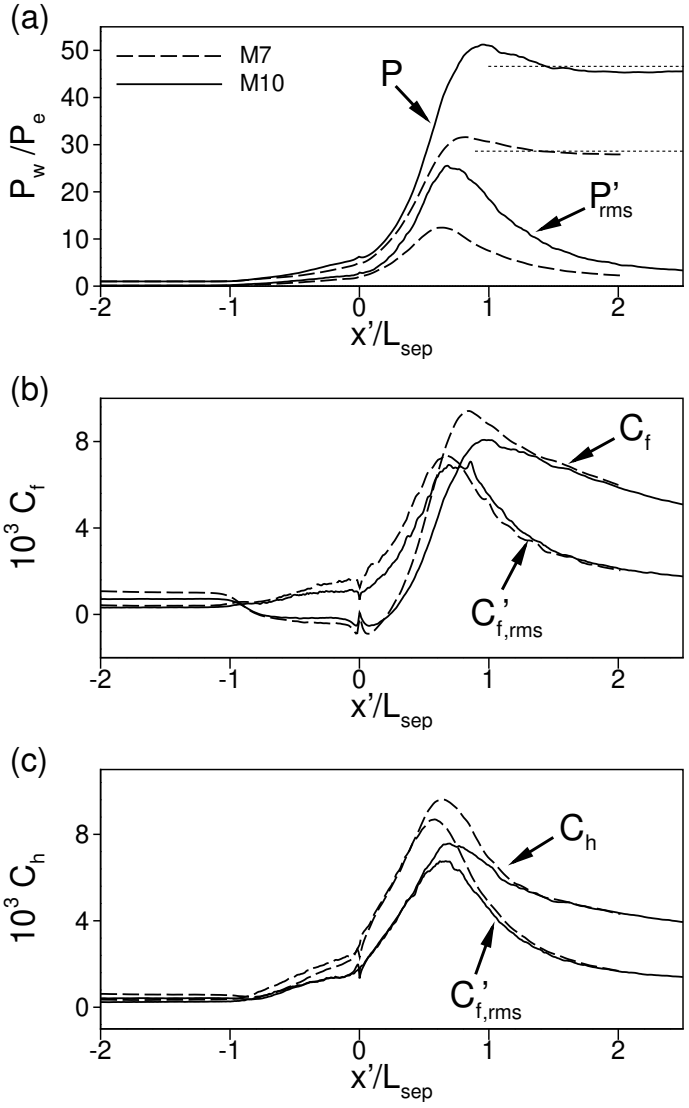

Figure 3.9: Time- and spanwise-averaged distributions of (a) wall pressure, (b) skin friction, and (c) heat transfer for R33-M7-L and R24-M10-L. The horizontal dashed lines in (a) indicate the inviscid shock pressure.

The distribution of mean skin friction coefficient C_f is plotted in Fig. 3.9 (b). The skin friction first decreases gradually just ahead of the separation point and drops below zero inside the separation bubble where it remains fairly constant up to the corner. Two sharp dips appear on either side of the corner as a result of the grid discontinuity. The C_f then increases rapidly, reaching a peak just downstream of reattachment and at the same location as the peak in P_w. It then steadily decreases as the reattached boundary layer begins to recover. In the Mach 7 distribution, C_f reaches a maximum of 9.3 times the level of the incoming boundary layer while the Mach 10 C_f distribution peaks at 11.3 times the incoming boundary level. The fluctuations in the skin friction $C'_{f,rms}$ are included in Fig. 3.9 (b). The fluctuating C_f increases gradually from separation to the corner and then increases rapidly to a peak downstream of reattachment followed by a steady decrease along the ramp. In both flows, the maximum in $C'_{f,rms}$ is found to be approximately 20 times the upstream level. In addition, the peak C_f occurs at the same streamwise location as the maximum in P_w while the peak in $C'_{f,rms}$ at the same location as the maximum in P'_{rms} for both the Mach 7 and Mach 10 interactions.

The wall heat transfer coefficient C_h distribution shown in Fig. 3.9 (c) experiences a slight dip at separation after which it increases first gradually and then more rapidly past the corner until it reaches a maximum on the ramp. It then steadily decreases downstream. The fluctuation magnitude $C'_{h,rms}$ is included in Fig. 3.9 (c) and is found to follow the same progression as C_h but at a somewhat lower magnitude. The coinciding maxima in C_h and $C'_{h,rms}$ occur just upstream of the peak in P_w but in-line with the peak in P'_{rms}. In the Mach 7 mean flow, the maximum heat transfer coefficient is 15.2 times the value of the incoming boundary layer and 2.2 times the value at the outlet plane. The amplification of heat transfer in the Mach 10 flow is 16.8 times the value in the incoming boundary layer

and 2.0 times the value measured at the outlet plane.

3.5 Turbulence Properties

In this section, the properties of the time- and spanwise-averaged turbulence stresses and turbulent kinetic energy budgets are discussed. Contours of the Favre-averaged Reynolds stress components $\sqrt{\widetilde{u''u''}}$, $\sqrt{\widetilde{v''v''}}$, $\sqrt{\widetilde{w''w''}}$, and $\widetilde{u''w''}$ normalized by the freestream velocity are plotted in Fig. 3.10. The streamwise turbulence intensity reaches its maximum amplification in the separation shear layer where it is found to be twice the upstream maximum in both flows. This strong amplification occurs almost immediately at separation and remains fairly constant throughout the detached shear layer. The contours show that v''_{rms} and w''_{rms} also increase in the separation shear layer. The maximum in v''_{rms} occurs at the wall surface in the vicinity of reattachment. Two local peaks occur in the contours of w''_{rms}, one just above the wall at reattachment and the second at the base of the main shock. The latter is a result of the fore and aft motions of the shock which cause w to oscillate between freestream ($w = 0$) and post-shock deflection velocity. The base of the main shock also appears in the contour of turbulence shear stress $\widetilde{u''w''}$ as a region of negative correlation due to a similar effect where the oscillations of u and w are out of phase across the shock. In the upstream boundary layer and in the separated shear layer, $\widetilde{u''w''}$ is negative as is expected for these types of shear flows. In both the Mach 7 and Mach 10 data, a strong positive amplification of $\widetilde{u''w''}$ occurs on the ramp surface near reattachment.

Profiles of each of the four stress components in Fig. 3.10 are plotted in Fig. 3.11. The individual profiles are taken from the same streamwise locations as in Fig. 3.8 from Section 3.4. The velocity axes are again rotated on the ramp surface so that u is in

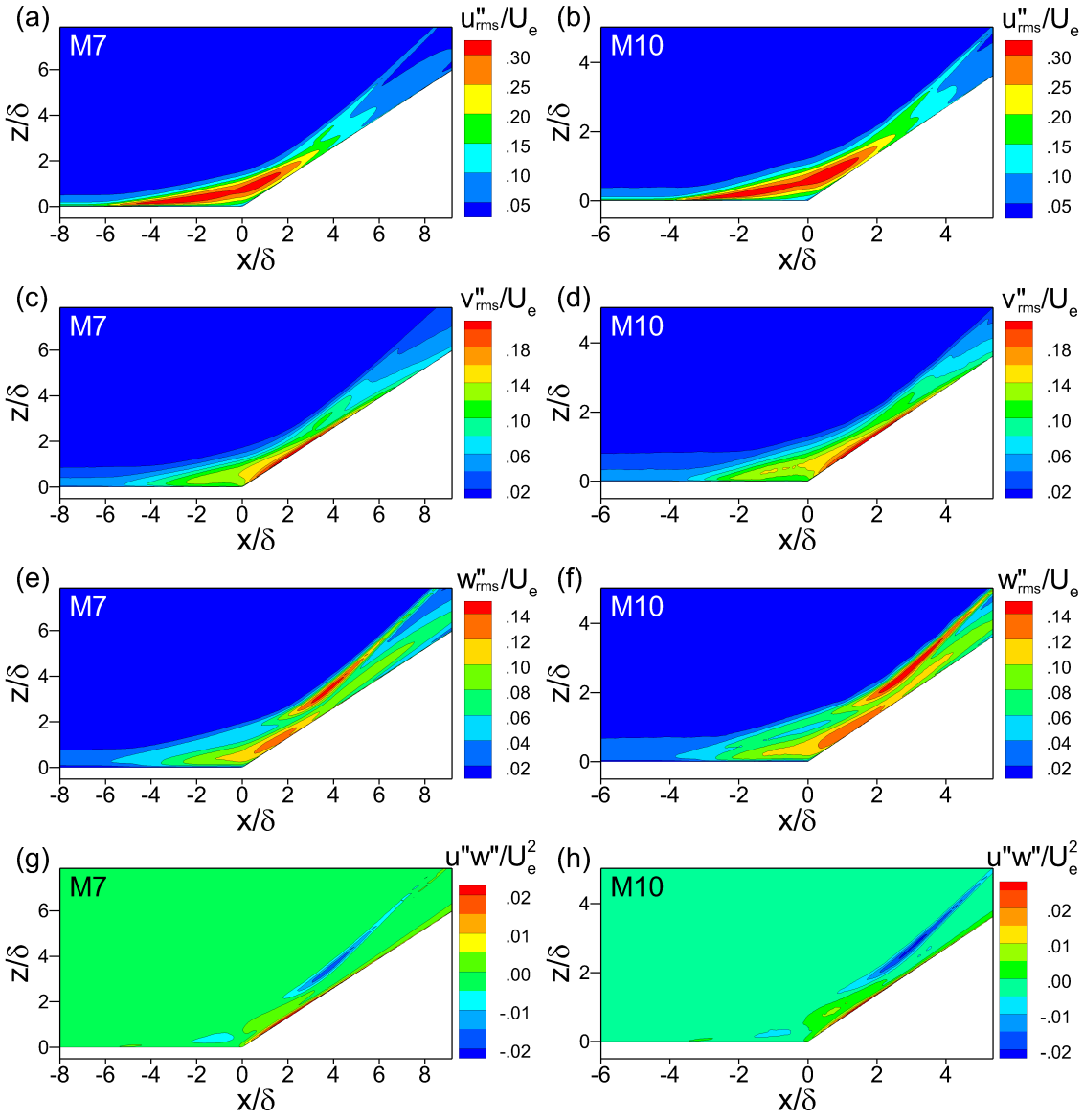

Figure 3.10: Contours of mean turbulence stress components (a)-(b) $\sqrt{\widetilde{u''u''}}$, (c)-(d) $\sqrt{\widetilde{v''v''}}$, (e)-(f) $\sqrt{\widetilde{w''w''}}$, and (g)-(h) $\widetilde{u''w''}$ normalized by the freestream values. R33-M7-L are plotted on the left and R34-M10-L on the right.

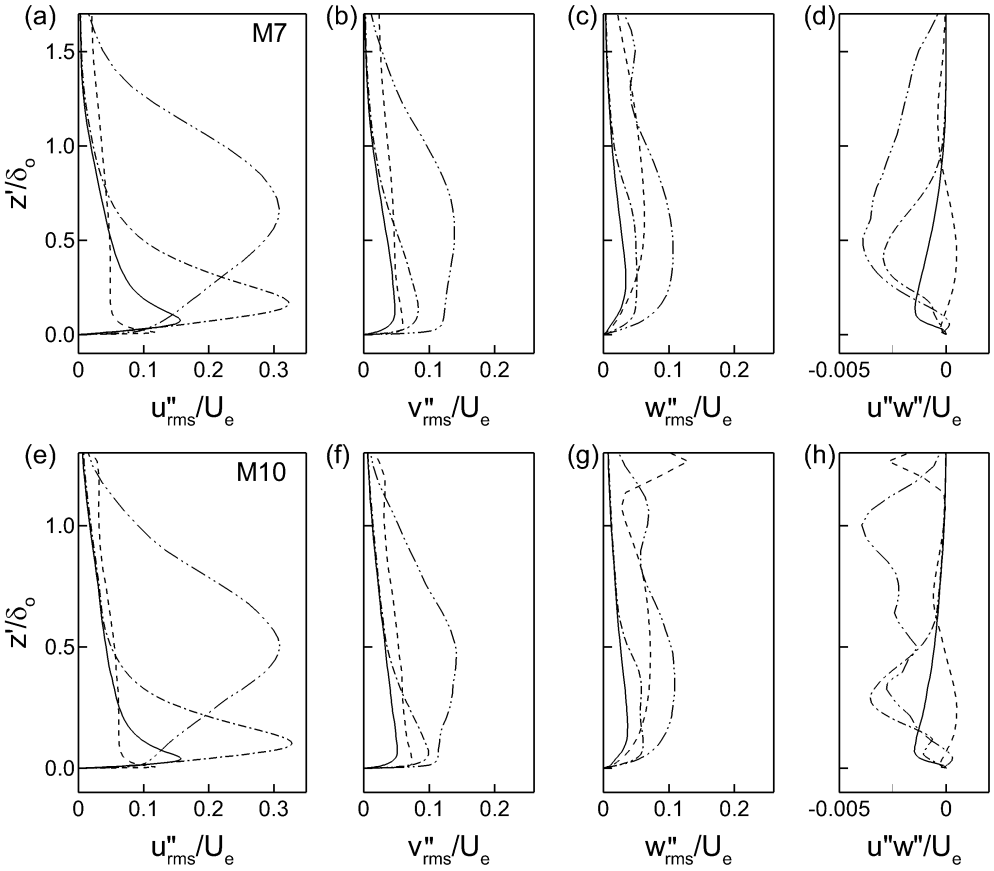

Figure 3.11: Individual profiles of turbulence stress components (a),(e) $\sqrt{\widetilde{u''u''}}$, (b),(f) $\sqrt{\widetilde{v''v''}}$, (c),(g) $\sqrt{\widetilde{w''w''}}$, and (d),(h) $\widetilde{u''w''}$ normalized by the freestream values. The top row is R33-M7-L and the top row is R34-M10-L. Profile locations are upstream $x'/L_{sep} = -1.3$ (solid), separation $x'/L_{sep} = -0.65$ (dash-dot), corner $x'/L_{sep} = 0$ (dash-dot-dot), and downstream $x'/L_{sep} = -1.9$ (dashed).

the plane parallel to the ramp and w is perpendicular to the ramp. In the profiles of streamwise turbulence, the upstream turbulence peak increases in magnitude and shifts away from the wall at separation. At the corner, the streamwise turbulence peak is greatly thickened but the maximum value does not change significantly from that at separation. The location in z' of the $\sqrt{\widetilde{u''u''}}$ peak in the corner profile coincides with the z' location of the inflection point in the corner mean velocity profile shown in Fig. 3.8 (a) for the Mach 7 and Fig. 3.8 (e) for the Mach 10 flow. The magnitude of the streamwise turbulence is significantly reduced in the downstream boundary layer and the peak is compressed very close to the wall surface. The v''_{rms}, w''_{rms}, and $\widetilde{u''w''}$ turbulent stresses also show an increase through the shear layer. The magnitude of v''_{rms} and w''_{rms} decrease again in the most downstream profiles. The $\widetilde{u''w''}$ component is seen to reverse sign in the recovering boundary layer. The downstream profiles show that all four turbulence stresses maintain an elevated turbulence level outside the region of high shear at the wall, that is, above the compressed local boundary layer thickness. This feature can also be seen in the contour plots of Fig. 3.10 as a band of elevated turbulence parallel to the ramp surface beneath the main shock. This band of elevated turbulence appears to decay gradually downstream.

The state of the turbulence stresses is further investigated by analyzing the principle invariants of the anisotropy tensor. The anisotropy tensor is defined as $b_{ij} = \widetilde{u''_i u''_j}/2k - \delta_{ij}/3$ where $k = \widetilde{u''_i u''_i}/2$ and δ_{ij} is the Kroneker function. Because b_{ij} is deviatoric, only the second and third invariants are non-zero. These are by definition $\mathrm{II} = -b_{ij}b_{ji}/2$ and $\mathrm{III} = b_{ij}b_{jk}b_{kl}/3$. The mapping of these two non-zero invariants are generally plotted together with the so-called Lumley triangle which represents the range of values of II and III that are physically possible for a given flow [71, 72]. The invariant mappings of both the Mach 7 and Mach 10 at the same wall-normal profiles of Fig. 3.8 are shown together

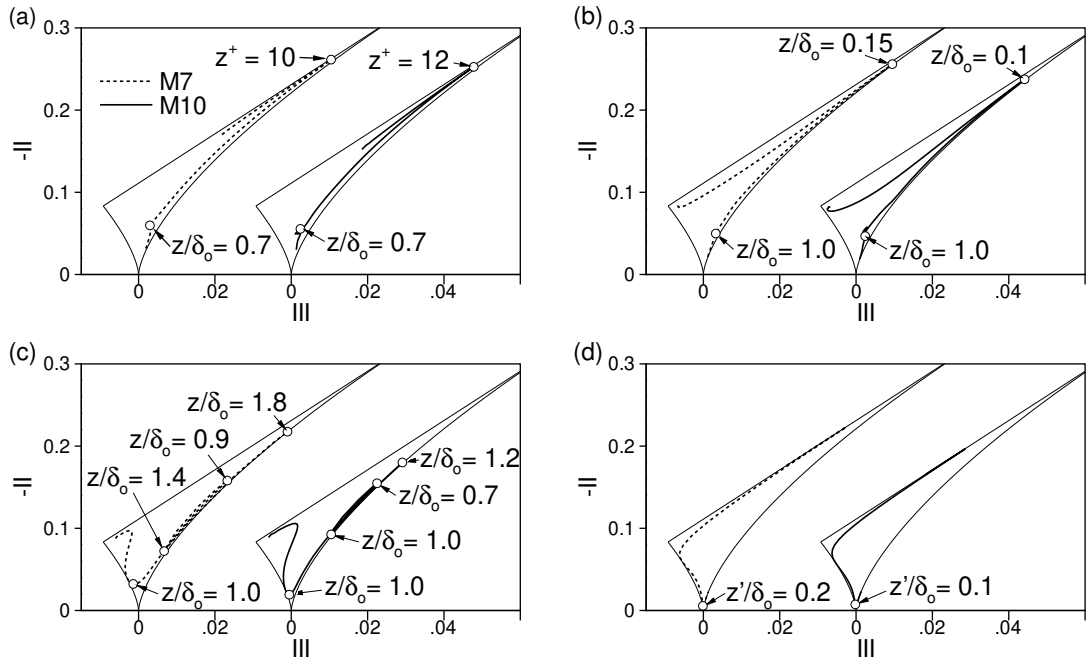

Figure 3.12: Lumley triangles for wall-normal profiles (a) in the incoming boundary layer $x'/L_{sep} = -1.3$, (b) at mean separation $x'/L_{sep} = -0.65$, (c) at the corner $x'/L_{sep} = 0$, and (b) in the downstream boundary layer $x'/L_{sep} = 1.9$.

in 3.12. The upstream trajectories of the upstream boundary layers shown in Fig. 3.12 (a) are typical of turbulent boundary layer data [71]. The top branch of the Lumley triangle represents two-component turbulence which is realized in the boundary layer at the wall due to the constraint the wall imposes on the w fluctuations. The top right corner of the Lumley triangle represents one-component turbulence which occurs in the boundary layer at $z^+ \approx 10$ where u''_{rms} is at its maximum value. The bottom right side of the triangle is the boundary of axisymmetric turbulence expansion which is characteristic of the logarithmic layer. Near the boundary layer edge, the turbulence approaches isotropic conditions where II = III = 0. At the corner between $z/\delta = 0$ and 1, the invariant pair moves towards the bottom left branch of the Lumley triangle and towards isotropy. The left side of the triangle represents axisymmetric turbulence compression and is typical of mixing layer data [71]. In the downstream profile, the invariant pair remains on the

top and left boundaries in the region of high shear at the wall and moves to isotropic conditions outside of the local boundary layer thickness.

Next the turbulent kinetic energy budgets through the interactions are analyzed. For this purpose we use the TKE of the Favre fluctuation velocity such that $k = \langle \rho u_i'' u_i'' \rangle / 2$. The transport equation for k is included in Appendix A Eqn. A.1. The TKE budgets are plotted for R33-M7-L and R34-M10-L in Fig. 3.13. The streamwise stations at which each set of budget profiles were taken are the same four locations as were used in Figs. 3.10, 3.11, and 3.12. The wall-normal coordinate is nondimentionalized by z_τ and the budget terms by $\rho_w u_\tau^3 / z_\tau$ where z_τ, u_τ and ρ_w are the values from the upstream undisturbed boundary layer. The SGS terms in Fig. 3.13 are calculated as the remainder of the sum of all other budget terms and represent the combined contribution of the SGS diffusion and SGS dissipation terms.

The upstream boundary layer TKE budgets shown in Fig. 3.13 (a) and (b) are typical of compressible turbulent boundary layers with zero pressure gradient [73, 74]. The production is balanced by the turbulent transport, diffusion, and dissipation with all other terms being relatively insignificant. The peak in production occurs at $z^+ = 14$ for the Mach 7 boundary layer and at $z^+ = 17$ for the Mach 10 as the greater wall cooling tends to push the turbulence production peak away from the wall [73]. At separation (Fig. 3.13 (c) and (d)), the magnitude of both the production and transport terms are greatly increased from the incoming flow. The peaks in these two quantities come away from the wall in a manner consistent with similar observations in the velocity profiles of Fig. 3.8 and in the turbulence stress profiles of Fig. 3.11. The turning of the fluid at separation results in a non-zero convection term that is balanced by an increase in the turbulence transport. Production is further increased in the corner profiles of Fig. 3.13 (e) and (f). The production peak

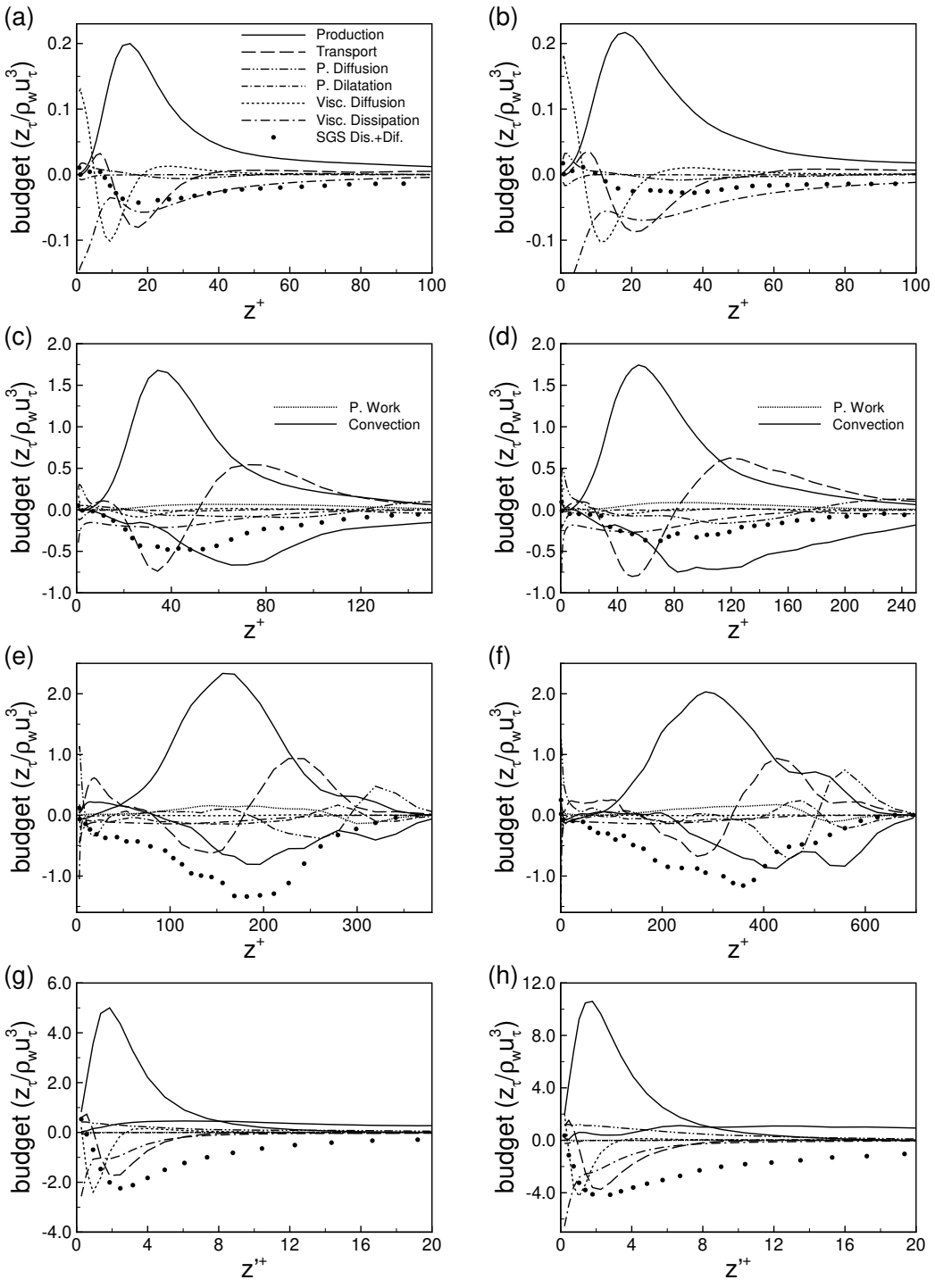

Figure 3.13: Profiles of TKE budgets in (a)-(b) the upstream boundary layer $x'/L_{sep} = -1.3$, (c)-(d) at mean separation $x'/L_{sep} = -0.65$, (e)-(f) at the corner $x'/L_{sep} = 0$, and (g)-(h), in the downstream boundary layer $x'/L_{sep} = 1.9$. The budget profiles for R33-M7-L are on the left and R34-M10-L on the right.

is greatly widened at the corner and occurs in the wall-normal vicinity of the shear layer center. (Note that $z/\delta = 1$ is equivalent to $z^+ = 200$ in the Mach 7 flow and $z^+ = 500$ in the Mach 10 flow.) The increase in production in the separation shear layer is balanced by increases in turbulence transport, convection, pressure diffusion, and dissipation. Here the increase in dissipation is found to be predominantly in the SGS. In the downstream boundary layer (Fig. 3.13 (g) and (h)), the production, transport, and convection terms are increased significantly at the wall due to the strength of the mean shear in this region. This is consistent with the high shear at the wall shown in the velocity profiles of Fig. 3.8 (a) and (e) and the near-wall turbulence peak in Fig. 3.11 (a) and (e). Overall, the pressure work term is seen to increase to a non-zero value at separation and in the recirculation region but its contribution is not significant. Likewise the pressure dilatation remains small throughout both the Mach 7 and Mach 10 mean flows. The budget magnitudes in the boundary layer, at separation, and the corner are comparable between the Mach 7 and Mach 10 solutions. In the downstream flow, however, the turbulence production of the Mach 10 is twice that of the Mach 7.

3.6 Assessment of Turbulence Modeling Assumptions

We use the R33-M7-L and R34-M10-L data to evaluate several practical turbulence modeling assumptions and their applicability to these separated hypersonic STBLI flows. Two scaling laws for the prediction of the mean heat transfer at the wall are tested. The first of these is the assumption that the Reynolds Analogy Factor, defined as the ratio $\mathrm{RAF} = 2C_h/C_f$, is approximately unity. This ratio in the LES data is plotted as RAF^{-1} in Fig. 3.14 to avoid the division by zero C_f. The results are nearly identical between the Mach 7 and Mach 10 interactions. The RAF^{-1} is 0.85 in the boundary layer upstream

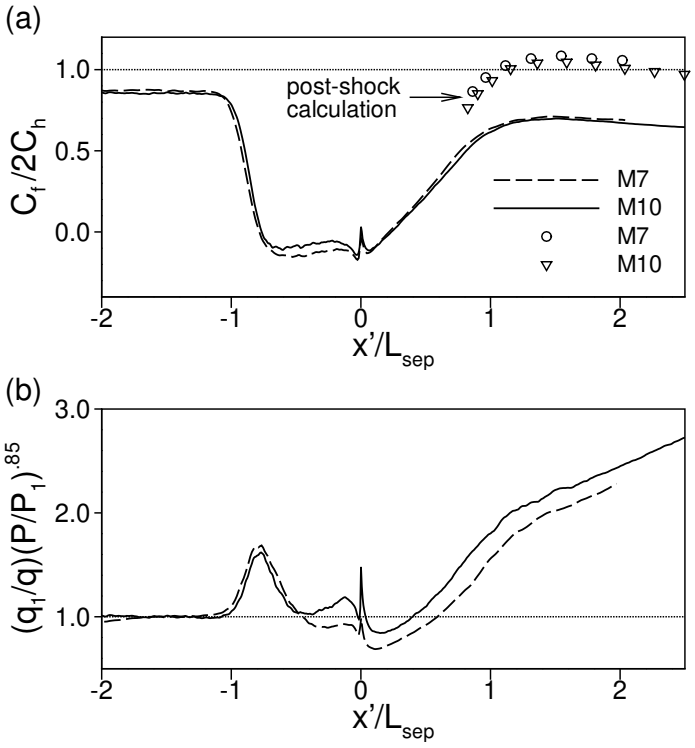

Figure 3.14: Streamwise distributions of (a) the (inverse) Reynolds Analogy Factor and (b) the QP85 law of Back & Cuffel [69] for R33-M7-L and R24-M10-L.

of separation and approximately 0.7 in the downstream reattached boundary layer. The assumption of RAF ≈ 1 does not hold in the separated region.

The Reynolds Analogy Factor can equivalently be written as RAF $= q_w C_p (T_w - T_r)/\tau_w U_e$. The line distributions in 3.14 (a) were calculated using U_e and T_r of the upstream boundary layer throughout. If instead the RAF in the downstream flow is calculated using values of U_e and T_r estimated from the inviscid oblique shock solution, the result is the distribution indicated by the symbols in 3.14 (a). The RAF^{-1} distributions calculated using the post-shock conditions show a slight over-shoot of 1 followed by what appears to be a gradual decrease to 1.

The second heat transfer model considered is the so-called QP85 law of Back & Cuffel [69] relating the mean distribution of wall heat transfer to the distribution of mean wall pressure by $q(x)/q_u = (P(x)/P_u)^{0.85}$. The subscript u refers to a quantity in the upstream undisturbed boundary layer. In Fig. 3.14 (b) is plotted the QP85 prediction as a fraction of the measured $q(x)$ of the LES solutions. The two STBLI flows show nearly identical results with the Mach 10 having greater relative heat transfer downstream of the separation region. It was noted in 3.12 (c) that the C_h dips slightly at separation but the same feature does not occur in the wall pressure shown in Fig. 3.12 (a). Consistent with this observation, the QP85 relation over-predicts the heat transfer at separation. The steep increase in heat transfer that occurs just downstream of the corner is also not well predicted by the QP85 relation. In the downstream recovering boundary layer, the heat transfer is significantly over-predicted and this error increases steadily up to the simulation exit plane. These results are not surprising as this relation was derived for attached shock/turbulent boundary layer interactions. Coleman & Stollery [75] derived a similar relation between $q(x)$ and $P(x)$ and these authors also noted that the relation

was only accurate for predicting their experimental heat transfer data for attached and incipiently separated compression ramp experiments with a freestream Mach number of 9.

Next we test the validity of the set of modeling assumptions collectively known as the Strong Reynolds Analogies relating the temperature fluctuations to the velocity fluctuations in compressible turbulent boundary layers. The Strong Reynolds Analogies were originally proposed by Morkovin [76] and include the turbulent Prandtl number relation (Eqn. 3.1), the phase relation (Eqn. 3.2), and the magnitude relation (Eqn. 3.3).

$$Pr_t = \frac{\widetilde{\rho u'' w''}}{\widetilde{\rho T'' w''}} \frac{\partial \tilde{T}/\partial z'}{\partial \tilde{u}/\partial z'} \approx 1, \tag{3.1}$$

$$-R_{u''T''} = -\frac{\langle u'' T'' \rangle}{u''_{\text{rms}} T''_{\text{rms}}} \approx 1, \tag{3.2}$$

$$\text{SRA} = \frac{T''_{\text{urms}}/\tilde{T}}{(\gamma - 1) M^2 (u''_{\text{rms}}/\tilde{u})} \approx 1. \tag{3.3}$$

We evaluate Eqns. 3.1, 3.2, and 3.3 in both the upstream undisturbed boundary layers and in the downstream recovering boundary layers of the R33-M7-L and R34-M10-L data. Upstream profiles were taken at $x'/L_{sep} = -1.3$ and downstream profiles at $x'/L_{sep} = 1.9$, the same upstream and downstream locations that were used for the TKE and anisotropy analyses in Section 3.5. For the evaluation of the Strong Reynolds Analogies in the downstream recovering boundary layer, the velocity field is again rotated so that u is in the direction parallel to the ramp surface and w is perpendicular.

The turbulent Prandtl number Pr_t is defined in Eqn. 3.1 as the ratio of turbulent transport of momentum to turbulent transport of heat flux and is typically assumed constant and equal to 1 throughout the boundary layer. Profiles of the Prandtl number in

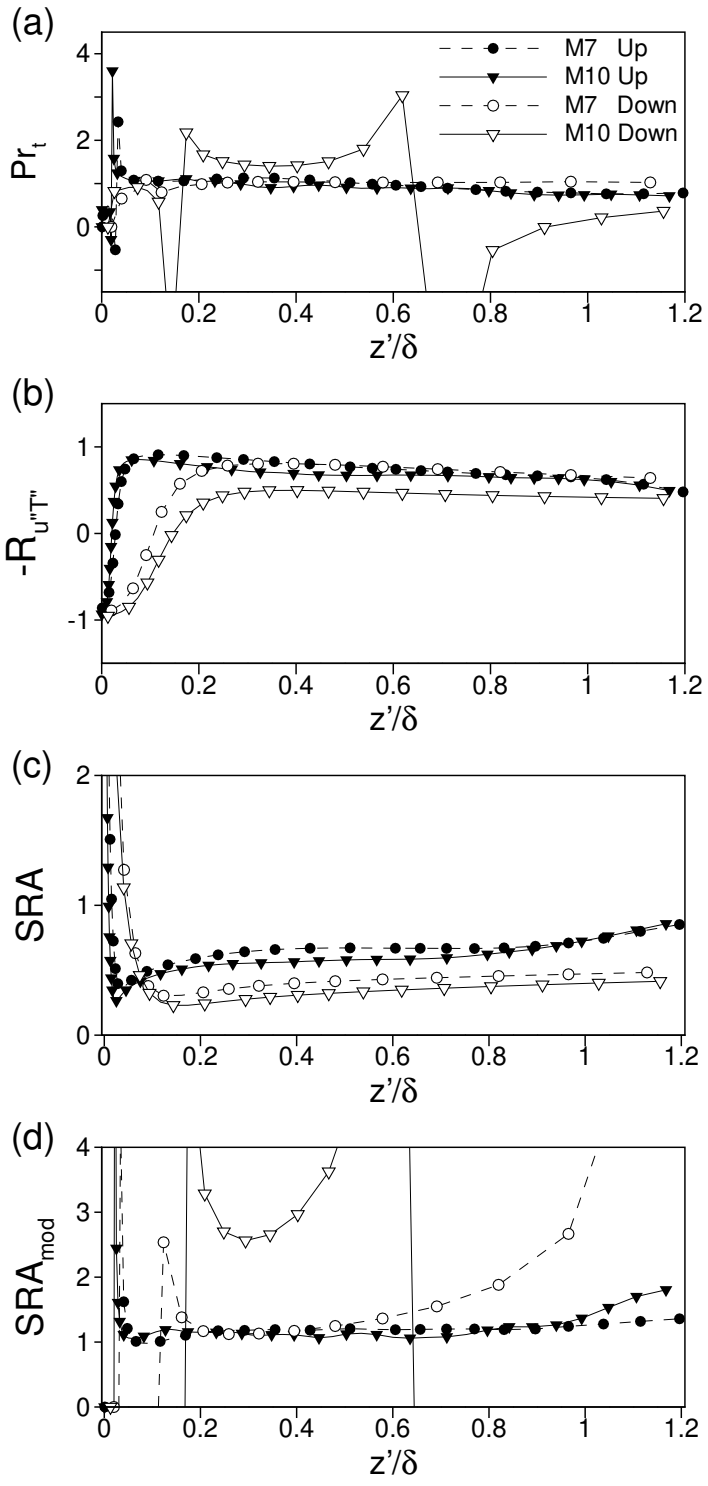

Figure 3.15: Upstream ($x'/L_{sep} = -1.3$) and downstream boundary ($x'/L_{sep} = 1.9$) layer profiles of (a) turbulent Prandtl number Pr_t, (b) Strong Reynolds Analogy (SRA) phase relation, (c) SRA magnitude relation, and (d) modified SRA magnitude relation.

the mean flow of the R33-M7-L and R34-M10-L LES solutions are plotted in Fig. 3.15. These profiles are plotted versus wall-normal distance z' non-dimensionalized by the local boundary layer thickness δ_x. In the upstream boundary layers, Pr_t is within 13% of 1 between $z'/\delta_x = 0.05$ and 0.75. At the boundary layer edge, $Pr_t = 0.75$. Below $z'/\delta_x = 0.05$ the assumption of constant Pr_t does not hold. In the M7 recovering boundary layer, it is found that $Pr_t \approx 1.0$ for $z'/\delta_x > 0.1$. In the M10 downstream profile, near $z'/\delta_x = 0.1$ the Pr_t is nearly 1. Between $z'/\delta_x = 0.3$ to 0.5, Pr_t is approximately 1.4.

For undisturbed adiabatic turbulent boundary layers, the DNS data analysis of Duan *et al.* [74] has shown that the phase relation correlation $-R_{u''T''}$ is approximately 0.6 through the majority of the compressible boundary layer and that this level does not change with freestream Mach number, at least up to $M_e = 12$. The value of 0.6 is consistent with other DNS studies [77, 78]. In addition, Duan *et al.* [73] showed the correlation reduces only slightly with decreasing T_w/T_r. The profiles of $-R_{u''T}$ for the current LES data are plotted in Fig. 3.15 (b). In the upstream profiles of both the Mach 7 and Mach 10 boundary layers, $-R_{u''T''}$ drops from 0.85 at $z'/\delta_x = 0.05$ to 0.6 at the boundary layer edge. A shift to negative correlation at the wall indicates that the temperature-velocity phase relation is reversed here. The profile of $-R_{u''T''}$ in the Mach 7 downstream profile, when z' is normalized by the local boundary layer thickness, is very similar to the upstream profile for $z'/\delta_x > 0.2$. In the Mach 10 solution, however, the magnitude of $-R_{u''T''}$ reduces to approximately 0.5 in the downstream profile. Although not shown here, the zero crossing of $-R_{u''T''}$ in each of the four profiles was found to closely correspond to the location of the peak in the mean temperature profile.

The magnitude relation of Eqn. 3.3 is plotted for the two LES solutions in Fig. 3.15 (c). In the Mach 7 flow, the SRA = 0.65 in the upstream boundary layer and decreases to

0.4 in the downstream boundary layer. In the Mach 10 flow, the SRA = 0.6 upstream and decreases to 0.35 downstream. In all four profiles, the SRA drops to a minimum of about 0.3 near the wall and then increases asymptotically to infinity at the wall surface. The fact that the assumption of SRA ≈ 1 does not hold for these two flows is not surprising as the relation of Eqn. 3.3 was originally derived for an adiabatic boundary layer. Huang *et al.* [79] derived the following modified Strong Reynolds Analogy that accounts for heat transfer at the wall.

$$\mathrm{SRA}_{\mathrm{mod}} = \frac{(T''_{\mathrm{urms}}/\tilde{T})Pr_t(1-\partial\tilde{T}_t/\partial\tilde{T})}{(\gamma-1)M^2(u''_{\mathrm{rms}}/\tilde{u})} \approx 1. \tag{3.4}$$

The variable $\tilde{T}_t$ is the total temperature, which for the LES solution is calculated from the Favre filtered $\tilde{u}$ and $\tilde{T}$. Similar expressions were also proposed by Gaviglio [80] and by Rubesin [81]. The profiles of the $\mathrm{SRA}_{\mathrm{mod}}$ are plotted in Fig. 3.15 (d). The upstream profiles of the Mach 7 and Mach 10 flows both take on a value of 1.2 between $z'/\delta_x = 0.1$ and 1.0. In the downstream flow, the Mach 7 profile drops to 1.2 only between $z'/\delta_x = 0.2$ and 0.5. The $\mathrm{SRA}_{\mathrm{mod}}$ relation does not hold for the Mach 10 recovering boundary layer.

3.7 On the scale-similar SGS model

This section discusses the importance of including a scale-similar term in the SGS turbulence stress (Eqn. 2.9) and the SGS heat transfer (Eqn. 2.10). Eddy viscosity models only account for the dissipative drain of energy from the resolved scales to the unresolved scales. Scale-similar models were originally derived under the assumption that the most active SGS are those just below the cutoff frequency of the LES [82] and so are designed to approximate the local exchange of energy between the smallest resolved scales and the

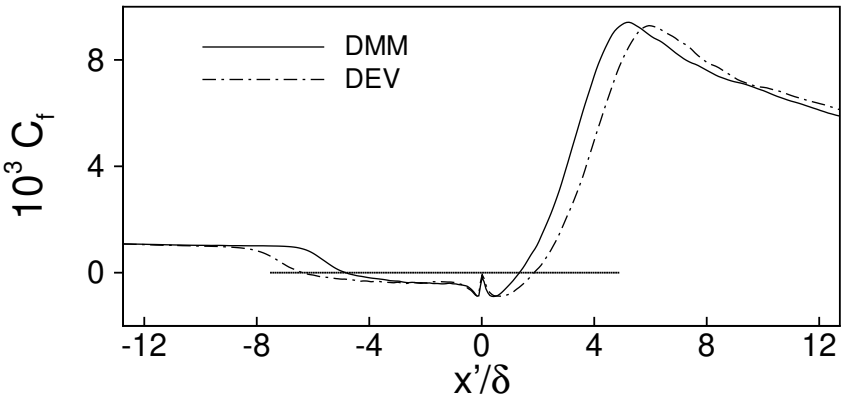

Figure 3.16: Skin friction comparison of DMM and DEV solutions of R33-M7-L.

SGS. The scale-similar models, however, tend to underestimate the SGS dissipation [52]. In combination, the scale-similar term accounts for the conservative energy exchange at the smallest resolved scales and the eddy viscosity term accounts for the dissipative energy drain of the SGS. In a study of decaying isotropic compressible turbulence, Martin *et al.* [52] reported better correlations of SGS shear stress and heat flux using the mixed model in comparison to the eddy viscosity only model.

To demonstrate the importance of using the dynamic mixed model (DMM) rather than the dynamic eddy viscosity model (DEV) for the solution of the STBLI flows, we repeat several of the simulations in this paper with the scale-similar terms in Eqns. 2.9 and 2.10 turned off and using only the dynamic coefficient eddy viscosity models. We first repeated simulations R24-M3w-L from Section 2.5 and R8-M7-L from Section 2.6 and in both cases the result was to slightly increase the length of the interaction region. The difference was found to be minor, however, with less than 5% increase in the Mach 3 separation length and an increase from 31% to 35% in the maximum reverse probability at the corner of the Mach 7. In contrast, we repeated the R33-M7-L solution with the SGS scale similar contributions removed and found that the separation length increased by 30%.

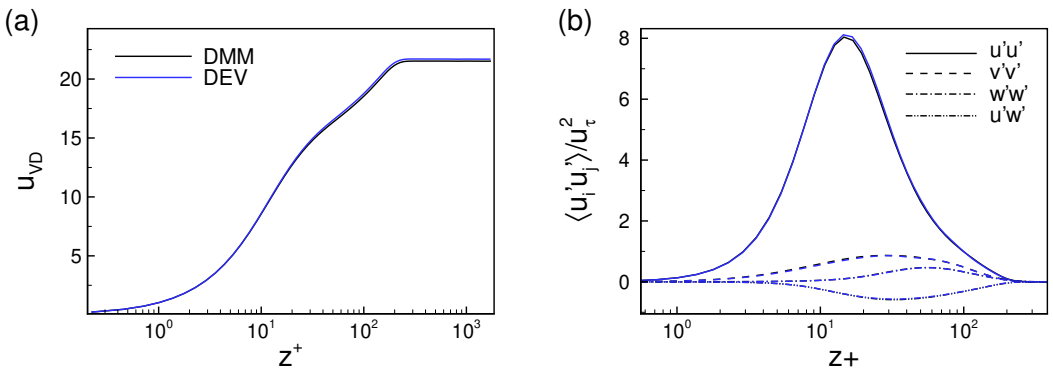

Figure 3.17: Comparison of DMM and DEV upstream boundary layer solutions of R33-M7-L (a) van Driest transformed velocity, and (b) turbulence intensities. Legend as in Fig. 3.13.

This dramatic difference is shown in the comparison of mean skin friction distributions between the original Mach 7 DMM solution and the DEV solution (Fig. 3.16).

Profiles of the upstream boundary layer indicate that the source of the error in the Mach 7 separation length is not from a change in the state of the incoming boundary layer. The comparison of van Driest transformed velocity profiles taken in the upstream boundary layers at $x/L_{sep} = -1.7$ are shown in Fig. 3.17 (a). The comparison of turbulence Reynolds stress profiles at the same location are shown in Fig. 3.17 (b).

Instead, the results indicate that the difference between the two solutions resides in the STBLI separation shear layer. We estimate the spreading rate of the separation shear layers in each of the separated hypersonic flow solutions using a method that is given in detail in Chapter 6 and also in Helm & Martin [83]. In short, a shear layer coordinate system $(x_{\mathrm{ml}}, z_{\mathrm{ml}})$ is considered for which the linearly varying similarity variable $\zeta = z_{\mathrm{ml}}/x_{\mathrm{ml}}$ can be defined. Plotting mean flow profiles in the shear layer versus ζ results in what resemble collapsed mixing layer similarity profiles.

The difference in the shear layers of the DMM and DEV solutions is highlighted by plotting the resulting collapsed shear layer profiles scaled by ζ. In Fig. 3.18 are shown

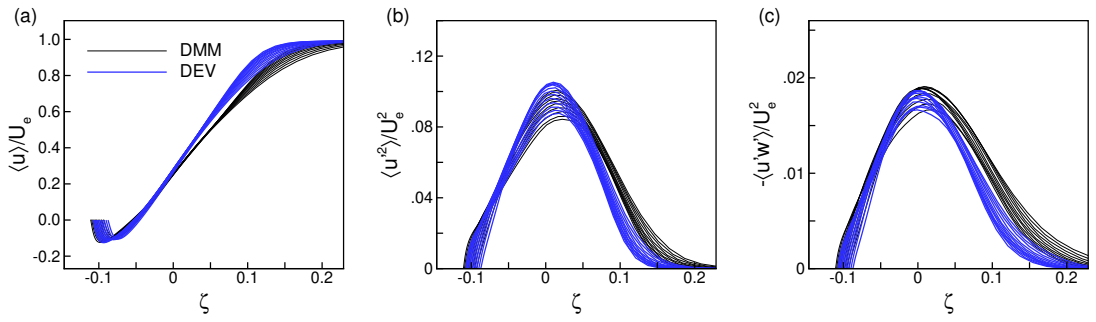

Figure 3.18: Comparison collapse of shear layer profiles (a) streamwise velocity, (b) streamwise turbulence intensity, and (c) turbulence shear stress between the DMM and DEV solutions of R33-M7-L.

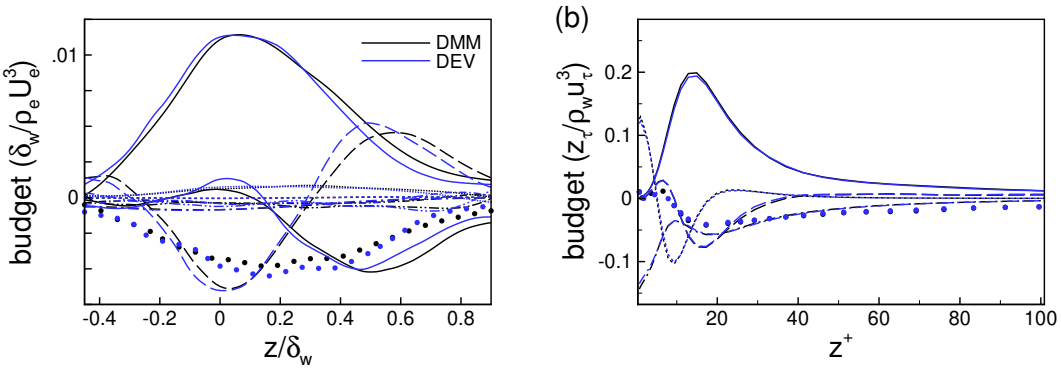

Figure 3.19: Comparison of DMM and DEV solutions of R33-M7-L (a) TKE budgets scaled by the mixing layer thickness δ_w and (b) the upstream boundary layer TKE budgets scaled by z_τ and u_τ. Legend as in Fig. 3.13.

the collapse of (a) the mean streamwise velocity profiles, (b) the streamwise turbulence intensity, and (c) the turbulence shear stress. The streamwise direction now refers to the velocity component in the direction of x_{ml}. The profiles of the DEV solution are visually narrower than the DMM solution indicating that the DEV models produce a lower spreading rate. The DMM solution spreading rate is determined to be $\delta'_w = 0.194$ whereas the DEV solution results in a spreading rate of $\delta'_w = 0.173$; nearly a 10% decrease.

A decrease in the spreading rate of the separation shear layer indicates that the entrainment rate of fluid across the shear layer is reduced in the DEV solution. To balance this slower rate of fluid depletion from the separation bubble, the flow must necessarily

converge to a larger mean separation bubble size compared to the DMM solution. Cross-stream profiles of TKE budget terms (Eqn. A.1) plotted versus ζ and normalized by the local shear layer thickness $\delta_{\mathrm{ml}} = \delta_w x_{\mathrm{ml}}$ are seen to scale by δ_{ml} (Fig. 3.19 (a)). The reduction in spreading rate is therefore a result of a proportional reduction in turbulence activity produced by the DEV model in comparison to the DMM solution. Note that in the upstream boundary layer, the TKE budget profiles scale by z_τ and ρ_w and the two SGS models produce identical solutions (Fig. 3.19 (b)).

3.8 Summary

Two LES datasets of separated hypersonic STBLI flows at experimentally achievable conditions were presented and a thorough documentation of the mean flow statistics was provided. Time- and spanwise-averaged flow fields of Favre-averaged velocity, temperature, and density were given in contour plots and also as individual profiles highlighting the changes in these quantities through the interaction. Averaged streamwise distributions of skin friction, wall pressure, and heat transfer as well as the rms magnitude of each was included. Separation lengths were obtained from the skin friction distribution. We found that for both the Mach 7 and Mach 10 separated interactions, the root-mean-squared pressure fluctuations reached a maximum near reattachment and peaked at approximately half the post-shock mean level. Maximum skin friction and heat transfer fluctuations were also found to occur on the ramp just downstream of separation where the turbulence from the incoming boundary layer are heavily compressed at the impingement location of the separation shock on the ramp surface.

Profiles of mean velocity, turbulence stresses, TKE budgets, as well as the Reynolds stress anisotropy tensor all indicate a mixing layer-like behavior in the shear layer of

the hypersonic separated flows. At the corner, a wide single-inflection-point mean velocity profile was shown to coincide with a broad peak in turbulence activity, turbulence production, and viscous dissipation. Similar observations have been made in separated supersonic STBLI [12, 84] and appears to be a persistent feature in the case of the hypersonic interaction.

Two classic heat transfer scaling relations, the Reynolds Analogy Factor and the QP85 relation of Back & Cuffel [69], were tested on the separated hypersonic LES data. The QP85, which was shown by Priebe & Martin [34] to be reasonably accurate for the attached Mach 7 interaction, breaks down both in the separated region and in the downstream recovering boundary layer. The RAF also fails in the separated region and the downstream boundary layer. If, however, the downstream post-shock conditions were used instead of the upstream condition in the definitions C_f and C_h, the results were much more satisfactory in the downstream boundary layer.

Common assumptions on velocity-temperature fluctuation relations such as constant Prandtl number and the Strong Reynolds Analogies modified for non-adiabatic wall conditions were found to be accurate to a large extent in the upstream boundary layers of both flows and in the downstream boundary layer of the Mach 7. Neither the constant Prandtl number nor the SRAs were found to be accurate for the downstream Mach 10 flow. It is much more difficult to evaluate the turbulent Prandtl number and SRAs relations in the separation region. Both the recirculating motion of the flow and the fact that the flow is deflected away from the wall surface make the definition of u'' in Eqns. 3.1 through 3.4 ambiguous. A more sophisticated analysis would be required to extract useful information on the temperature-velocity fluctuation properties in the separated region.

A comparison was made of the LES DMM and DEV solutions of the separated

Mach 3 STBLI and attached Mach 7 interactions from Chapter 2 and the fully separated Mach 7 STBLI from the present chapter. It was found that the effect of excluding the scale-similar term was minor in the supersonic interaction solution and in the attached hypersonic solution. The DEV solution of the separated Mach 7 interaction resulted in a significant increase of 30% in the separation length. It was concluded that the reason for this difference is not a result of any change in the incoming boundary layer solution but in the solution of the separation shear layer. It will be shown in Chapter 6 that the shear layer in this case is highly compressible with a convective Mach number of 2. The convective Mach number of the Mach 3 flow in comparison is 1. Spreading rate and TKE budgets revealed that the DEV model underestimates the turbulence activity in this highly compressible shear layer.

This chapter focused on the mean flow properties, however, the initial evaluation of the spectral content of the separation and reattachment history indicates that the characteristic low-frequency shock unsteadiness is present in both of these hypersonic flows. The documentation of the dynamic properties of the low-frequency cycle in the current data is the topic of a the next chapter.

Chapter 4: Low-Frequency Mode Form in Hypersonic STBLI

4.1 Background

The origin of the low-frequency unsteadiness in separated STBLI flows has been the topic of much research for the past several decades. For many years the research was concerned with identifying an upstream influence. In many cases the unstable motions of the shock were found to correlate with the long momentum fluctuations in the incoming boundary layer [16, 17, 18, 85]. However, several articles have also shown the separation motions correlate with the unsteadiness of the separation bubble and the downstream flow [3, 11, 19, 20, 21]. Priebe & Martin [12] showed that the low-frequency cycle of the Mach 3 compression ramp STBLI flow shows very specific structure changes in the separation bubble depending on the phase of the low-frequency cycle. These changes involved a bifurcation of the shear layer producing a multi-inflection point velocity profile and local increase in turbulence activity indicating an inviscid mechanism. The structural change could also be identified by a change in the skin friction distribution that was found to be similar in form to the unstable global mode identified in the reflected shock simulation of Touber & Sandham [42]. Recent arguments put forward by Martin *et al.* [23] and Martin & Helm [24] point out striking similarities among the inviscid instability identified by Priebe & Martin [12], the surface flow visualizations of the STBLI experiment of Settles *et al.* [67], and the global unstable modes identified in several different cases of laminar

separation [86, 87, 88]. The indication then is that the low-frequency unsteadiness is driven by a self-excited, downstream inviscid instability.

This hypothesis was further corroborated by the recent work of Priebe *et al.* [22]. Priebe *et al.* performed a Dynamic Mode Decomposition (DMD) analysis on the DNS data of a Mach 3 compression ramp flow (the same DNS dataset as R24-M3n-D in Chapter 2.5) and found that the flowfield generated from a reconstruction of the five low-frequency DMD modes took the form of streamwise-oriented, counter-rotating vortices that extend from the point of separation and down the length of the ramp. In addition, the formation of these vortices coincided with an increase in strength of a centrifugal instability vortex metric (Görtler number) in the vicinity of separation and reattachment. As noted by Martin *et al.* [23, 24], revealing the form of the unstable mode as counter rotating vortices could also explain the similarity between the STBLI flow structure and the spanwise repeating cell-like structure of the laminar separation modes. Furthermore, Priebe *et al.* [22] and also Martin *et al.* [23, 24] provided a discussion on the passive sensitivity of this inviscid centrifugal instability to input from the upstream turbulence fluctuations, thus reconciling the correlations of the separation motion with the upstream boundary layer.

It was also demonstrated by Priebe *et al.* [22] that a simple low-pass filtering operation in time applied to the DNS data produces the same flow structure as the reconstructed DMD modes. In Fig. 4.1 are reproduced from Priebe *et al.* [22] and show a snapshot of the reconstructed low-frequency DMD modes from the DNS data compared to the low-pass filtered (wide span) DNS data. In this chapter, we investigate the dynamics and structure of the low-frequency unsteadiness in the LES dataset R33-M7-L from Chapter 3 of the Mach 7 STBLI flow over a 33^o compression ramp. A simple low-pass filtering operation in time applied to the full three-dimensional flow volume is performed. In Section 4.2

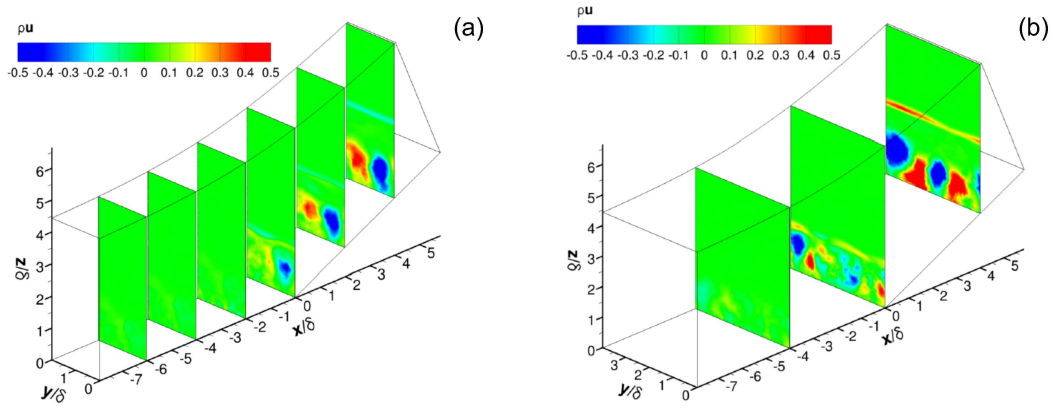

Figure 4.1: Low-frequency mode shape in the Mach 3 STBLI DNS data reproduced from Priebe *et al.* [22]. Streamwis momentum fluctuations in (a) the reconstructed DMD modes and (b) the wide-span low-pass filtered DNS.

we show that the low-frequency mode in the Mach 7 case is also in the form of counter-rotating, streamwise-oriented vortices as identified in the Mach 3 DNS, indicating that the same inviscid centrifugal instability persists in the hypersonic regime. The DMD analysis of Priebe *et al.* [22] was performed on a narrow 2δ-wide computational domain. The increased domain size of the Mach 7 simulation also provides information on the spanwise variation of the low-frequency mode. In addition, time resolved videos of the low-pass filtered flow were generated and provide additional insight into the interpretation of the mechanism by which the inviscid vortical structures drive the separation bubble unsteadiness. A proposed model for the origin of the low-frequency unsteadiness in separated STBLI is discussed in Section 4.3.

4.2 Low-Pass Filtered Data

As was demonstrated in Chapter 2.5 and 3.2, the time signal of separation is a good indicator of the low-frequency unsteadiness in separated STBLI. The pre-multiplied PSD of separation history of the R33-M7-L solution was shown in Chapter 3.2 and broadband

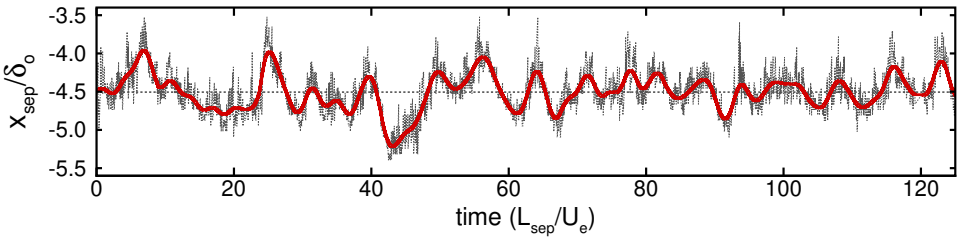

Figure 4.2: Time signal of separation position in the R33-M7-L data. The unfiltered signal is plotted in gray and the low-pass filtered signal in red.

low-frequency energy between nondimensional frequencies of $St_L = fL_{sep}/U_e = 0.2$ and 0.02 were observed. For the purpose of isolating the frequencies associated with the low-frequency shock motions, a cutoff frequency of $St_L = 0.3$ is selected for the low-pass filter. The resulting filter is demonstrated in Fig. 4.2 by a comparison of the unfiltered separation signal plotted in gray and overlaid by the low-pass filtered signal in red.

The time filtering operation requires a high sample rate output of the full 3D volume data at a frequency of $St_L = 0.15$. The width of the filter is 400 samples or $60L_{sep}/U_e$ in time. The flow field is filtered at each sample volume of the data in order to produce time resolved videos from which the dynamics of the low-frequency mode could be studied. Four uncorrelated snapshots in time selected from one of the videos are plotted in Fig. 4.3 showing instances of the filtered flow visualized by contours of streamwise momentum fluctuations. In each figure appear spanwise-alternating positive and negative 'spots' in the downstream flow on the ramp. A comparison of the four snapshots in time shows that these filtered structures are not fixed in space but are unsteady and move about in the spanwise direction. They also vary in strength both along the span and in time. These figures are comparable to the Mach 3 mode shown in Fig. 4.1.

The same structures are visualized again in Fig. 4.4 where the streamwise momentum fluctuations are shown as volume plots that highlight the locations of the cores of the red

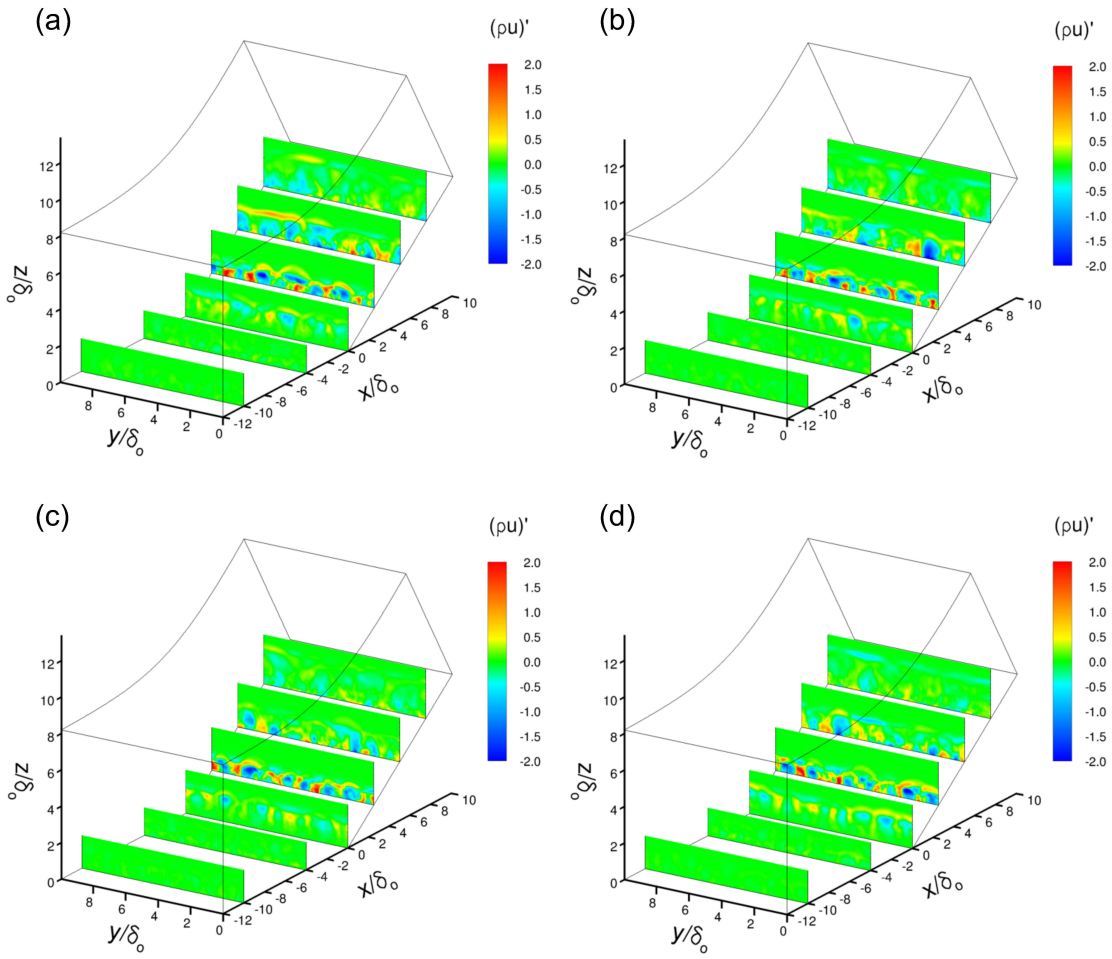

Figure 4.3: Uncorrelated instantaneous snapshots of the low-pass filtered momentum fluctuation field in the Mach 7 STBLI visualized by contour plots.

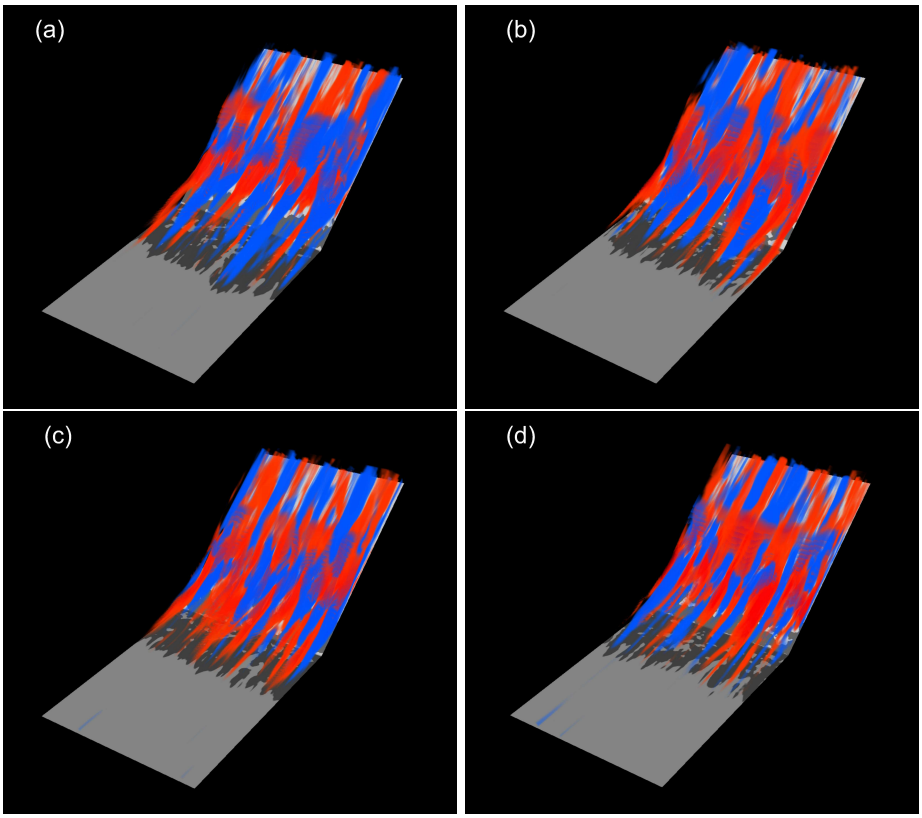

Figure 4.4: Uncorrelated instantaneous snapshots of the low-pass filtered momentum fluctuation field in the Mach 7 STBLI visualized by volume plots. Images are taken from the same time instances as in Fig. 4.3

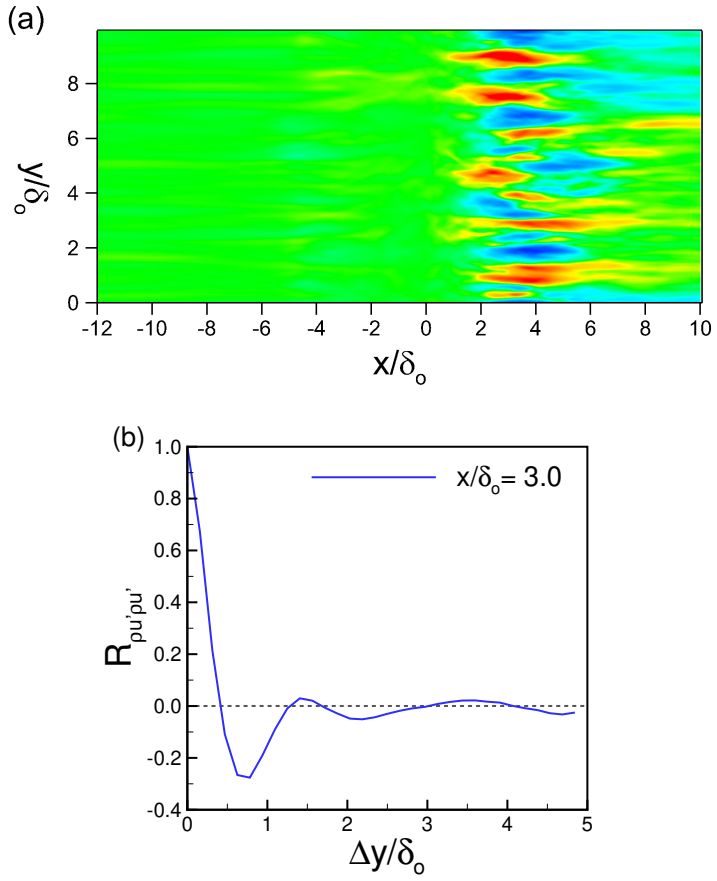

Figure 4.5: Spanwise periodicity in the low-pass filtered momentum fluctuation field is seen in the streamwise-spanwise plane located 0.15δ above the wall surface (a). The ensemble averaged cross-correlation of spanwise momentum fluctuations on this plane and at streamwise location $x/\delta_o = 3$ is shown in (b).

and blue spots in Fig. 4.3. Here the streamwise elongated form in the flow is recognizable as the same structure that was identified by Priebe *et al.* [22]. The shaded portion on the wall surface indicates the area of reverse flow on the wall for which $C_f < 0$. From these figures it is also apparent that the streamwise structures originate near the separation line as was also the case in the Mach 3 DNS data [22]. The images in Fig. 4.4 were also selected from a time resolved video of the filtered flow.

The average spanwise periodicity in the downstream flow is shown in the time averaged contour plot of momentum fluctuation on a plane parallel to the wall surface but offset

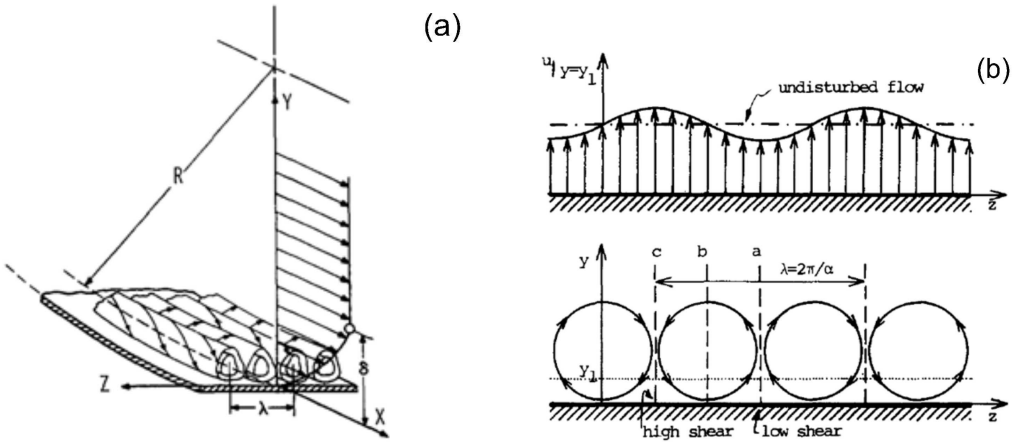

Figure 4.6: Schematic of Görtler vortices reproduced from Floryan. [89]

by a distance of $0.15\delta_o$ (Fig. 4.5). The ensemble averaged auto-correlation of the spanwise momentum fluctuations was calculated on this plane along the position of $x/\delta_o = 3$. The result is the correlation signature plotted in Fig. 4.5 (b) showing a periodic length scale of approximately two boundary layer thicknesses which is consistent with the spanwise length scale reported by Priebe *et al.* [22].

The structures seen in Figs. 4.3-4.5 can be explained in the context of the classic Görtler instability that occurs in laminar boundary layers over walls with concave curvature. The change in streamwise fluid direction introduces centrifugal forces that produce streamwise-oriented, counter-rotating vortices as depicted in the sketch of Fig. 4.6 (a). Because of the proximity to the wall surface, the vortices induce sinusoidal fluctuations in momentum along the cross-stream direction as is shown in the schematic in Fig. 4.6 (b). (Figure 4.6 is reproduced from [89]) If we plot the instantaneous low-pass filtered velocity vector field on a spanwise-wall normal plane positioned on the surface of the Mach 7 compression ramp as indicated in Fig. 4.7, a clear counter-rotating fluid motion is observed as shown in the inset of Fig. 4.7. In this particular snapshot, two pairs of vortices can be seen. Plotting the distribution of streamwise momentum along the bottom edge of these

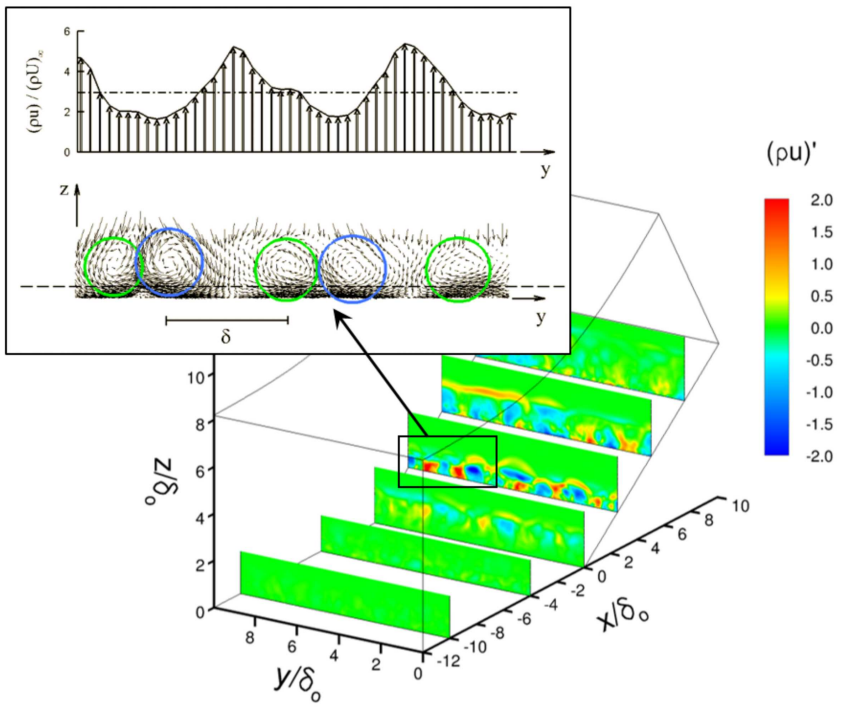

Figure 4.7: Vector field showing vortex rotation in the low-pass filtered Mach 7 STBLI.

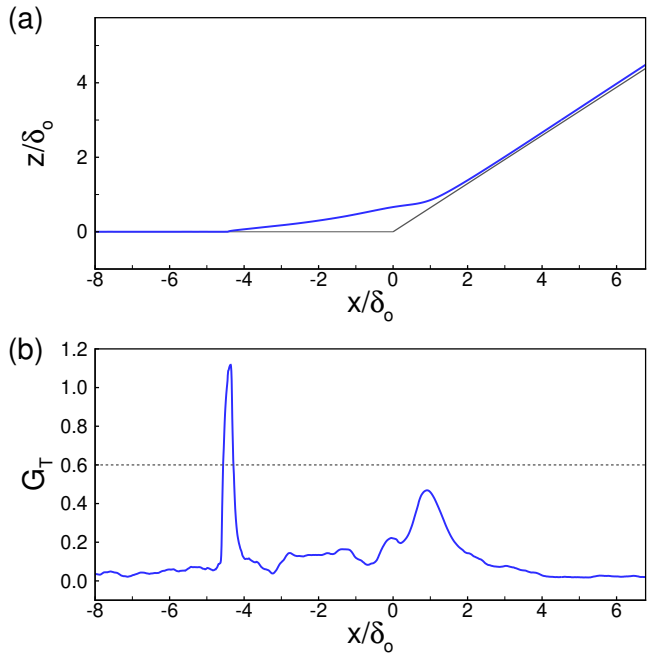

Figure 4.8: Time averaged dividing streamline (a) and the corresponding Görtler number (b) in the Mach 7 STBLI mean flow.

vortices shows that the spanwise variation is consistent with the rotation of the fluid. It is clear then, that the long streaking structures of high and low momentum fluctuations observed in Figs. 4.3-4.5 are a result of streamwise oriented vortices in the low-pass filtered flow.

Further evidence that these structures result from a centrifugal instability is provided by the calculation of the Görtler number. The Görtler number G_{T} defined in Eqn. 4.1 as

$$G_{\mathrm{T}} = \frac{(\theta/\delta)^{\frac{3}{2}}}{0.018(\delta^*/\delta)}\sqrt{\frac{\delta}{R}} \tag{4.1}$$

and is a function of the incoming boundary layer thickness δ, momentum thickness θ, displacement thickness δ^*, and the local radius of streamline curvature R [1, 41]. The dividing streamline in the unfiltered time and spanwise-averaged velocity field of the Mach 7 flow is shown in Fig. 4.8 (a). The G_{T} calculated along this streamline is plotted in

Fig. 4.8 (b). In laminar boundary layers, the critical value of G_T is 0.6 [41]. Although the threshold for turbulent boundary layers is not known, the value of the Görtler number at separation in Fig. 4.8 (b) is nearly twice the laminar threshold. The large value of G_T is also consistent with the formation of the vorticese at separation as was noted in Fig. 4.4.

4.3 Discussion

The physical mechanism involved in fully separated STBLI data and the associated low-frequency unsteadiness has been a point for debate for several decades. Recent work by Priebe & Martin [12] and Priebe *et al.* [22] has shown compelling evidence that the low-frequency unsteadiness of separated STBLI's is in fact driven by the dynamics of inviscid vortical structures (IVS) that are aligned with the streamwise direction and mix the inviscid high momentum fluid with the near wall separated flow. Conceptually similar to the inviscid Görtler vortices occurring in laminar boundary layers over concave surfaces, the IVS might originate from the elevated streamline curvature at the separation point and extend downstream with the vortex cores oriented in the streamwise direction. Alternatively, a second theory regarding the origin of the IVS has been formulated that these large vortical structures are a product of the 3D structure of the separated flow [25]. In whichever case that might explain the origin of the vortical structures, the effect the IVS have on the separated flow is the same.

As is discussed by Martin *et al.* [23] and Martin & Helm [24], it is the mixing produced by these vortices between the freestream and the separated fluid that produces the low-frequency unsteadiness in the separated STBLI. Based on the observations in the literature described above, as well as the new visualizations presented for the Mach 7 hypersonic wide-span data, a physical model for the low frequency is proposed (see also

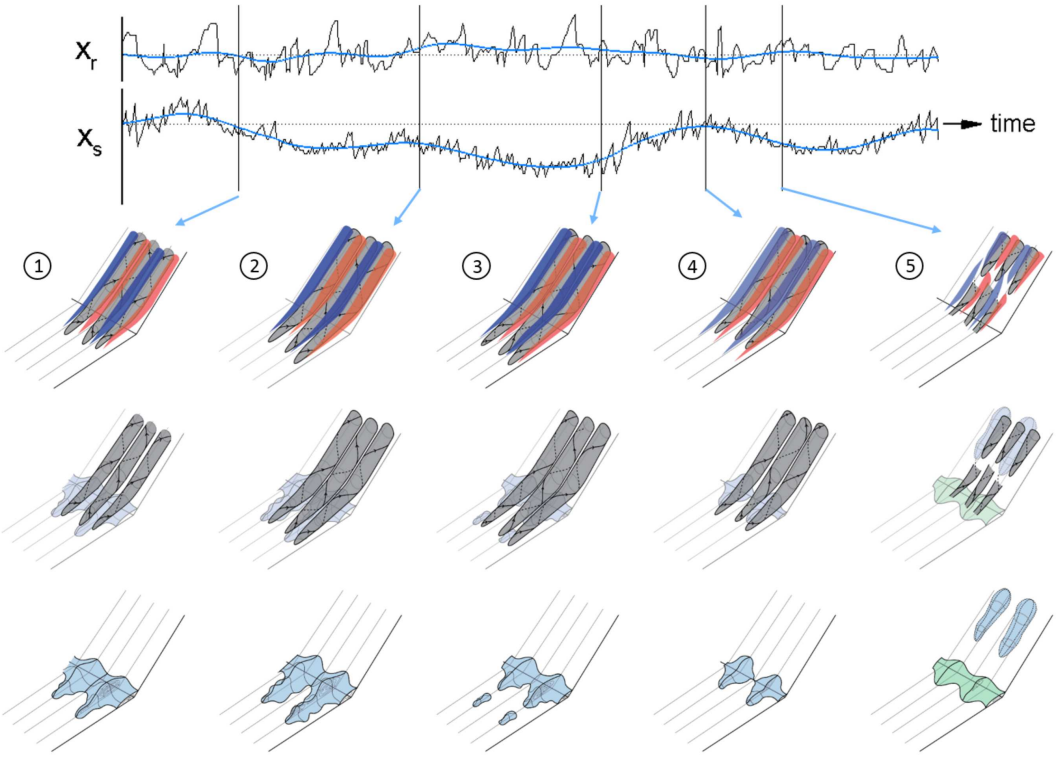

Figure 4.9: Schematic of the low-frequency instability dynamics.

the discussion in Martin *et al.* [24]). Figure 4.9 shows a schematic of the time progression of the state of the separation region in the compression ramp interaction. At the top of Fig. 4.9 are sample time segments of separation and reattachment history. Below this are three rows of images depicting different details in the separated flow. Images in the same column represent the flow structure at the same instant in time. The top row shows the streamwise counter-rotation vortices drawn as the gray structures, and the momentum fluctuations induced by the direction of rotation of the vortices are colored in as red and blue streaks for positive and negative momentum fluctuations respectively. In the second row of images, the momentum fluctuation colors are removed and the area of recirculating flow is indicated by the shaded bubble drawn beneath the vortices. In the last row, the vortices are removed to show the time progression of the separation bubble only.

The mechanism of the unsteadiness is proposed to be the following. From left to right beginning with station 1, the separation bubble is at medium size and the separation signal indicates the bubble is growing at this instant. The presence of the separation bubble produces curvature in the streamline at separation which causes the formation of the IVS. At station 2, the bubble continues to grow and as a result, the curvature at separation increases causing the IVS in turn to become stronger. At Station 3, the bubble has reached its maximum size and the vortices their maximum strength leading to the condition at station 4. The strength of the vortices has grown to the point where the mixing of the flow from the freestream to the wall and the wall to the freestream is such that the fluid in the separation bubble is depleted and ejected into the downstream flow and the separation bubble collapses. Because the bubble has been depleted of fluid, the streamline curvature at separation is flattened and the vortex strength is significantly reduced. At station 5, after the fluid in the bubble is ejected, the natural state of the flow is to again separate, producing a new region of reverse flow and new vortices to form, starting the same cycle over again.

Chapter 5: The Scaling of Hypersonic STBLI

§The majority of this chapter is reproduced from Helm & Martin [90].

5.1 Chapter Overview

Souverein, Bakker, and Dupont [14] (SBD hereafter) introduced a scaling for the separation length in two-dimensional, supersonic shock-separated flows. The scaling is based on mass conservation arguments and depends only on the freestream Mach number, upstream boundary layer displacement thickness, and flow deflection angle. The interaction strength metric is an expression that approximates the ratio of pressure jump across the shock structure to the pressure jump required for the onset of separation and is a function of inviscid pressure ratio and freestream Mach number. To test their scaling method, SBD compiled from the literature a large database of STBLI that included experimental and computational data of both reflected shock and compression ramp interactions at various states of separation and Reynolds numbers. The database consisted of interactions with freestream Mach numbers ranging from 1.7 to 5. One of the key features of the SBD scaling is the collapse of both compression ramp and reflected shock data to the same curve.

The data compilation of SBD included predominantly adiabatic shock interactions. Jaunet, Debieve, and Dupont [15] (JDD hereafter) showed that the SBD scaling method does not account for variations in separation length caused by wall heat transfer. The

authors derived an alternate nondimensionalized shock strength metric based on the free interaction theory of Chapman *et al.* [91]. Using their data of a Mach 2.3 reflected shock configuration with both adiabatic and heated walls, and also the adiabatic and cold wall Mach 3 compression ramp data of Spaid and Frishett [92], JDD demonstrated the effectiveness of their new scaling for collapsing the separation data of STBLI with different heat transfer conditions. Their results were further corroborated by the reflected shock DNS at Mach 2.3, of Volpiani *et al.* [93]. JDD, however, were unable to demonstrate their scaling for any STBLI with Mach number above 3 or for any appreciable range of Reynolds number.

In this chapter, we relate the results of JDD to the original scaling of SBD and derive a more general separation-length-to-shock-strength scaling that includes heat transfer effects across all Reynolds numbers and freestream Mach numbers. It is then our task to evaluate the viability and quality of the proposed scaling law. In doing so, we extend any such STBLI separation scaling law into the hypersonic regime for the first time by including our new database of Mach 7 and Mach 10 compression ramp data. This chapter is organized as follows. In Section 5.2.1, we use a control volume analysis of an axisymmetric cylinder-flare configuration to demonstrate that this geometry scales by the same relation as the two-dimensional interactions. In Section 5.2.2, we present a modification of the interaction strength metric that accounts for wall heat transfer effects. In Section 5.3, we introduce our database of hypersonic compression ramp STBLI. The scaling modification of Section 5.2.2 and the 3D scaling of Section 5.2.1 are then evaluated for hypersonic conditions. The Mach 10 experimental compression ramp data of Elfstrom [27], the Mach 10 cylinder-flare experimental data of Coleman [94], the recent Mach 10 cylinder-flare data of Brooks *et al.* [95], and the recent DNS database of Mach 5 reflected shock STBLI

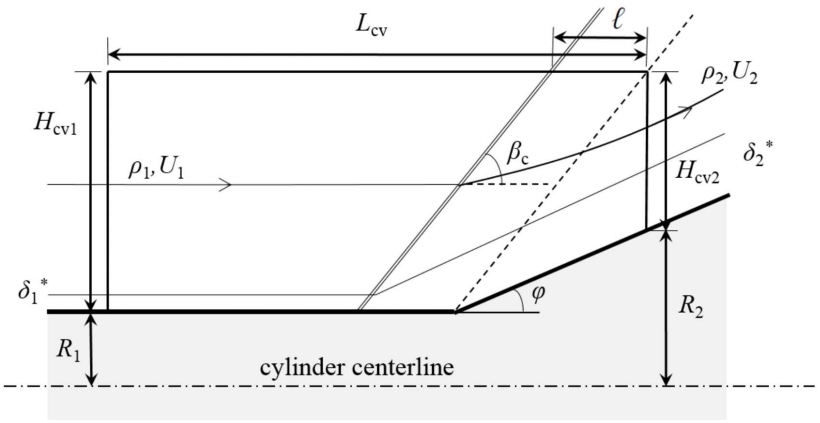

Figure 5.1: Control volume for the cylinder-flare configuration. The notation of Souverein *et al.* is adopted here. (See Figure 5 in [14]).

of Volpiani *et al.* [36] are also included in the evaluation. A discussion of the results is provided in Section 5.4.

5.2 Scaling Method Generalization

5.2.1 Axisymmetric Geometry

The expression for the nondimensionalized separation length L^* as derived by SBD is

$$L^* \equiv \left(\frac{\dot{m}^*_{\text{post}}}{\dot{m}^*_{\text{pre}}} - 1 \right) = \frac{L}{\delta^*} G_3(M_e, \phi). \tag{5.1}$$

Here L^* is by definition the "mass deficit ratio," the term inside the brackets of Eqn. 5.1, which includes the ratio of the outgoing boundary layer deficit of mass flux $\dot{m}^*_{\text{post}} = \rho U \delta^*_{\text{post}}$ to the incoming boundary layer deficit of mass flux $\dot{m}^*_{\text{pre}} = \rho U \delta^*_{\text{pre}}$ as determined by a control volume analysis of the interaction region. For the compression ramp configuration, SBD define the dimensional separation length L as the distance between the mean separation shock foot and the corner. For the reflected shock configuration, L is the distance

between the points of intersection at the wall of the mean impinging shock and the mean reflected shock. The function G_3 is a scaling factor based on the flow deflection angle ϕ and the inviscid shock angle β. Although G_3 is theoretically dependent on the interaction geometry, SBD arrived at the same expression for both the compression ramp and the reflected shock two-dimensional flow configurations:

$$G_3(M_e, \phi) = \frac{\sin(\beta)\sin(\phi)}{\sin(\beta - \phi)}. \tag{5.2}$$

We now derive the separation length scaling for an axisymmetric cylinder-flare STBLI geometry. The control volume for the cylinder-flare in Fig. 5.1 is similar to that used by SBD for the two-dimensional compression ramp case, however for this case we introduce the cylinder radii at the control volume inlet and outlet. We have adopted the same notation for the control volume as SBD to facilitate the comparison of the current analysis with their original formulation. The control volume is also assumed to sweep the full 360^o around the centerline axis. For this derivation we assume that any three-dimensional relief effects along the flare are such that the variation in the wall-normal flow profiles (e.g. U_2, ρ_2, etc.) are minimal and can be approximated by a uniform flow. For example, in the computational solutions by Sims [96] of an inviscid conical shock with cone angle of 30^o and freestream Mach number of 10, the variation in the post-shock similarity profiles was less than 0.5% for wall-parallel velocity and less than 5% for density. In Fig. 5.1, the cylinder-flare shock angle is indicated by β_c to distinguish it from the two-dimensional oblique shock solution angle β occurring at the same freestream Mach number and flow deflection angle.

If the inviscid flow around the flare is considered, conservation of mass over the

control volume in Fig. 5.1 results in the relation

$$\rho_1 U_1 \Big[\big(H_{\text{cv1}} + R_1\big)^2 - R_1^2 \Big] - \frac{\rho_2 U_2}{\cos(\phi)} \Big[\big(H_{\text{cv2}} + R_2\big)^2 - R_2^2 \Big] = 0. \tag{5.3}$$

For the viscous flow with the turbulent boundary layer displacement thickness δ^* and the shock offset distance ℓ, conservation of mass for the same control volume gives

$$\rho_1 U_1 \Big[\big(H_{\text{cv1}} + R_1\big)^2 - \big(R_1 + \delta_1^*\big)^2 \Big] - \frac{\rho_2 U_2}{\cos(\phi)} \Big[\big(H_{\text{cv2}} + R_2\big)^2 - \Big(R_2 + \frac{\delta_2^*}{\cos(\phi)}\Big)^2 \Big] - 2\ell\rho_2 U_2 \sin(\phi)\big(R_2 + H_{\text{cv2}}\big) = 0. \tag{5.4}$$

Subtracting Eqn. 5.3 from 5.4 gives

$$\rho_1 U_1 \Big[\big(R_1+\delta_1^*\big)^2 - R_1^2 \Big] - \frac{\rho_2 U_2}{\cos(\phi)} \Big[\Big(R_2+\frac{\delta_2^*}{\cos(\phi)}\Big)^2 - R_2^2 \Big] - 2\ell\rho_2 U_2 \sin(\phi)\big(R_2+H_{\text{cv2}}\big) = 0 \tag{5.5}$$

which can be rearranged to solve for ℓ as

$$\ell = \frac{\frac{\rho_2 U_2}{\cos^2(\phi)} \Big[2R_2\delta_2^* + \frac{\delta_2^{*2}}{\cos(\phi)} \Big] - \rho_1 U_1 \Big[2R_1\delta_1^* + \delta_1^{*2} \Big]}{2\rho_2 U_2 \sin(\phi)\big(R_2 + H_{\text{cv2}}\big)}. \tag{5.6}$$

To simplify Eqn. 5.6 it is assumed that the control volume is such that $\delta_1^* \ll R_1$ and $\delta_2^* \ll R_2$ resulting in the expression

$$\frac{\ell}{\delta_1^*} = \left[\frac{\delta_2^*}{\delta_1^*} \left(\frac{R_2}{\cos^2(\phi)} \right) - \frac{\rho_1 U_1}{\rho_2 U_2} \big(R_1\big) \right] \frac{1}{\sin(\phi)\big(R_2 + H_{\text{cv2}}\big)}. \tag{5.7}$$

Finally, by using the continuity relation across the shock such that $U_1\rho_1\sin(\beta_{\text{c}}) = U_2\rho_2\sin(\beta_{\text{c}}-$

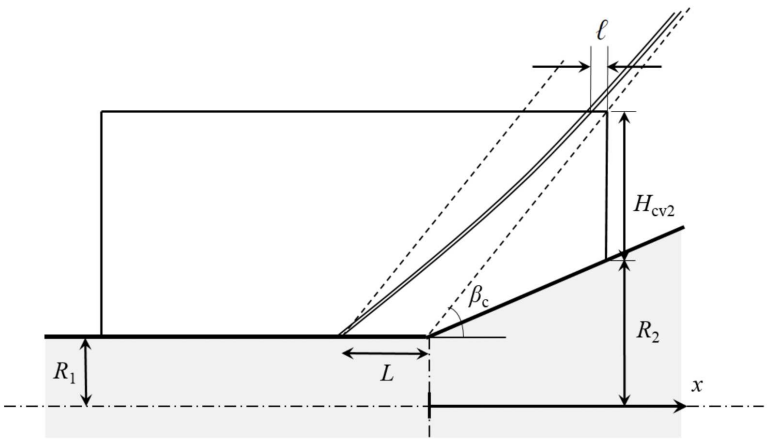

Figure 5.2: Diagram of the cylinder-flare shock position showing the difference between ℓ defined for the control volume and the actual flow separation length L.

ϕ) Eqn. 5.7 can be rewritten as

$$\frac{\ell}{\delta_1^*} = \left[\frac{\rho_2 \frac{U_2}{\cos(\phi)} \frac{\delta_2^*}{\cos(\phi)}}{\rho_1 U_1 \delta_1^*}\left(\frac{2\pi R_2}{2\pi R_1}\right) - 1\right] \frac{\sin(\beta_c - \phi)}{\sin(\beta_c)\sin(\phi)} \frac{R_1}{R_2 + H_{cv2}}. \tag{5.8}$$

By comparing Eqn. 5.8 with Eqn. 5.1, the term in the square brackets is easily recognized as the mass deficit ratio ($\dot{m}^*_{post}/\dot{m}^*_{pre} - 1$) for the cylinder cross-section. The inverse of the two-dimensional flow deflection function G_3 also appears in Eqn. 5.8 and is multiplied by the ratio $R_1/(R_2+H_{cv2})$. Since H_{cv2} and R_2 do not cancel out in the derivation of Eqn. 5.8, it appears that the separation length is dependent on the choice of control volume. This does not make sense physically seeing as a given STBLI flow will have a specific mean separation length L regardless of the choice of control volume. This apparent problem in the derivation can be remedied with the following reasoning. In Fig. 5.1, l is defined as the distance between the crossing point of the shock at the top boundary and the top right corner of the control volume. It is assumed that the shock remains parallel to the inviscid shock inside the control volume thus making ℓ equivalent to the actual separation length

L. This is approximately true for the two-dimensional ramp but not for the cylinder-flare. For instance, if the distance $R_2 + H_{cv2}$ is rewritten in terms of R_1, β_c, and a coordinate variable x defined as the distance along the cylinder centerline from the flare corner (see Fig. 5.2), Eqn. 5.8 becomes

$$\frac{\ell}{\delta_1^*} = \left(\frac{\dot{m}^*_{post}}{\dot{m}^*_{pre}} - 1 \right) {G_3}^{-1} \frac{R_1}{R_1 + x\tan(\beta_c)}. \tag{5.9}$$

In this form one can clearly see that the length ℓ goes to 0 as x increases indefinitely. It would appear then that the actual separation length L is determined from the limit of Eqn. 5.9 as x goes to 0 which ultimately results in Eqn. 5.1. By this analysis, the cylinder-flare configuration scales by the same relation as the two-dimensional compression ramp. Any three-dimensional effects are therefore entirely contained in the difference in shock angle β_c and downstream-to-upstream pressure ratio generated by the flared geometry as compared to the two-dimensional ramp. Note also from Eqn. 5.8 that, for a given angle ϕ and control volume dimensions, R_2 is equal to R_1 plus a constant. If R_1 goes to infinity, which is the equivalent of a flat plate, the ratio R_2/R_1 goes to 1 which results in the original two-dimensional ramp expression of Eqns. 5.1 and 5.2. This further implies that the shock angle β_c is a function of the cylinder radius R_1 and will in fact vary between the oblique shock angle ($R_1 = \infty$) and the conical shock angle ($R_1 = 0$).

5.2.2 Varying wall heat transfer

It was proposed by SBD that the correct interaction strength metric for the scaling of the nondimensionalized separation length data is the ratio of pressure jump across the interaction ΔP to the pressure jump required for the onset of separation ΔP_{sep}. Since the criteria for the onset of separation is not typically known for a given STBLI flow, SBD

derived the interaction strength parameter Se^*_{SBD} as an approximation of $\Delta P/\Delta P_{\mathrm{sep}}$. The assumption was made that ΔP_{sep} scales as the dynamic pressure q_{e} so that

$$Se^*_{\mathrm{SBD}} = k\frac{\Delta P}{q_{\mathrm{e}}}. \tag{5.10}$$

The normalization constant k is introduced to ensure $Se^*_{\mathrm{SBD}} \approx 1$ at the onset of separation and is assumed to be independent of the freestream Mach number. From a compilation of experimental data for which ΔP_{sep} was known, SBD showed that $k = 2.5$ and is also independent of Reynolds number[1] at least up to $Re_\theta = 3 \times 10^5$. Together with L^* from Equation 5.1, Se^*_{SBD} was shown to collapse adiabatic data for M_{e} from 1.7 to 5 and for Re_θ between 2.3×10^3 and 3×10^5. Reflected shock and compression ramp data, both experimental and computational, were included in the database.

More recently, Jaunet *et al.* [15] used reflected shock experiments at $M_{\mathrm{e}} = 2.3$ with varying deflection angle for both an adiabatic and a heated wall ($T_{\mathrm{w}}/T_{\mathrm{r}} = 1.9$ where T_{r} is the adiabatic recovery temperature) to show that the SBD separation strength metric does not collapse data of STBLI's with varying wall temperature conditions. Based on the separation plateau pressure scaling in the free-interaction theory of Chapman *et al.* [91], JDD proposed a new shock strength metric defined as

$$Se^*_{\mathrm{JDD}} = \frac{\Delta P}{k_2 q_{\mathrm{e}} \sqrt{\frac{2C_{f\mathrm{o}}}{(M_{\mathrm{e}}^2-1)^{1/2}}}}. \tag{5.11}$$

The denominator of Equation 5.11 is the approximation of ΔP_{sep} which is now assumed to scale with the incoming boundary layer skin friction coefficient $C_{f\mathrm{o}}$, M_{e}, and q_{e}. The

[1] SBD originally reported a mild dependence on Reynolds number so that $k = 3$ for $Re_\theta \leq 1 \times 10^4$. It was later determined that this shift in k was a result of three-dimensional effects in the experimental data. After correction, k was found to be 2.5 also for the lower Reynolds number data. Communication with P. Dupont.

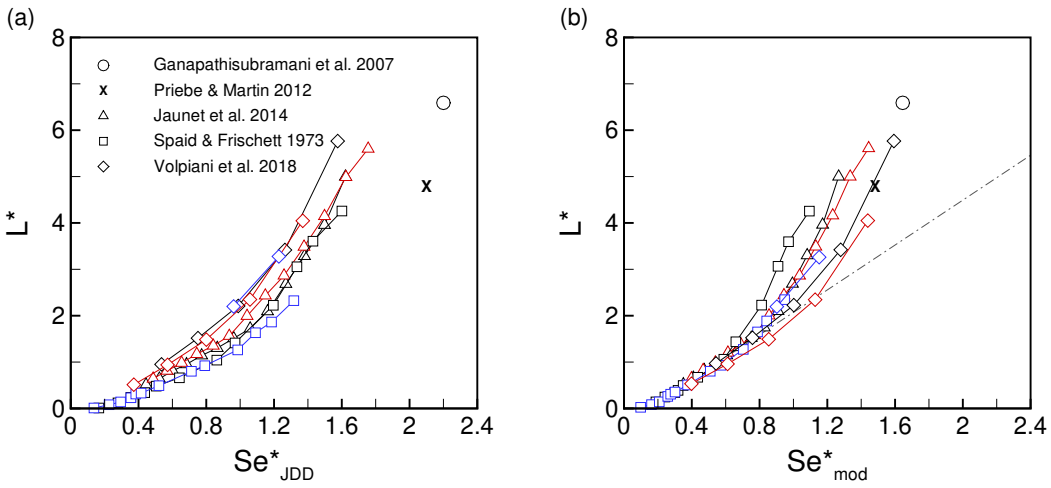

Figure 5.3: Compilation of Mach 2-3 STBLI data with various heat transfer conditions scaled by Se^*_{JDD} (a) and again by the Se^*_{mod} (b). Symbol color indicates the wall temperature condition. Black data points are adiabatic walls, red are heated walls, and blue are cold walls.

constant k_2 is again a normalization constant that is introduced so that $Se^*_{\mathrm{JDD}} \approx 1$ at the onset of separation. JDD determined from the incident shock angle required to separate their adiabatic boundary layer that $k_2 = 7.14$ for their data. The dependence of k_2 with Re_θ or M_e is otherwise unknown.

When Se^*_{JDD} is applied to their reflected shock data together with the adiabatic and cold wall compression ramp data of Spaid & Frishett [92], a much better collapse of L^* is achieved as compared to Se^*_{SBD}. Because the data of Spaid & Friscett is of similar Mach number and Reynolds number, the same k_2 was used throughout. In addition, Volpiani *et al.* [93] also tested the JDD scaling with their DNS database of reflected shock interactions, also at similar freestream conditions, with satisfactory results. Their DNS database included wall temperature ratios $T_\mathrm{w}/T_\mathrm{r} = 1.0$, 0.5, and 1.9. The greatest drawback to the scaling of JDD, however, is the lack of knowledge of the dependence of k_2 on the conditions of any given STBLI flow.

We now propose a new scaling of the interaction strength that is based on the

combined results of JDD and SBD. For the derivation, two observations are made. First, we note that the SBD scaling was shown to work well for a large range of adiabatic STBLI. Second, the parameters Se^*_{SBD} and Se^*_{JDD} have nearly the same form in that Se^*_{JDD} is essentially a correction of the SBD normalization constant k. We make the assumption that both scaling methods are equivalent for adiabatic interactions and that k and k_2 can therefore be related to each other by the following expression.

$$\frac{1}{k} = k_2 \sqrt{\frac{2C_{f\mathrm{o,a}}}{(M_{\mathrm{e}}^2 - 1)^{1/2}}}. \tag{5.12}$$

Here $C_{f\mathrm{o,a}}$ is the skin friction coefficient for an adiabatic boundary layer with the same freestream conditions and Reynolds number. If we assume that k_2 can be determined from the ΔP_{sep} of the adiabatic boundary layer, then we arrive at an expression for a modified proportionality constant k_{mod} that is generalized for any wall temperature condition

$$k_{\mathrm{mod}} = k \sqrt{\frac{C_{f\mathrm{o,a}}}{C_{f\mathrm{o}}}}. \tag{5.13}$$

The k of SBD is therefore simply scaled by the square root of the ratio of the adiabatic $C_{f\mathrm{o,a}}$ to $C_{f\mathrm{o}}$ with heat transfer. The modified separation strength metric then becomes

$$Se^*_{\mathrm{mod}} = k_{\mathrm{mod}} \frac{\Delta P}{q_{\mathrm{e}}} = k \sqrt{\frac{C_{f\mathrm{o,a}}}{C_{f\mathrm{o}}}} \frac{\Delta P}{q_{\mathrm{e}}}. \tag{5.14}$$

Even if unknown, $C_{f\mathrm{o,a}}$ can be estimated using an appropriate skin friction prediction method such as those reviewed by Hopkins & Inouye [97]. It is interesting to mention that if the relation between k and k_2 of Equation 5.12 is used to back out k_2 for the experiments of JDD, a value of 7.41 is obtained compared to their experimentally determined value of

7.14.

We first test the scaling of L^* with Se^*_{mod} on the data of JDD, Spaid & Frishett, and Volpiani *et al.* We also include the DNS compression ramp of Priebe & Martin [12] with $M_\text{e} = 2.9$, ramp angle = 24°, $T_\text{w}/T_\text{r} = 1.0$, and $Re_\theta = 2400$, and the experimental compression ramp of Ganapathisubramani *et al.* [85] with $M_\text{e} = 2$, ramp angle $\phi = 20^\text{o}$, $T_\text{w}/T_\text{r} = 1.0$, a nd $Re_\theta = 35,000$. Figure 5.3(a) shows all L^* data scaled by Se^*_{JDD} as reproduced from figure 10 of Jaunet *et al.* [15] and figure 13b of Volpiani *et al.* [93] Again, the same $k = 7.14$ is used for the Priebe & Martin and Ganapathisubramani data points. The data are then re-scaled using Se^*_{mod} of Equation 5.14 and plotted in Fig. 5.3(b). Two observations are immediately apparent from this comparison. First, a much closer data collapse occurs for $Se^*_{\text{mod}} \lesssim 1$ and the points in this range clearly fall on a linear trend. Second, there is essentially no collapse of the fully separated STBLI data points when scaled by Se^*_{mod}. It will be shown in the next section that similar results occur with the hypersonic data. Further discussion of these observations is provided in Section 5.4.

5.3 Scaling of a Hypersonic Database

For this study, we add to our LES database of hypersonic interactions that was presented in Chapters 2 and 3 by running additional ramp angles for both the Mach 7 and Mach 10 freestream conditions. In addition to runs R8-M7-L and R33-M7-L, five new ramp angles of 17^o, 20^o, 24^o, 28^o, and 31^o are run at Mach 7 using the same M7-L inflow. The same grid domain and resolution as R33-M7-L are used throughout with the only change in the computational grid being the angle of the ramp. For the Mach 10 condition, a new auxilary boundary layer and ramp grid are run with a reduced span width of $L_y = 3\delta_o$ compared to $L_y = 10$ of the R34-M10-L run. Ramp angles of 15^o,

Case	Type	M_e	T_w/T_r	Re_θ	Re_τ	ϕ	Geometry	Reference
M7-L	LES	7.2	0.5	3720	210	$8^o - 33^o$	Ramp	–
M10n-L	LES	9.6	0.3	7940	460	$15^o - 34^o$	Ramp	–
M10-L	LES	9.1	0.3	8280	520	34^o	Ramp	–
M10-Elf1	Exp.	9.22	0.3	9010	680	$15^o - 38^o$	Ramp	[27]
M10-Elf2	Exp.	8.95	0.3	2900	220	$15^o - 38^o$	Ramp	[27]
M10-Col1	Exp.	9.22	0.3	4800	390	$15^o - 40^o$	Flare	[94]
M10-Col2	Exp.	8.95	0.3	2900	240	$15^o - 40^o$	Flare	[94]
M10-CF	Exp.	9.87	0.3	8346	706	34^o	Flare	[95]
M5-Vol1	DNS	5.0	0.8	3760	390	$6^o - 14^o$	Ref. Shock.	[36]
M5-Vol2	DNS	5.0	1.9	3890	175	$6^o - 14^o$	Ref. Shock.	[36]

Table 5.1: Database of hypersonic compression ramp STBLI: flow conditions.

22^o, 24^o, 27^o, 31^o, 33^o, and 34^o are run with the narrow domain. We continue to use the same run casename notation as was introduced in Chapter 2 and here the narrow Mach 10 datasets are reffered to by "M10n". We chose to use the narrow grid to run the vaying ramp angles at the Mach 10 condition simply because of the lower compuational cost. This is especially true for the higher Reynolds number of the Mach 10 boundary layer compared to the Mach 7. As will be discussed in Section 5.4, the narrow grid does tend to restrict the spanwise periodicity in the downstream flow of the separated case, however, the effect that this has on the averaged separation length is small and the same conclusions on the scaling analysis can be made.

A summary of the freestream Mach number and incoming boundary layer Reynolds numbers of the LES database are provided in Table 5.1 together with those from experimental data at similar conditions to the Mach10 LES. The DNS database of Mach 5 reflected shocks at varying angle from Volpiani *et al.* [36] are also included in the compilation. The data of Volpiani *et al.* are unique in this compilation in that they are the only reflected shock data included and also M5-Vol1 is the only heated wall case considered.

A summary of the LES compression ramp compuational grid size and resoltuion are

Case	δ_o (mm)	L_{corner}/δ_o	L_{ramp}/δ_o	L_y/δ_o	L_z/δ_o	Δx^+	Δy^+	${z_2}^+$
M7	5.0	12	12	10	8	26.6-11.3	8.4	0.23
M10n	18.0	13	8	3	7	30.7-10.0	6.7	0.19
M10	18.0	13	12	10	7	27.7-10.5	7.1	0.20

Table 5.2: STBLI compression ramp LES computational grid.

listed in Table 5.2. Details of the Mach 7 and Mach 10 ramp grids from Chapter 3 are repeated here for quick reference. Computational domain sizes are given in terms of the reference boundary layer thickness δ_o. For the compression ramp, the dimension L_{x1} is the distance from the inlet to the corner of the ramp and L_{x2} is the length along the ramp surface measured from the corner to the outlet plane. Grid resolutions are given in units of the inner length scale z_τ as indicated by the '+' superscript.

The mean separation length L in units of δ_o is listed in Table 5.3 for each of the LES runs. Note that for this study, L is defined as the distance from the mean separation point to the corner as is consistent with the definition of separation length used by SBD. The duration over which the mean field was averaged is also listed in Table 5.3 in time units nondimensionalized by both δ_o and L with freestream velocity u_e. The mean skin friction distributions and the mean wall pressure distributions for the Mach 7 interactions are shown in Fig. 5.4. The Mach 10 interactions are shown in Fig. 5.5. Dashed lines indicate attached and incipiently separated ramp angles and solid lines indicate fully separated angles.

We now apply the scaling using Eqns. 5.1 and 5.14 to the data of Table 5.3. The experimental data included in the scaling analysis are the Mach 10 compression ramp data of Elfstrom [27], the Mach 10 cylinder with flare data of Coleman [94] at similar conditions to the compression ramps of Elfstrom, and the AEDC cylinder-flare experiment of Brooks

Case	ϕ	L/δ_o	$\Delta t U_e/\delta_o$	$\Delta t U_e/L$
R8-M7-L	8°	0	150	–
R17-M7-L	17°	0.27	500	1850
R20-M7-L	20°	0.49	610	1240
R24-M7-L	24°	0.87	460	530
R32-M7-L	28°	1.51	540	360
R31-M7-L	31°	2.94	770	260
R33-M7-L	33°	4.42	1970	450
R15-M10n-L	15°	0.06	140	2330
R22-M10n-L	22°	0.27	150	560
R24-M10n-L	24°	0.40	200	500
R27-M10n-L	27°	0.59	190	320
R31-M10n-L	31°	1.10	180	160
R33-M10n-L	33°	2.28	210	90
R34-M10n-L	34°	3.10	220	70
R34-M10-L	34°	3.32	310	90

Table 5.3: Mean flow separation of LES ramp data.

et al. [95]. Not all of the information needed to scale the experimental data was available from the respective references. The displacement thickness for the data of Elfstrom was not reported explicitly. We used the boundary layer velocity profile data available from the Ph.D. thesis of Elfstrom [98] together with the Crocco relation for mean velocity and mean temperature to reproduce the experimental profiles of $(\rho_e U_e)$ from which δ^* could be integrated. Neither the displacement thickness nor the velocity profiles were available for the data of Coleman. Since the data of Coleman and Elfstrom were run in the same experimental facility at the same nominal freestream and wall temperature conditions, we assume here that the ratio δ^*/δ is the same between M10-Col1 and M10-Elf1 and between M10-Col2 and M10-Elf2. The separation lengths L were obtained from the available static pressure distributions (figures 16, 17, and 20 of Elfstrom [98]; and figures 50a and 51a of Coleman [94]). The separation length of the M10-CF was estimated as $L = 0.3\delta$ from the PIV mean streamwise velocity field at the flare corner (figure 12 in Brooks *et al.* [95]). The surface pressure measurements of Coleman showed that the pressure on the flare

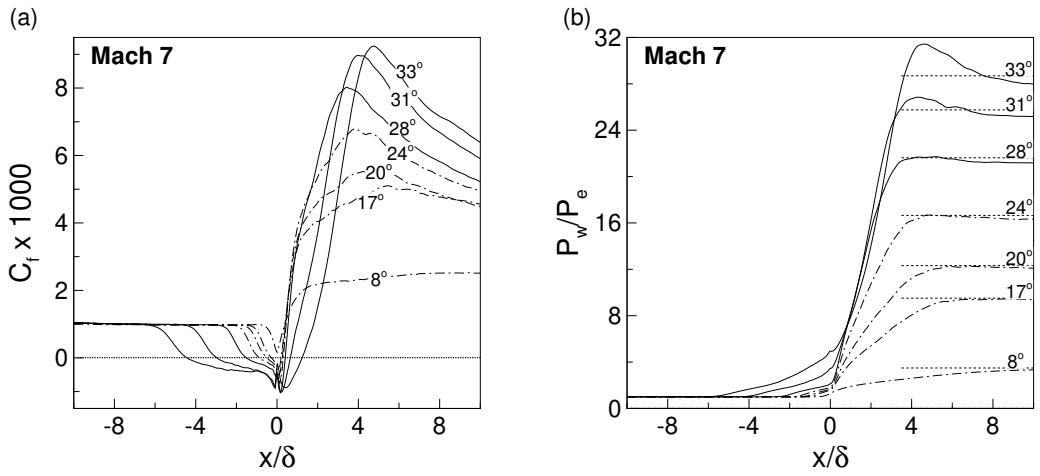

Figure 5.4: Skin friction (a) and wall pressure (b) distributions for M7 LES data. Dashed lines indicate attached and incipient separated ramp angles. Solid lines are fully separated ramp angles.

downstream of reattachment approached the conical shock inviscid pressure for all flare angles. Surface pressure data was not available for the AEDC experiment. Inviscid conical shock theory was used to estimate β_c and P_2/P_1 for all flare data in Table 5.1. The van Driest II theory [99] was used to determine the adiabatic skin friction coefficient $C_{fo,a}$ for the calculation of k_{mod} for all data. Volpiani *et al.* [36] reported L^* versus Se^*_{SBD}. The Se^*_{mod} data were scaled by $\sqrt{C_{fo,a}/C_{fo}}$ where the C_f conditions were determined also from van Driest II theory. The van Driest II theory was shown by Duan, Beekman, and Martin [73, 74] to be accurate within 5% error for Mach numbers up to 12 and wall temperatures T_w/T_r from 1.0 to 0.2. They did not test the skin friction prediction on heated walls.

The scaling results are plotted in Fig. 5.6. The incipiently separated interactions, including the cylinder-flare data, appear to be well described by the same linear trend observed in the supersonic data. As with the supersonic data, significant spreading occurs in the fully separated regime and the scaling law does not hold. The M10n, M10,

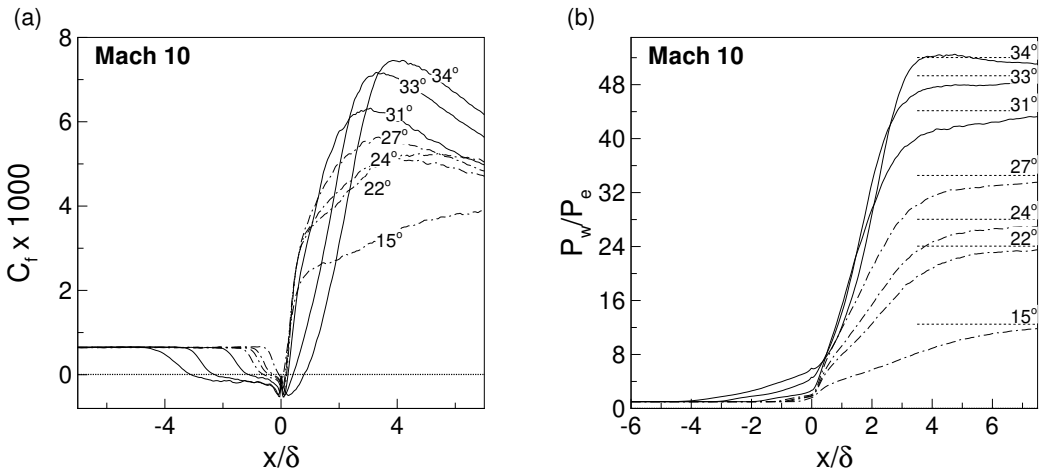

Figure 5.5: Skin friction (a) and wall pressure (b) distributions for M10 LES data. Dashed lines indicate attached and incipient separated ramp angles. Solid lines are fully separated ramp angles.

and M10-Elf1 data are of similar conditions (Re_θ, M_e, T_w/T_r) and these nearly coincide across all ramp angles. The fully separated R31-M10n-L, R33-M10n-L, and R34-M10n-L are a bit below the M10-Elf1 and R34-M10-L data points, however, this is interpreted as a consequence of the narrow computational domain of M10n as will be discussed in the following section. The fully separated cylinder with flare M10-Col1, also at similar conditions as M10-Elf1 but with half the Re_θ, has dramatically larger L^* than the compression ramp.

5.4 Discussion and Summary

All Se^*_{mod} and L^* data from Sections III and IV are plotted together in Fig. 5.7(a). Both the supersonic and hypersonic data show that there are two distinct linear regions in the curve of L^* versus Se^* when multiple deflection angles are plotted for the same incoming boundary layer. The point at which the two linear regions intersect has been determined to coincide with the onset of separation for a given boundary layer [14, 15]. In

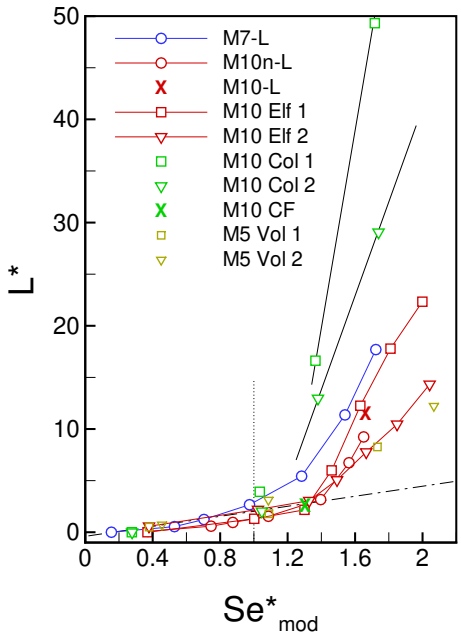

Figure 5.6: Separation scaling data of the hypersonic STBLI database of Table 5.1. The dashed line is the linear trend reproduced from Fig. 5.3 (b).

corroboration with this assumption, careful observation of the current LES data reveals that the first point on the fully separated branch of each of the M7 and M10n curves (R28-M7-L and M10-31 respectively) is also the smallest ramp angle simulated for which the spanwise averaged flow field does not instantaneously reattach. A characteristic of these two slopes, which is most apparent in the hypersonic data but is also true for the supersonic data, is that they are not proportional to each other in the same ratio across all data. It is therefore not possible to collapse both the incipiently separated data and the fully separated data simultaneously by using a single proportionality constant such as k in the definition of the shock strength metric. We also point out that this problem of the disproportionality of the slopes remains even if L^* is plotted versus $\Delta P/\Delta P_{\text{sep}}$ as is done in Fig. 5.7(b) for all data for which ΔP_{sep} is known. Recall that Se^*_{mod} is an approximation of the ratio $\Delta P/\Delta P_{\text{sep}}$ such that $q_e/k_{\text{mod}} \approx \Delta P_{\text{sep}}$. In conclusion, it seems that the

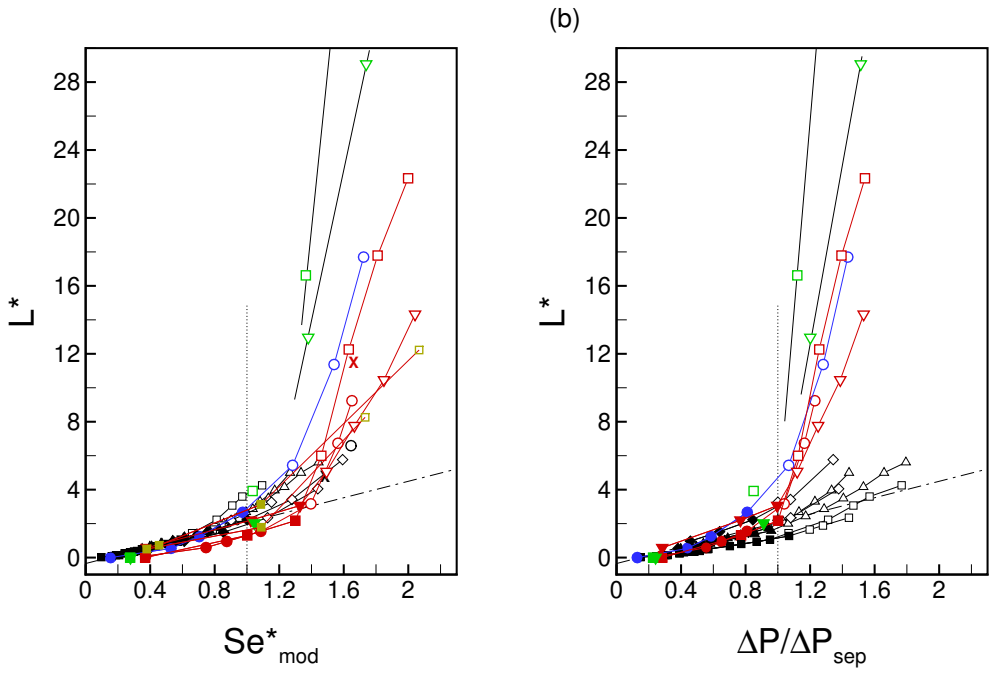

Figure 5.7: Supersonic and hypersonic scaled STBLI data plotted together with L^* versus $Se^*_{\rm mod}$ (a) compared to L^* versus $\Delta P/\Delta P_{\rm sep}$ (b). Symbols are as in Fig. 5.3 for supersonic data and Fig. 5.6 for hypersonic data. Filled symbols are incipiently separated and open symbols are fully separated.

two branches of incipiently separated and fully separated STBLI are each governed by different physical mechanisms and therefore different scaling laws, each potentially with its own dependence on Reynolds number, Mach number, wall temperature, and geometry.

In comparing Figs. 5.3(a) and 5.3(b) and also Figures 5.7(a) and 5.7(b) we propose that the modified separation scaling derived in Section III is the appropriate separation-length-to-shock-strength scaling for the incipient separation regime. For the incipient interactions, the boundary layer separates when the pressure jump across the shock structure is sufficient to halt the momentum of the incoming boundary layer and so ΔP scales by $q_{\rm e}$. Increasing the wall temperature will increasingly skew the distribution of momentum towards the edge of the boundary layer and so we see that heated interactions produce larger separation than an adiabatic case at the same deflection angle. The opposite effect

occurs when the wall is cooled. The skin friction ratio correction on k_{mod} was shown in Section III to account for the variation in separation length caused by the wall temperature condition. Also by the current data compilation, the incipient separation data collapse appears to be independent of the geometry and agrees for all compression ramp, reflected shock, and axi-symmetric flare data. In contrast, the separated interactions follow a different trend and a different Reynolds number dependence.

With the current limited data compilation and the limited knowledge of the factors affecting the dynamics of the IVS, it is not possible to propose a scaling for the fully separated STBLI regime. We observe, however, that the data trends can be reconciled with the existence of the IVS discussed in Chapter 4. Shown by the data in Fig. 5.6, there is an obvious dependence of L^* on Reynolds number when comparing between M10-Elf1 and M10-Elf2 and also between M10-Col1 and M10-Col2. The L^* is significantly reduced in the lower Reynolds number data. Notice that an increase in the Reynolds number of the incoming boundary layer results in an increase in the turbulent mixing and energy in the incoming boundary layer flow, which in turn hinder the development of the IVS resulting in weaker circulation of the vortices rendering them less effective in depleting the separation bubble. This is consistent with the fact that the mean separation length increases with increasing Reynolds number for a given M_e and ϕ as the data of Elfstrom and Coleman show. In the case of M10-34, the IVS are confined by the narrow grid resulting in a stronger instability with stronger circulation. The result is again a smaller separation length in M10-34 compared to M10-34w for which there is no such constriction. For the cylinder-flare data compared to the compression ramp data (M10-Elf to M10-Col data points) the spanwise relief effects from the increasing flare radius downstream of attachment significantly weakens the strength of the IVS and the separation length

increases dramatically.

Chapter 6: Characterization of the Shear Layer in Separated STBLI

§The majority of this chapter is reproduced from Helm *et al.* [83].

6.1 Background

The free shear layer is one of the most fundamental shear flows for the study of turbulence. Unlike wall-bounded shear layers, the mixing layer develops with only one length scale. The canonical mixing layer therefore affords a simple yet essential configuration for the study of compressible turbulence. A firm grasp of the fundamental physics of compressible turbulence in shear flow is of paramount importance for the advancement of hypersonic flight technology, supersonic combustion, and the development of robust practical simulation tools for such engineering design efforts.

Despite its conceptual simplicity, the compressible mixing layer exhibits certain properties that are difficult to explain physically. One of its most documented features is a significant decrease in spreading rate with increasing compressibility. This property is noted in research articles as early as the 1950's from experimental observation [100, 101] and from linear stability prediction of the stabilizing effects of increasing Mach number on a vortex sheet [102, 103, 104]. By the 1970's, consensus among scientist resulted in the well-known "Langley curve" [105, 106]. The Langley curve is generally plotted as normalized spreading rate versus the convective Mach number M_c, a metric for compressibility proposed by several authors [107, 108, 109]. Early research also revealed that the reduction

in spreading rate is accompanied by a reduction in fluid entrainment, turbulence mixing, and turbulence stresses [110, 111, 112]. Many significant research contributions advancing our physical understanding of these phenomena have since been put forth as outlined in several review articles [1, 113, 114, 115]. In spite of the large volume of research, precise scaling laws and robust models for simulation are still lacking.

Several factors make identification of exact scaling dependencies difficult. Significant spread exists in the data partly due to limitations of measurement techniques, but also due to an acute sensitivity of the mixing layer to initial and boundary conditions. This sensitivity is problematic in both experiment and computation and can produce large variations in the spreading rate and turbulence stresses. Disturbances in the freestream, conditions of the boundary layer, experimental facility acoustics, splitter plate vibration, and test section confinement can all contribute to scatter in the data [1, 115]. In the classic relation of Papamoschou & Roshko [109] $\delta' = \delta'_{\text{inc}}\phi(M_c)$, determination of the scaling function $\phi(M_c)$ is compromised by significant scatter in both the compressible spreading rate δ' and the incompressible spreading rate δ'_{inc}. Dimotakis [113] reported as much as 30% variation in incompressible spreading rate data due to experimental inconsistencies. Smits & Dussauge [1] estimated as much as 50% variation in the compressible data measurements. A number of attempts have been made to correct for the discrepancies in the data [116, 117, 118, 119] with some success, however, large spread in the data still remains. Similarly for turbulence quantities, scatter has prevented a consensus on the trends caused by increasing compressibility. For example, many studies indicate that the peak normal stress in both the streamwise $\langle u'^2 \rangle$ and cross-stream $\langle w'^2 \rangle$ directions steadily decrease with increasing M_c. This resulted in the turbulence shear stress $\langle u'w' \rangle$ and anisotropy $\langle u'^2 \rangle / \langle w'^2 \rangle$ remaining relatively constant [120, 121, 122, 123]. Still, several other studies

[112, 124, 125] found that for increasing M_c, $\langle u'^2 \rangle$ is constant and only $\langle w'^2 \rangle$ decreases causing the shear stress to decrease and anisotropy to increase. The overall scatter is on the order of the reported trends as can be seen in the data compilations in [1] and also in the more recent data compilations of Barre & Bonnet [126].

The sensitivity of the mixing layer stems from the complex dynamics of the large-scale vortices produced by the Kelvin-Helmholtz instability. These large-scale mixing layer eddies undergo significant changes with increasing Mach number and have been found to play a dominant role in establishing both the spreading rate and turbulence levels. It has been observed in many studies that the structure of the mixing layer becomes increasingly three-dimensional and less coherent with increasing compressibility. This has been shown, for example, with two-point correlations in experimental data [127], in experimental flow visualizations [128, 129, 130], and flow visualizations in numerical simulations [125, 131, 132, 133]. Increasing strength of an oblique unstable wave with convective Mach number was also predicted by inviscid stability theory [131, 134]. Further complexity arises when the motion of the large vortices becomes supersonic relative to one or both of the external flows causing shocklets to appear. Shocklets have been observed both experimentally [130, 135] and in simulations [125, 133, 136] and typically occur at high convective Mach numbers. These shocklets can affect the turbulence dilatation, dissipation, and pressure fields [1].

A key parameter for the characterization of the compressible mixing layer is the convection velocity of the Kelvin-Helmholtz vortices in relation to one or both of the freestream velocities. Under the assumption that the mixing layer eddies convect at a constant velocity, are non-dispersive, and the streamlines are isentropic, Papamoschou & Roshko [109] conducted a theoretical analysis to derive the convective Mach number

$M_c = \Delta U/(a_1 + a_2)$ which is the velocity difference across the layer ΔU divided by the average of the sound speed a in the two streams. Despite the limitations imposed by the derivation assumptions, M_c is still the most used Mach number in the study of compressible mixing layers. Freund *et al.* [125] showed in their direct numerical simulations (DNS) of an annular mixing layer that, with increasing M_c, the cross-stream correlation length decreases in relation to the layer thickness. This indicates that the large scale eddies do not span the width of the layer at elevated Mach number. The same authors also showed that the peak turbulence stress in their simulation data scaled with the cross-stream correlation length and not the layer thickness. These results were confirmed by Pantano & Sarkar [123] who demonstrated that the pressure-strain rate correlation in their DNS scaled best with the so-called gradient Mach number. The gradient Mach number M_g is by definition the acoustic time scale divided by the flow distortion time scale and is related to the velocity difference across a large scale structure. This is in contrast to M_c which is based on the velocity difference across the entire layer. The results of Freund *et al.*[125] and Pantano & Sarkar [123] are both consistent with the previous work by Vreman *et al.*[137] who used a theoretical model of sonic eddy, a concept first introduced by Breidenthal[138], to explain an observed decrease in pressure fluctuations with increasing Mach number. Detailed turbulence statistics afforded by high fidelity numerical simulations enabled these authors [123, 125, 137] to reveal that a decrease in the pressure-strain rate correlation is directly responsible for the decrease in spreading rate with increasing Mach number. These results point to the importance of the structural changes of the large-scale mixing layer eddies in dictating both the spreading rate and the turbulence stresses.

One factor limiting our ability to translate these observations into precise scaling laws is that the parameter space has by no means been exhausted. Particularly lacking in

the research are mixing layers of high convective Mach number ($M_c > 1$), especially in the way of turbulence statistics. Aside from the notable work by Pantano & Sarkar [123], the effects of density gradient on the compressible mixing layer dynamics and their distinction from purely compressibility effects has not yet been thoroughly explored. The effect of velocity ratio also has not been fully investigated. The majority of mixing layer data are either of a single stream or two co-flowing streams. There is evidence, however, that the vortex dynamics are fundamentally different for the counter-current configuration compared to the much more widely studied co-flowing configuration. Flow visualizations of the axi-symmetric jet of Strykowski *et al.* [139] demonstrate that counter-flow shear layers can produce larger and more coherent structures than are discernible in single-stream jets at similar conditions. Linear stability analysis of both compressible and incompressible mixing layers shows the unstable mode can transition from a convectively unstable to an absolutely unstable mode under certain conditions of reverse flow strength [140, 141, 142]. Considering these changes in the nature of the instability, a question that may be asked is whether the relations between spreading rate and turbulence statistics observed in co-flowing compressible mixing layers still hold true. Another configuration of practical interest of which there is very little data available is the mixing layer subjected to a streamwise pressure gradient.

A compressible separation shear layer forms in strong shock/turbulent boundary layer interactions (STBLI). A well-known characteristic of separated STBLI is the occurrence of a low-frequency unsteadiness in the shock foot and separation bubble (among many references see for example Dussauge *et al.* [2] and Wu & Martin [3]). Many attempts have been made to discover the origins of this unsteadiness, but of particular interest to the current discussion is the work of Pipponiau *et al.*[21] who used scaling arguments

to explain the order of magnitude difference between low-frequency motions observed in STBLI and those observed in incompressible separation bubbles. In the derivation of their model, they equated the separation shear layer in their Mach 2.3 reflected shock STBLI to a canonical mixing layer and sited the Mach number dependent reduction in the spreading rate of the compressible mixing layer as the primary cause of the frequency difference. Recently, Dupont *et al.* [143] published a follow-up article to that of Piponniau *et al.* with the intention of verifying the assumptions that were made of the STBLI shear layer properties. Although decidedly not a canonical mixing layer, interestingly, Dupont *et al.* showed that the STBLI shear layer does in fact share many of the same properties. For example, they were able to collapse profiles of the mean velocity and turbulence stresses onto an approximate similarity profile by defining an appropriate, linearly varying, shear layer coordinate system. They also demonstrated that the spreading rate of the separation shear layer was consistent with the level of compressibility as determined by the convective Mach number and the measured rate of entrainment. Turbulence scaling properties of shear stress-to-spreading rate and also turbulence anisotropy-to-convective Mach number were also found to be in good agreement with mixing layer dimensional analysis. In light of these results, it would seem that the separation shear layer in STBLI flows could potentially provide significant insight into the mixing layer problem, or, at the very least, help expand the currently available parameter space.

6.2 Chapter Overview

In this chapter, we employ our LES database of separated STBLI including the Mach 3 interaction (R24-M3w-L) of Chapter 2 and the hypersonic interactions (R33-M7-L and R34-M10-L) of Chapter 3 to analyze the properties of mixing layers in hypersonic

separated flow with the intention of contributing to the research of mixing layer theory. These three separated STBLI were found to produce shear layers with convective Mach number ranging from 1 to 2. This highlights an attractive feature of STBLI separation shear layers in that they naturally occur at high convective Mach number. They also present the rare combination of high convective Mach number with reverse flow on the low-speed side. A further detail of the STBLI shear layers is that they exists in an adverse pressure gradient. We find that the pressure increases approximately linearly in the direction of shear layer development and that similarity in the mean velocity and turbulent stress profiles is still achieved under these conditions. Because we are using high fidelity, high detail LES data, we are able to obtain accurate turbulence statistics in the shear layer. The spatial/temporal resolution of the LES data also allows us to produce statistics on the shear layer turbulence structures, to visualize instantaneous realizations of the turbulence structures, and to directly calculate their convection velocity. The vortex convection velocity is an important parameter in characterizing the mixing layer yet it is notoriously difficult to measure accurately in experiments [121, 144, 145].

This chapter is organized as follows. In Section 6.4, the mean flow properties of the shear layer are tabulated. The form of the shear layer vortices is the topic of Section 6.5. The shear layer turbulence properties including turbulent kinetic energy and Reynolds stress budgets are compared with available mixing layer data and theory in Section 6.6 followed by a summary of conclusions in Section 6.7.

6.3 Nomenclature and data sampling

Throughout this chapter we use the following notation. The datasets R24-M3-L, R33-M7-L, and R34-M10-L from Capters 2 and 3 will referred to by the shorthand M3,

M7, and M10. The LES coordinate axes are indicated by capital letters (X, Y, Z) and refer to the streamwise, spanwise, and wall-normal directions respectively. The shear layer coordinate axes, to be explained in Section 6.4.1, are specified by the lowercase letters (x, y, z) where x is in the direction of the shear layer development, y is the spanwise direction, and z the cross-stream direction. Unless stated otherwise, the velocity components (u, v, w) are in the direction of the mixing layer coordinate system. In this Chapter, the symbol δ with no subscript is reserved for the mixing layer thickness whereas the boundary layer thickness is denoted by δ_{bl}.

During the runtime of the R24-M3-L, R33-M7-L, and R34-M10-L datasets, primitive flow variables were output at a high sampling rate of $f = 20U_e/\delta_{\text{bl}}$ from several stations positioned along X in the computational domain. At each station, that is at a given i-grid point, data was recorded from each j- and k-grid points. The grid indices i, j, and k refer to the streamwise, spanwise, and wall-normal grid directions respectively. For each Mach number case, there are a total of seven of these stations evenly spaced in X between $(X - X_{\text{sep}})/L = 0.3$ and 0.9 in the region of the mean separation bubble. Here X_{sep} refers to the location of the separation point in the time- and spanwise-averaged ramp flow. These high resolution time signals are used for the enhanced correlations described in Section 6.5.1 and also the flow visualizations in Section 6.5.3.

6.4 Region of Similarity in the Mean Separated Flow

6.4.1 Similarity Profiles

The STBLI separation shear layers are visualized in Fig. 6.1 by the region of elevated turbulence in the contours of mean turbulent kinetic energy $\text{TKE} = \langle u_i' u_i' \rangle / 2{U_e}^2$. In each case, the shear layer forms at the foot of the shock and makes an angle to the wall surface.

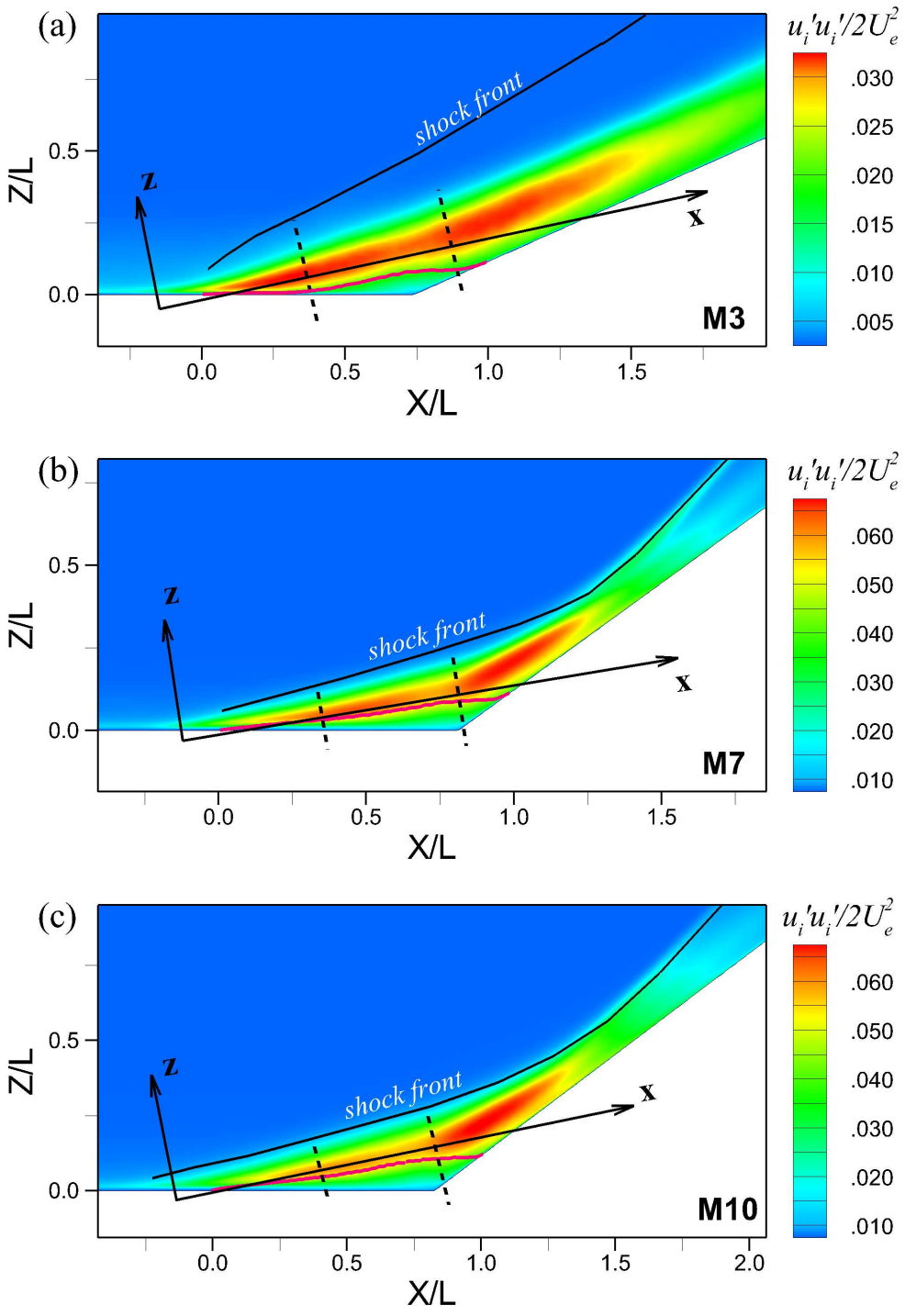

Figure 6.1: Mixing layer coordinate system definition for the (a) Mach 3, (b) Mach 7, and (c) Mach 10 compression ramp datasets. Contours are of the turbulent kinetic energy TKE = $\langle u_i' u_i' \rangle / 2{U_e}^2$. The black line is the location of the mean shock front and the magenta line is the mean dividing streamline. Dashed lines indicate the range of similarity.

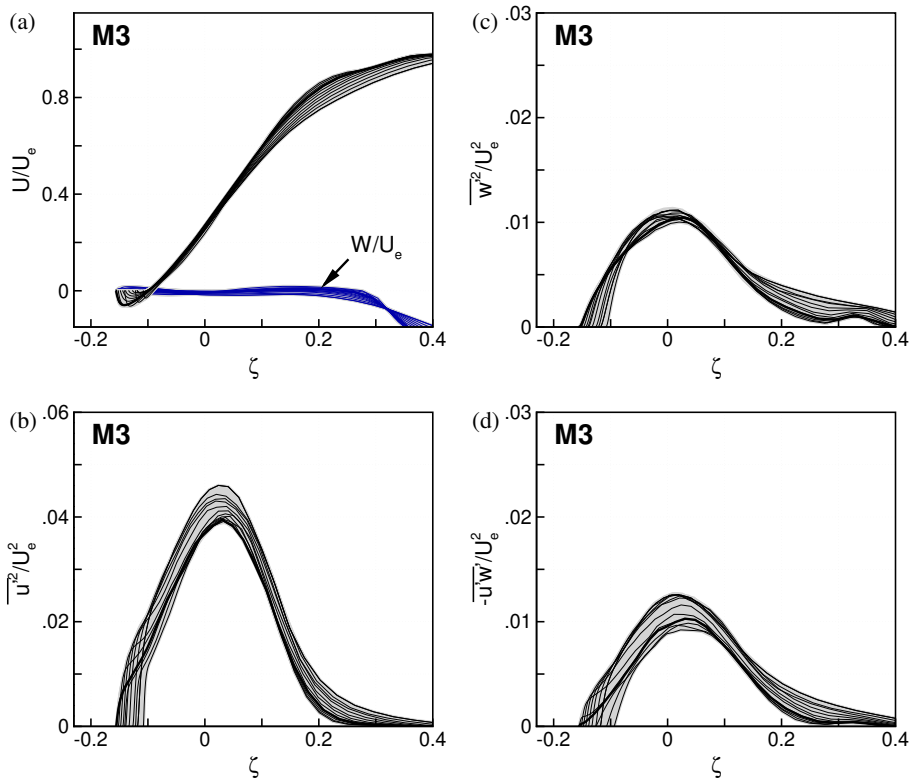

Figure 6.2: Similarity profiles in the Mach 3 STBLI separated shear layer: (a) the mean axial and cross-stream velocity, (b) axial turbulence intensity, (c) cross-stream turbulence intensity, and (d) turbulence shear stress. The bold line is the profile at the ramp corner.

The positions of the shock and the separation dividing streamline are also indicated in Fig. 6.1. A shear layer coordinate system (x, z) is defined for each case such that the longitudinal x-axis extends along the center of the layer in the direction of its development and the z-axis is perpendicular to x in the cross-stream direction. Canonical mixing layers are characterized by a linear growth rate of the layer thickness [146, 147]. If linear growth does in fact occur in the present shear flows, it should be possible to collapse profiles of the mean flow onto a single similarity profile by plotting against the similarity variable $\zeta = z/x$. In doing so, a region of approximate linear growth is found in each of the three STBLI flows.

The mean velocity and mean turbulence stresses are plotted versus ζ for M3, M7,

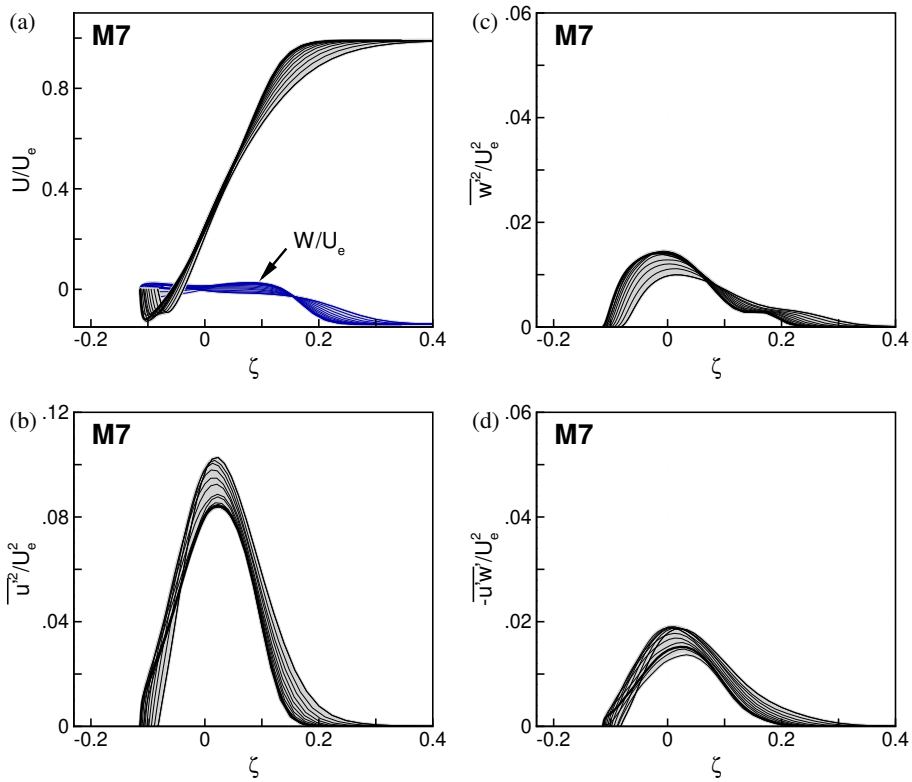

Figure 6.3: Similarity profiles in the Mach 7 STBLI separated shear layer: (a) the mean axial and cross-stream velocity, (b) axial turbulence intensity, (c) cross-stream turbulence intensity, and (d) turbulence shear stress. The bold line is the profile at the ramp corner.

and M10 in Figs. 6.2-6.4 respectively. Obtaining these profiles required the positioning of the shear layer coordinate system xz-axes, the rotation of which was determined by the orientation of the mean velocity field, and the origin by the angle of spread observed in the contour of mean TKE. This manual placement of the mixing layer coordinates is similar to the method used by Dupont *et al.*[143]. The position of the xz-axes for each case are shown in Fig. 6.1. The angles of inclination for the Mach 3, 7, and 10 flows are 12.0°, 8.5°, and 10.0° respectively. The bold dashed lines in Fig. 6.1 indicate the range in x for which a good collapse of the similarity profiles was found. The profiles of Figs. 6.2-6.4 were taken from this range.

The collapsed profiles themselves resemble quite well those of the classic mixing

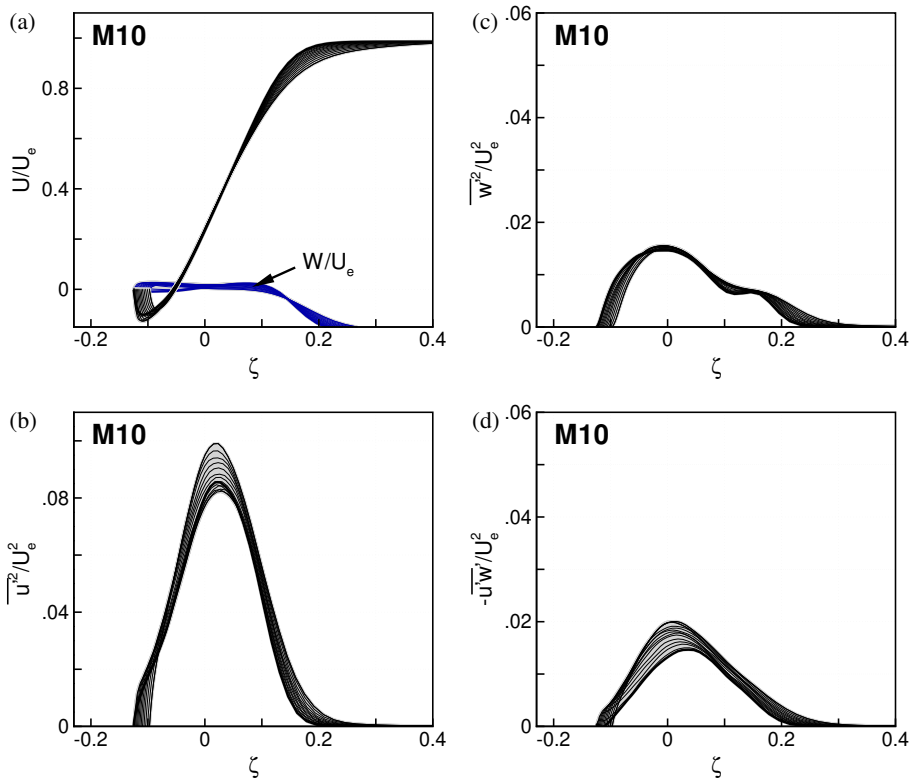

Figure 6.4: Similarity profiles in the Mach 10 STBLI separated shear layer: (a) the mean axial and cross-stream velocity, (b) axial turbulence intensity, (c) cross-stream turbulence intensity, and (d) turbulence shear stress. The bold line is the profile at the ramp corner.

layer. The mean longitudinal velocity profiles show high and low velocities connected by a single inflection point, and the profiles of turbulence stress are approximately Gaussian with the peak coinciding with the location of the inflection point in the mean velocity U. Both of these features are typical of the canonical mixing layer and together they produce the Kelvin-Helmholtz inviscid instability [148]. Unlike the classic mixing layer similarity solution, the collapsed profiles for all three shear layers appear to be non-symmetric with the turbulence peak (equivalently the inflection point in the mean velocity) biased towards the high speed side of the layer. It is shown in Section 6.6 that this bias is a result of the proximity of the wall on the low-speed side. The profiles of mean cross-stream velocity show that W is essentially zero across the layer for all three cases indicating that the

mean velocity is nearly parallel to the x-axis. The minimal variation in W across the layer is also consistent with a reduced entrainment rate, and therefore reduced spreading rate as is expected for highly compressible mixing layers. This point is discussed further in Section 6.4.4.

6.4.2 Two-Stream Properties

Encouraged by the quality of collapse of the profiles as well as their resemblance to the canonical free mixing layer flow, we make an attempt to categorize these STBLI shear layers in the manner of conventional compressible mixing layers. To do so we must describe each shear layer as two streams, a high- and a low-speed stream, each with constant velocity and constant thermodynamic properties. As can be seen in Figs. 6.2-6.4 this will only be an approximation as all profiles deviate from the typical mixing layer solution near the edges of the layer. Spreading occurs at the low-speed end of the profiles due to the presence of the wall and at the high speed end due to the presence of the separation shock (the location of the shock in ζ is easily seen in the profiles of W). It will be shown, however, that even a rough estimation of the mean properties of the two streams is sufficient for a general comparison to canonical mixing layer data. The estimations of the two stream properties for each shear layer are listed in Table 6.1. The methods for determining the entries of Table 6.1 are discussed below. By convention, properties associated with the high-speed side are indicated with the subscript "1" and the low-speed side with subscript "2".

The velocity U_1 and temperature T_1 for each case are estimated as the inviscid post-shock solution for the STBLI freestream undergoing a flow deflection equal to the angle of inclination of the x-axis. This selection of U_1 and T_1 stems from the observation that the

Case	U_1 (m s^{-1})	T_1 (K)	M_1	U_2 (m s^{-1})	T_2 (K)	M_2	dp/dx (p$_1$ L^{-1})	s	r	M_c	$U_{c,\mathrm{i}}$ (m s^{-1})
M3	551	140	2.3	-36	279	0.1	0.52	0.541	-0.065	1.03	308
M7	1115	99	5.6	-137	537	0.3	1.20	0.299	-0.123	1.89	739
M10	1368	115	6.3	-142	707	0.2	0.86	0.333	-0.104	1.99	934

Table 6.1: Averaged mixing layer flow properties.

rotated mean W profiles are essentially zero for all three shear layers. It is worth noting that we found the initial deflection angle of the separation shock, as shown for each case in Fig. 6.1, corresponds closely to the resulting wave angle of the oblique shock solution. The high speed stream Mach number M_1 is determined from U_1 and T_1. The M7 and M10 flows maintain Mach number above 5 downstream of the separation shock and can be considered hypersonic shear layers.

The velocity U_2 of the low-speed side is estimated as the minimum in the similarity profiles of U in Figs. 6.2-6.4 (a). The low-speed side T_2 is likewise determined from the similarity profiles of temperature which are plotted in Fig. 6.5. All three cases show a satisfactory collapse of temperature within the previously defined range of approximate similarity. In each shear layer, however, there occurs a "hook-off" of the temperature profiles on the low-speed side. This is due to the constant temperature boundary condition at the wall. The wall temperature of the Mach 3 case is nearly adiabatic and so the divergence of the profiles in Fig. 6.6 (a) is minimal. Because the Mach 7 and Mach 10 are both cold-wall simulations, the temperature drops significantly inside the separation bubble as seen in Fig. 6.5 (b-c). The low speed T_2 is therefore estimated as the maximum value in temperature just before the profiles diverge to meet the wall boundary condition. The two hypersonic shear layers have large temperature ratios such that T_2 experiences an increase of over 5 times T_1 for the M7 case and nearly 7 times for the M10 case. In

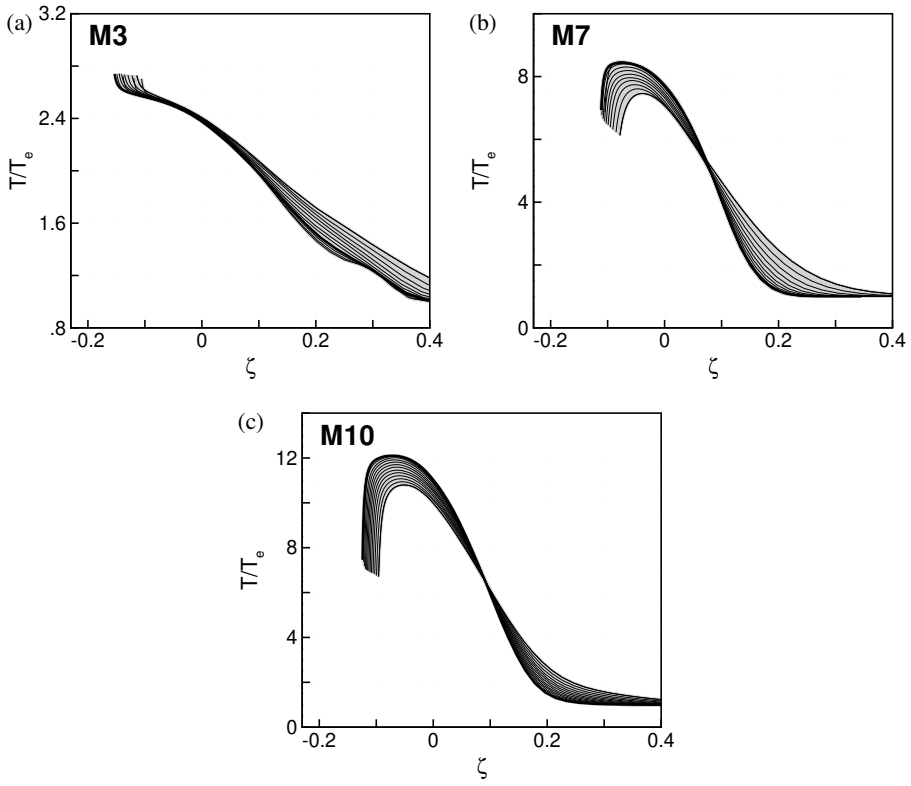

Figure 6.5: Similarity profiles of temperature in the (a) Mach 3, (b) Mach 7, and (d) Mach 10 STBLI separated shear layers.

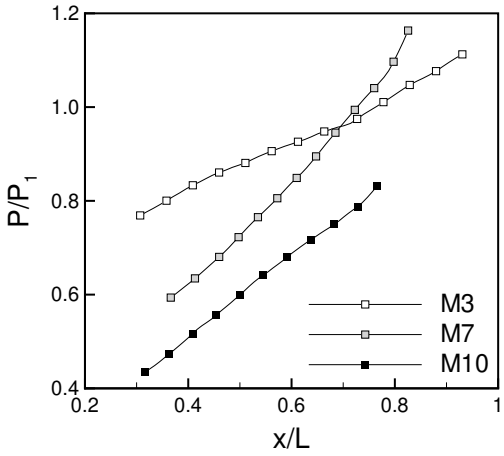

Figure 6.6: Pressure gradient along the shear layer centerline.

comparison, the M3 case T_2 is only double the value of T_1. Also listed in table 6.1 is the low-speed stream Mach number M_2 calculsed from U_2 and T_2.

Because the separated flow is shock-induced, an adverse pressure gradient occurs along the length of the shear layer. Figure 6.6 shows that the pressure increases nearly linearly along the x-axis for all three cases. The reference pressure p_1 is the post-shock pressure from the oblique shock solution from which U_1 and T_1 are obtained. The average rate of pressure increase dp/dx in units of p_1/L was determined from a linear fit to the data of Fig. 6.6. For the Mach 3 flow the pressure increases by nearly 50% across the region of similarity, while for the Mach 7 and Mach 10 flows the pressure approximately doubles. As a result of the adverse pressure gradient, the mean density plotted versus ζ does not collapse when normalized by the freestream density as is apparent in Figss 6.7 (a), (c), and (d). The density is seen to increase significantly from the most upstream profile to the most downstream profile. However, a much better collapse is achieved if each individual profile of ρ is non-dimensionalized by the local $\rho_2(x)$. The inverse of ρ non-dimensionalized by $\rho_2(x)$ is plotted in Fig. 6.7 (b), (d), and (f). That is, although

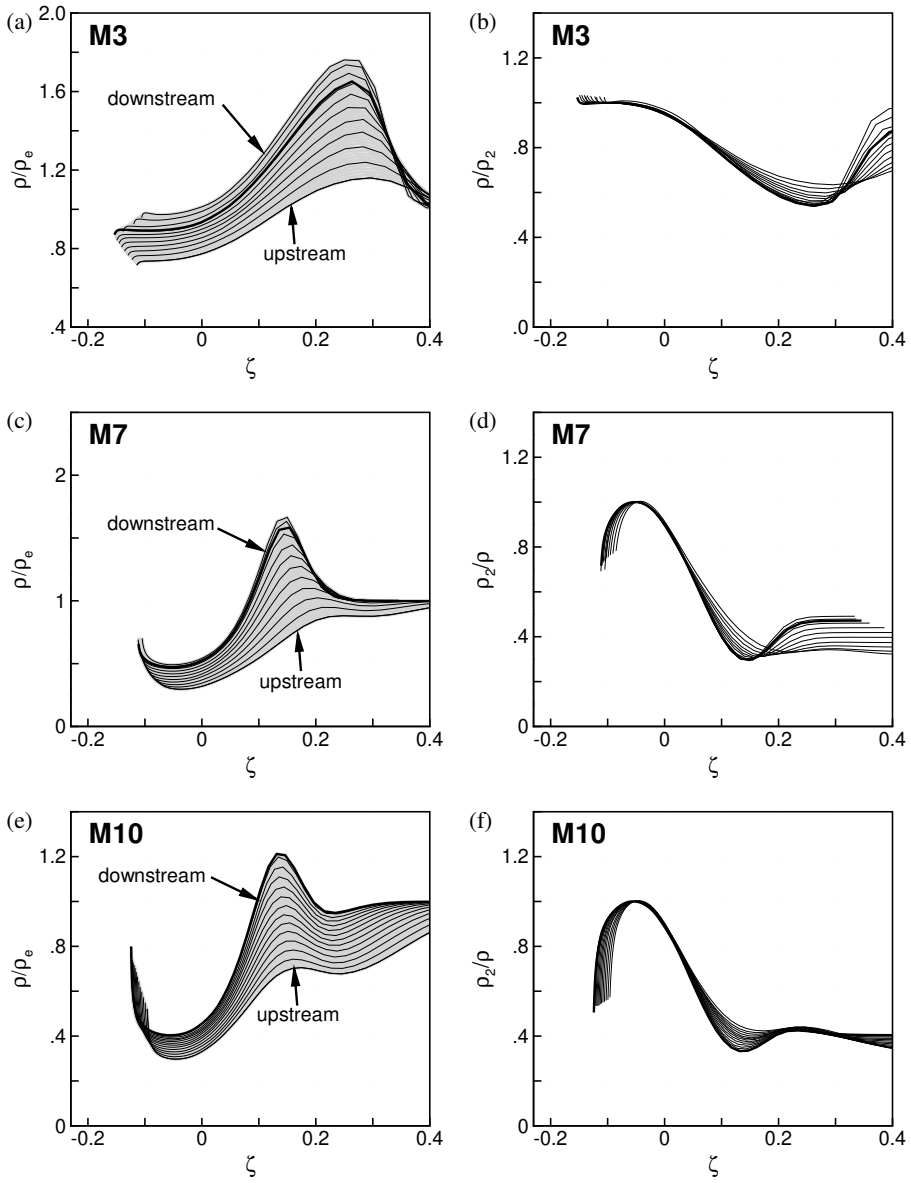

Figure 6.7: Similarity profiles of density in the (a)-(b) Mach 3, (c)-(d) Mach 7, and (e)-(f) Mach 10 STBLI separated shear layers. The profiles on the left are normalized by the freestream density. On the right are profiles of the inverse density normalized by the density of the low-speed side, that is, ρ_2/ρ. Plotting density in this way shows the variation in $s = \rho_2/\rho_1$.

there is a monotonic increase in density along x, the ratio between the two streams is approximately constant. Therefore, only the density ratio $s = \rho_2/\rho_1$ is reported in table 2. The value of local $\rho_2(x)$ was determined from the individual profiles in Figs. 6.7 (a-c) in a manner similar to the selection of T_2 from the profiles of temperature. Note that the density could have equivalently been non-dimensionalized by the local $\rho_1(x)$ to obtain the collapse. We chose to use $\rho_2(x)$ because this quantity was easier to select from Figs. 6.7 (a-c). The Mach 3 STBLI flow produces a density ratio of approximately 1/2 across the shear layer while both the Mach 7 and Mach 10 interactions produce a density ratio of 1/3. Also included in Table 6.1 is the velocity ratio $r = U_2/U_1$ for each case.

6.4.3 Convection Mach Number

Now that the properties of the shear layer high- and low-speed streams are known, the theoretical convective Mach number defined as

$$M_c = \frac{U_1 - U_2}{a_1 + a_2} \tag{6.1}$$

and also the theoretical mixing layer vortex convection velocity $U_{c,i}$ defined as

$$U_{c,i} = \frac{a_1 U_2 + a_2 U_1}{a_1 + a_2} \tag{6.2}$$

can be calculated for these flows. These expressions for the convective Mach number and convective velocity are derived for an isentropic mixing layer where a_1 and a_2 are the spead of sound in the two streams [107, 109]. The M_c and $U_{c,i}$ are computed for each case and listed in Table 6.1. An interesting feature of the separated STBLI flows is that they produce shear layers with rather high M_c even for the Mach 3 compression ramp flow.

All three shear layers are above $M_c = 1$. This is an attractive feature considering that the majority of mixing layer data available today, particularly for turbulence statistics, is below $M_c = 1$.

For mixing layers with M_c above 1 it is likely that shock waves exist in one or both sides of the mixing layer, thus negating the isentropic assumption in the derivation of Eqns. 6.1 and 6.2. We will show later in Section 6.5.2 that the theoretical $U_{c,\mathrm{i}}$ in Table 6.1 is quite different from the convection velocity determined from enhanced two-point correlations.

6.4.4 Spreading Rate

Despite its known limitations as a scaling parameter, the convective Mach number defined by equation 6.1 is currently the most widely accepted metric in the literature for classifying the compressibility effects of mixing layers [1]. One such classification is the observed significant decrease in layer spreading rate with increasing M_c. Smits & Dussauge [1] presented a compilation of compressible mixing layer spreading rate data, expressed as a fraction of the spreading rate of an equivalent incompressible mixing layer with the same values of r and s, and plotted these versus M_c (see figure 6.6 in reference). Included in the data compilation are the classic Langley curve [105, 106], the semi-empirical curve by Dimotakis [113], and the linear stability analysis prediction of spreading rate decrease with M_c by Day *et al.* [132]. The data show that the spreading rate can decrease by as much as 50% to 80% from the incompressible case for M_c above 0.5. For the current data, normalized spreading rate predictions from the classic Langley curve are approximately 0.55 for the Mach 3 flow and 0.40 for both the Mach 7 and Mach 10 cases as determined by the values of M_c in table 6.1.

Case	$\delta'_{u'}$	$\delta'_{u'w'}$	δ'_{inc}	$\delta'_{u'}/\delta'_{\text{inc}}$	$\delta'_{u'w'}/\delta'_{\text{inc}}$
M3	0.265	0.238	0.311	0.853	0.766
M7	0.195	0.194	0.297	0.656	0.653
M10	0.205	0.202	0.296	0.692	0.682

Table 6.2: Spreading rate estimates and comparison to incompressible theory.

For the STBLI shear layers, the spreading rate of vorticity thickness $\delta' = d\delta_\omega/dx$ where $\delta_\omega = \Delta U/\max(dU/dz)$ can be estimated using the two different methods outlined by Dupont *et al.*[143]. The first of these uses a comparison of the normalized $\langle u'^2 \rangle$ similarity profile with the same from an incompressible mixing layer. Here the two-stream mixing layer data of Mehta & Westphal [149] (figure 5(b) in reference) is used. This first method assumes that the shape of the $\langle u'^2 \rangle$ profile as well as the ratio of $(d\delta_\omega/dx)/d\zeta$ do not differ between the compressible and the incompressible cases. The second method involves fitting a Gaussian curve to the profiles of turbulent shear stress. Both methods provide consistent results. These are listed in table 6.2.

A theoretical estimate of the spreading rate for an incompressible mixing layer with non-zero density ratio s can be determined from the relation derived by Papamoschou & Roshko [109]

$$\delta'_{\text{inc}} = \delta'_{\text{ref}} \frac{(1-r)(1+\sqrt{s})}{(1+r\sqrt{s})}. \tag{6.3}$$

In equation 6.3, δ'_{ref} is a reference spreading rate from an incompressible mixing layer with $s = 1$ and $U_2 = 0$ and is typically taken to be equal to 0.16 [1]. The STBLI shear layer spreading rates are also listed in table 6.2 as a fraction of the corresponding incompressible estimate. The spreading rate ratios are less than unity however they are approximately 50% to 70% higher than the Langley curve predictions. The Langley curve, however, is based primarily on data for single or two stream co-flowing mixing layers. It

has been shown that the spreading rate can be significantly greater for counter-current mixing layers [139, 150] and also for mixing layers subjected to adverse pressure gradients [151]. Although there is significantly less data on the counter-current mixing layer than the co-flowing configuration, one notable work is that of Strykowski *et al.* [139]. The authors performed a series of counter-flowing axi-symmetric jet experiments at $M_c \approx 1$ with varying reverse flow strength. They showed that the spreading rates were consistently 60% greater than the case of a single stream jet. Another consideration is that equation 6.3 might not be an accurate approximation for the spreading rate of incompressible counter-current mixing layers. Strykowski *et al.* [139], however, also showed that equation 6.3 was valid for their experimental data if the reverse flow strength did not exceed $r < -0.1$. Even still, the disagreement for $r < -0.1$ was sited by the authors as possibly due to an artifact of their jet nozzle. At any rate, the shear layer data in table 6.2 clearly shows a decrease in spreading rate from the M3 case at $M_c \approx 1$ to the M7 and M10 cases at $M_c \approx 2$.

6.5 Vortex Signature and Convection Velocity

The similarity profiles of the mean velocity and turbulence stresses presented in section 6.4.1 indicate that the criteria for the inviscid Kelvin-Helmholtz instability exist in the STBLI shear layers, and so it is expected that there will be large spanwise-oriented vortices present in the flow. Changes in the global characteristics of the compressible mixing layer as compared to the incompressible condition may be better understood through observation of the dynamics of the large vortical structures. The detection and description of the average signature of these vortices is the subject of this section.

6.5.1 Enhanced Correlations

A schematic of the shear layer in the compression ramp STBLI flow is given in Fig. 6.8. On the left is shown a model of the spatial development of the mixing layer structur es as they convect along the x-axis. It is assumed that the vortices convect at a constant velocity U_c and that they follow one after the other at fairly regular intervals. It is also assumed that they do not stray too far from the shear layer centerline. At reattachment the vortices are shed into the downstream flow. These assumptions are based on observations of the temporally- and spatially-resolved LES data and are verified in Section 6.5.3 by the instantaneous vortex visualizations. If the flow is probed at a stationary point in the shear layer, the resulting time signals can be converted to spatially "frozen" turbulence via Taylor's hypothesis. This is drawn schematically on the right side of Fig. 6.8. The average signature of the frozen turbulence can be determined from the cross-correlations of the time signals of mass flux and pressure fluctuations in the following way. Consider for example the time signal of pressure taken from a point along the centerline of the shear layer. As a vortex core convects past the probe location there will be a negative fluctuation in the pressure. Likewise, in-between successive vortices there will be a positive pressure fluctuation from the stagnation point in the convective reference frame. In a similar way, the time signal of longitudinal mass fluctuations $(\rho u)'$ taken near the bottom edge of the shear layer will give information on the aperiodic signature of the passing vortices due to the orientation of the vortex rotation. Taking the cross-correlation between the centerline p' and the bottom edge $(\rho u)'$ time signals produces a sinusoidal signature, the period of which is equal to the average time between successive vortices as they convect past the probe points. Although not shown in the schematic of

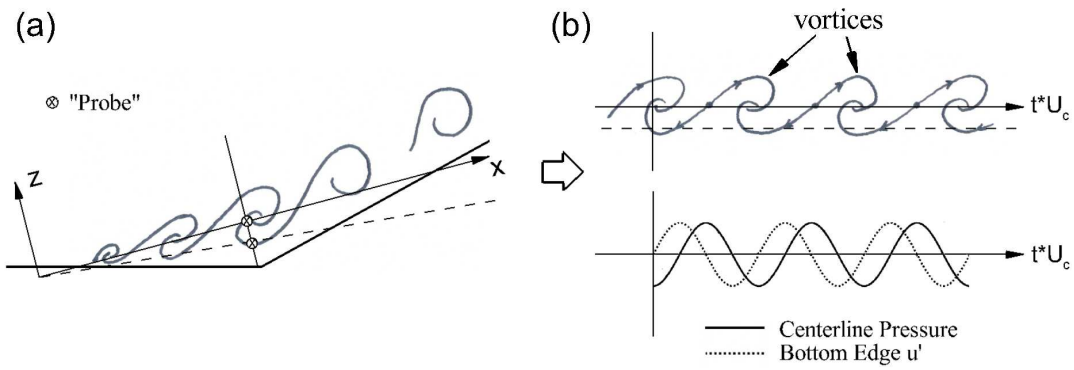

Figure 6.8: Schematic of the vortex structures (a) in the spatially developing shear layer in the separated compression ramp STBLI flow and (b) time signals taken from within the shear layer converted to "frozen" vortices by using Taylor's hypothesis.

Fig. 6.8, similar arguments can be made for cross-correlations between centerline p' and centerline cross-stream momentum $(\rho w)'$. Here we consider both $R_{(\rho u)'p'}$ and $R_{(\rho w)'p'}$.

A similar cross-correlation method was demonstrated by Kiya & Sasaki[152] and also Cherry *et al.* [153] for an incompressible separation shear layer, and Samimy *et al.*[127] for compressible mixing layers. There are a couple of points to be made on the cross-correlation method used here. First, the signal of longitudinal momentum fluctuations could be taken from either the top or bottom edge of the shear layer. Kiya & Sasaki [152] for example used the high speed edge. In this analysis, the bottom edge was chosen so as to avoid the separation shock. Second, auto-correlations of pressure with itself will also give a periodic correlation curve as demonstrated by Kiya & Sasaki [152], Cherry *et al.* [153], and Samimy *et al.*[127]. Here cross-correlations of p' and $(\rho u)'$ and also p' and $(\rho w)'$ were used in order to couple the mass flux and pressure field events, that is, to ensure that a pressure fluctuation is accompanied by a corresponding mass fluctuation. We found this strategy also ensures a more robust selection method for the enhanced correlation technique to be described shortly. Last, it was found that nearly identical correlation signatures were

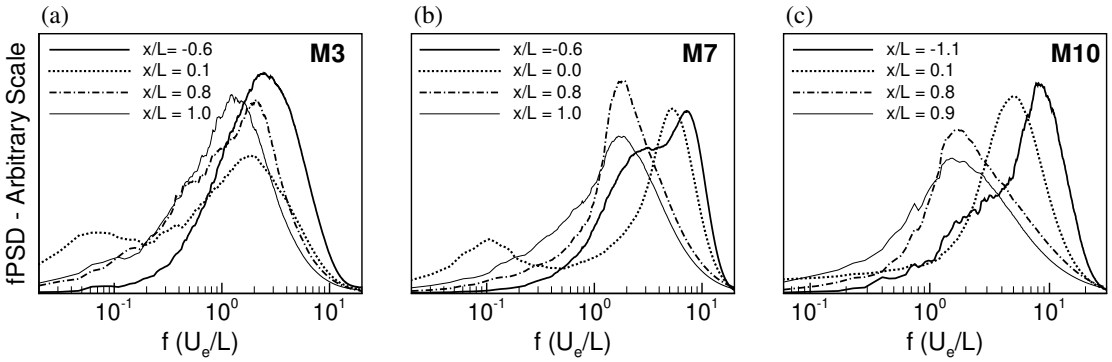

Figure 6.9: Pre-multiplied power spectral density of wall pressure signals from the (a) Mach 3, (b) Mach 7, and (c) the Mach 10 data. Spectra are shown for the upstream boundary layer (solid bold), separation point (dotted), corner (dashed bold), and reattachment (solid).

achieved when correlating velocity with pressure compared to correlating mass flux with pressure. In general the mass flux correlations provided a stronger signature and so only the mass flux and pressure correlations are included in this paper.

The details of the correlation method are as follows. Before calculating the cross-correlations, the signals of pressure and velocity are first bandpass filtered in time. Fully separated STBLI flows are characterized by frequency spectra consisting of three distinct broadband ranges of energized turbulence motions. These are associated with (1) the inherent low-frequency unsteadiness of the separated flow, (2) the mixing layer vortices, and (3) the fine scale boundary layer turbulence. To demonstrate these frequency bands, pre-multiplied power spectral density (PSD) of wall pressure taken in the upstream boundary layer, the mean separation point, the ramp corner, and the mean reattachment point are plotted in Fig. 6.9 for each of the three STBLI flows. These spectra were calculated using Welch's method with eight time segments with 50% overlap and then bin sampled with a bin width of 0.1 in the log scale. From these spectra it is possible to make out the shifts in the distribution of turbulence energy as the flow progresses through the separated region.

In the boundary layer, only the high frequency turbulence exists with little to no

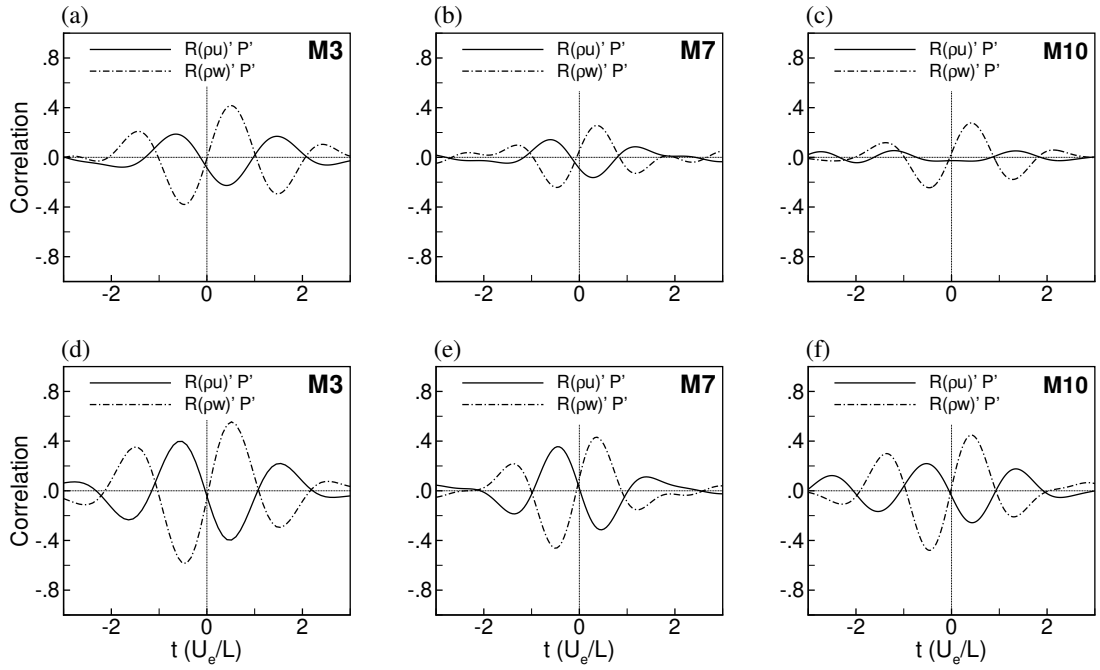

Figure 6.10: Cross-correlations between bandpass filtered mixing layer centerline pressure and massflux signals at the corner profile of each dataset. Averaged over full time signal (a-c) and enhanced average (d-f).

energy present at the lowest frequencies. The undisturbed boundary layer turbulence is generally centered at $St_\delta = f\delta_{bl}/U_e = 1$ and experiences a shift to $St_L = 1$ downstream of the shock. This shift in the boundary layer turbulence can be seen when comparing the broadband energy peaks between the most upstream and most downstream spectra. The low-frequency oscillations of the shock appear in the separation spectra. It is well documented in the literature that the low-frequency oscillations in quasi-two dimensional separated STBLI flows occurs at $St_L = fL/U_e$ on the order of 0.01 (Among many references, see for example Dupont *et al.* [11] for reflected shock interactions and Priebe & Martin [12] for compression ramp interactions). The relative strength of the low-frequency oscillations diminishes downstream, however, there still remains elevated energy at these frequencies in the corner and reattachment spectra. Although not appearing as a distinct peak in the pre-multiplied PSD, a substantial increase in energy at frequencies of approx-

imately $St_L = 0.5$ occurs in the corner and reattachment spectra when compared to the first two spectra profiles. The increase in energy content at these intermediate frequencies is attributed to the development of the mixing layer turbulence [11]. Because the three energized frequency ranges are separate from each other, even more so as the ratio L/δ_{bl} increases, it is possible to filter out both the low-frequency oscillations and the fine scale boundary layer turbulence from the mixing layer time signals. Therefore, a bandpass filter is designed for each case to retain frequencies between $St_L = 0.3$ and $St_\delta = 0.2$. Note that the low-frequency cutoff scales on L and the high frequency cutoff on δ_{bl}.

Correlation curves of $R_{(\rho u)'p'}$ and $R_{(\rho w)'p'}$ from bandpass filtered time signals taken from the corner profile in each of the Mach 3, 7, and 10 flows are plotted in Figs. 6.10 (a-c). The corner profile refers to the slice through the mixing layer that intersects the ramp corner as drawn in Fig. 6.8 (a). The signals of p' and $(\rho w)'$ are taken at $\zeta = 0$ on the x-axis and $(\rho u)'$ along the bottom edge of the shear layer at $\zeta = -0.06$. The time axis is oriented so that a positive time shift indicates a motion of the fluid, $(\rho u)'$ or $(\rho w)'$, that occurs before the correlated fluctuation in pressure. Time is non-dimensionalized by the pre-shock freestream velocity U_e and separation length L. Both the $R_{(\rho u)'p'}$ and $R_{(\rho w)'p'}$ curves are sinusoidal and are almost perfectly out of phase with each other. Only $R_{(\rho u)'p'}$ for the Mach 10 case fails to have a noticeable signature. A decrease in the mixing layer structure correlation level with increasing M_c was also observed by Samimy *et al.* [127]. The Mach 7 and Mach 10 flows, both $M_c \approx 2.0$, have a noticeably smaller amplitude than the Mach 3 with $M_c \approx 1.0$. The approximate period of the correlations is $2L/U_e$ which is consistent with the expected $St_L = 0.5$ for the mixing layer frequencies.

Although a distinct sinusoidal signature is visible in the full time signal correlations, the overall magnitude of the correlation is rather low particularly for M7 and M10. In

order to obtain a stronger signature of the vortex events, an enhanced correlation method is used. The conditional averaging technique used here is similar to the method of Brown & Thomas [154] for the detection of hairpin packets in a turbulent boundary layer. The strategy of Brown & Thomas assumes that the hairpin packet, or in this case the mixing layer vortex, is a specific isolated event occurring in the flow and that the corresponding fluid motion, or pressure fluctuation, associated with that event produces a specific signature in the time signal. Time signals of relevant fluid properties can be broken up into shorter segments and the cross-correlation computed for each of the shortened segments. If a vortex occurs in a given segment, the cross-correlation curve of that segment will produce the "signature" of the vortex event. The enhanced correlation, therefore, is the average over all of the short-signal correlations that show the vortex signature.

For the detection of the mixing layer vortices, the time signals of p', $(\rho u)'$, and $(\rho w)'$ are broken up into N segments of length $6.5U_e/L$, or twice the wavelength of the bandpass filter low-frequency cutoff. Successive time segments are taken with 50% overlap. We assume that the signature of the mixing layer vortices has the same form as the full time signal correlations. The criteria for the selection of the enhanced correlations are such that the segment correlations ${R^n}_{(\rho u)'p'}$ and ${R^n}_{(\rho w)'p'}$ simultaneously have maxima and minima in the same location as, but at least twice the magnitude of, the full time average signature. More specifically, a correlation is retained if (1) $\max({R^n}_{(\rho u)'p'}) \geq 2\max(R_{(\rho u)'p'})$ and (2) $\min({R^n}_{(\rho w)'p'}) \leq 2\min(R_{(\rho w)'p'})$ both in the range $-2 \leq \Delta t(U_e/L) \leq 0$ for $n \in N$. The enhanced results for the corner profile are shown in Figs. 6.10 (d-f). For the Mach 3, approximately 30% of the time segments met the criteria, and approximately 20% for the Mach 7 and Mach 10 flows. A distinct wavelength appears in the enhanced correlation for all three cases including the Mach 10 $R_{(\rho u)'p'}$.

6.5.2 Convection Velocity

The enhanced correlation technique was repeated for several stations along the x-axis. The frequency in St_L determined from the $R_{(\rho u)'p'}$ enhanced correlation curve time period are plotted in Fig. 6.11 (a) versus X/L. Although not shown, the time period selected from the enhanced correlations of $R_{(\rho w)'p'}$ produces similar frequencies to those from $R_{(\rho u)'p'}$. The frequency is approximately constant through the region of similarity for each case. Dupont *et al.* [11] also showed that the shear layer frequency plateaus at a constant $St_L = 0.5$ in the separated flow of their reflected shock STBLI with freestream Mach number of 2.3. They also showed that this frequency was independent of the incident shock angle.

The enhanced correlations can be used to determine the actual mixing layer vortex co nvection velocity U_c. At a given position on the x-axis, if a time segment is selected by the enhanced correlation criteria, the centerline pressure signal from that time segment can be correlated with the same from an adjacent position along x. The convection velocity of that vortex event is then obtained by dividing the distance between the two points in x by the offset in time of the peak in $R_{p'p'}$. The U_c can then be averaged over all enhanced correlation selections. Here the cross-correlation of adjacent pressure signals is used because the theoretical $U_{c,i}$ discussed in section 6.4.3 is by definition the convection velocity of the stagnation point between successive vortices [1, 109]. The averaged convection velocity versus X/L is plotted in Fig. 6.11 (b). For the cross-correlations of pressure, adjacent points are spaced approximately $0.1L$ apart. An average of both the forward adjacent point and the backward adjacent point correlation is used to calculate U_c at each data point plotted in Fig. 6.11 (b). The convection velocity seems to undergo a gradual

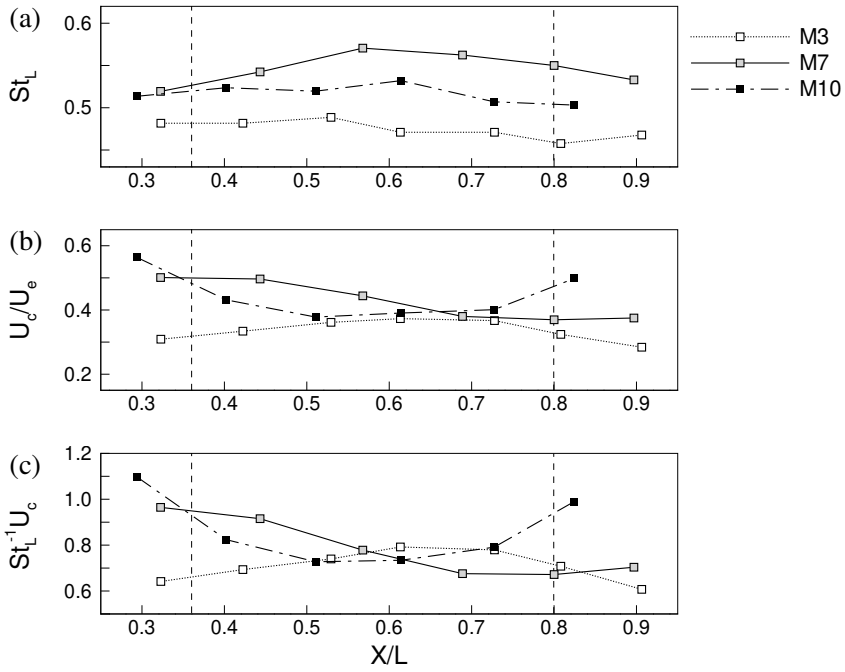

Figure 6.11: Non-dimensional vortex frequency (a), convection velocity (b), and length scale (c) determined from the enhanced correlations.

transition in the first half of the similarity region, but, for all three flows, U_c levels off at $0.4U_e$ in the second half of the region of similarity. For comparison, $U_{c,i}$ calculated from equation 6.2 is $0.5U_e$ for the M3 flow and $0.6U_e$ for M7 and M10. A similar comparison was made by Dupont *et al.* [11] for their Mach 2.3 reflected shock experiments. They found the phase velocity of wall pressure signals in the frequency range of $0.2 \leq St_L \leq 0.5$ gave a shear layer convection velocity of approximately $0.3U_e$ compared to the isentropic prediction of $0.5U_e$. In either case of the compression ramp or the reflected shock flow, the theoretical convection velocity significantly over predicts the measured vortex convection velocity.

The timescale of Fig. 6.11 (a) and the convection velocities of Fig. 6.11 (b) can be combined to estimate the spatial wavelength of the frozen vortices. The spatial quantity $St_L^{-1}U_c$ is plotted in Fig. 6.11 (c) and represents the average distance between successive

vortex cores. As with the convection velocity, the wavelength seems to reach a constant value in the second half of the region of similarity, leveling off at approximately $0.8L$ spacing for all three flows.

6.5.3 Three-Dimensional Vortex Signature

In order to investigate the spatial organization of the large vortex structure in our STBLI mixing layers, the following correlation coefficient is defined

$$R_{f'p'} = \frac{\langle f'(x+\Delta x, y+\Delta y, z+\Delta z)p'(x,y,z_{cl})\rangle}{f'_{\text{rms}}p'_{\text{rms}}} \tag{6.4}$$

where f' can refer to either $(\rho u)'$ or $(\rho w)'$, and $p'(x,y,z_{cl})$ is the pressure along the mixing layer center line. Again Taylor's hypothesis of frozen vortices is used to convert time signals into spatial information and so, in Eqn. 6.4, we set $x = tU_c$ where U_c is the convection velocity determined from the enhanced correlations described above. The enhanced spatial correlation can be generated in the same manner as the one-dimensional (1D) correlations by averaging $R_{f'p'}$ over all time segments selected by the previously defined criteria. The enhanced spatial correlations of bandpass filtered time signals from the corner profiles of the Mach 3, 7, and 10 flows are plotted in Figs. 6.12, 6.13, and 6.14 respectively. These plots represent the averaged "frozen" spatial waveform of the mixing layer vortices as they convect past the corner profile as drawn schematically in Fig. 6.8. In Figs. 6.12-6.14, figure (a) is the enhanced average in the xz-plane for $\Delta y = 0$, and figure (b) is the enhanced average in the xy-plane for $R_{(\rho u)'p'}$. Figures (c) and (d) are the same for $R_{(\rho w)'p'}$. The z-location of the xy-plane is indicated by the solid black line in the corresponding figure (a) and also in (c). For $R_{(\rho u)'p'}$ the xy-plane is along the mixing layer bottom edge as was defined for the 1D enhanced correlations. For $R_{(\rho w)'p'}$ the xy-plane

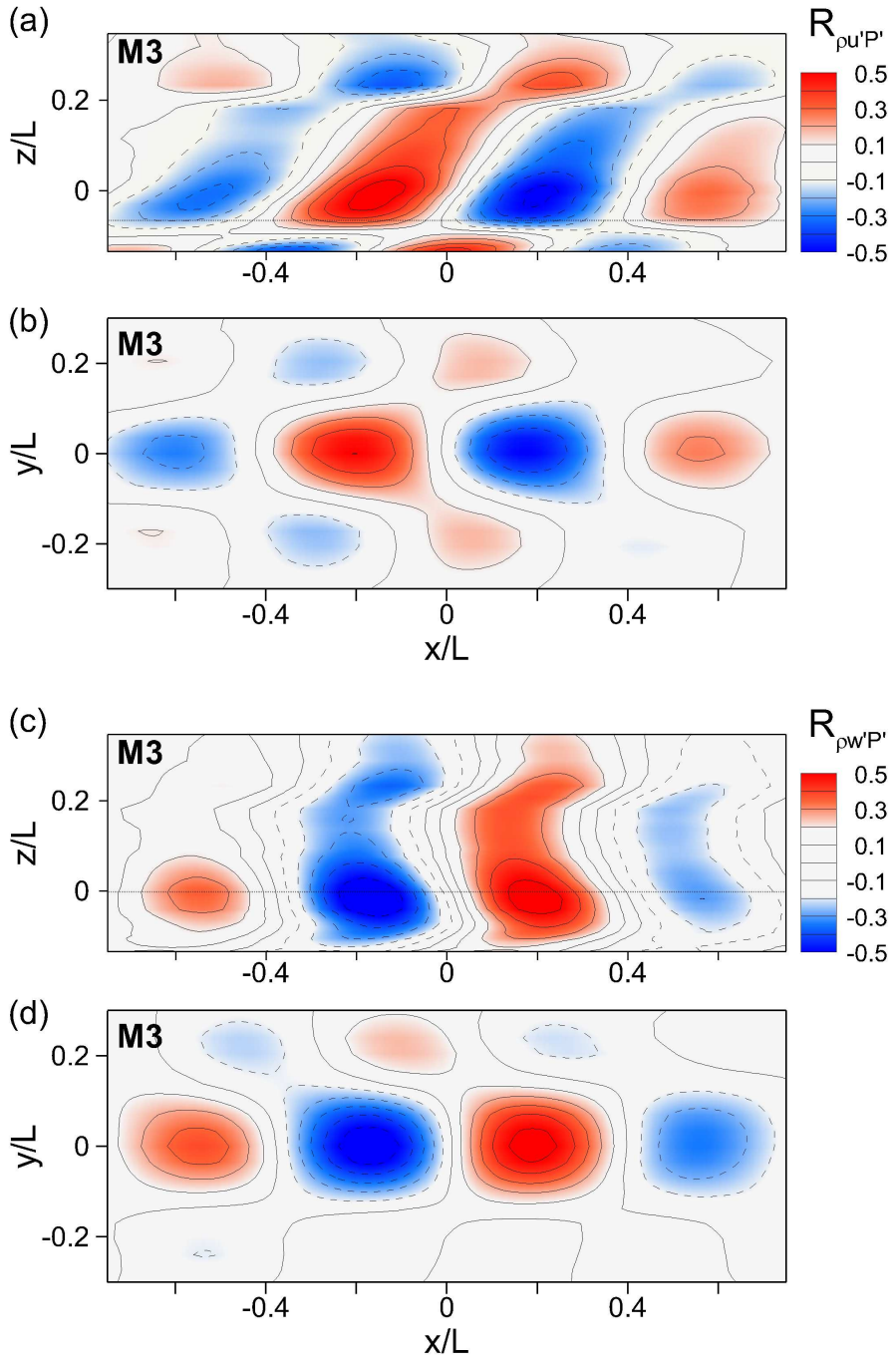

Figure 6.12: Enhanced correlation contours of the Mach 3 convective mixing layer structure. Correlations are of centerline pressure with longitudinal massflux in (a) xz- and (b) xy-planes and centerline pressure with cross-stream massflux in (c) xz- and (d) xy-planes. The horizontal dotted line in the xz-planes indicates the location of the corresponding xy-plane. Time correlations are converted to spatial information using the mixing layer convection velocity (i.e $x/L = tU_c/L$).

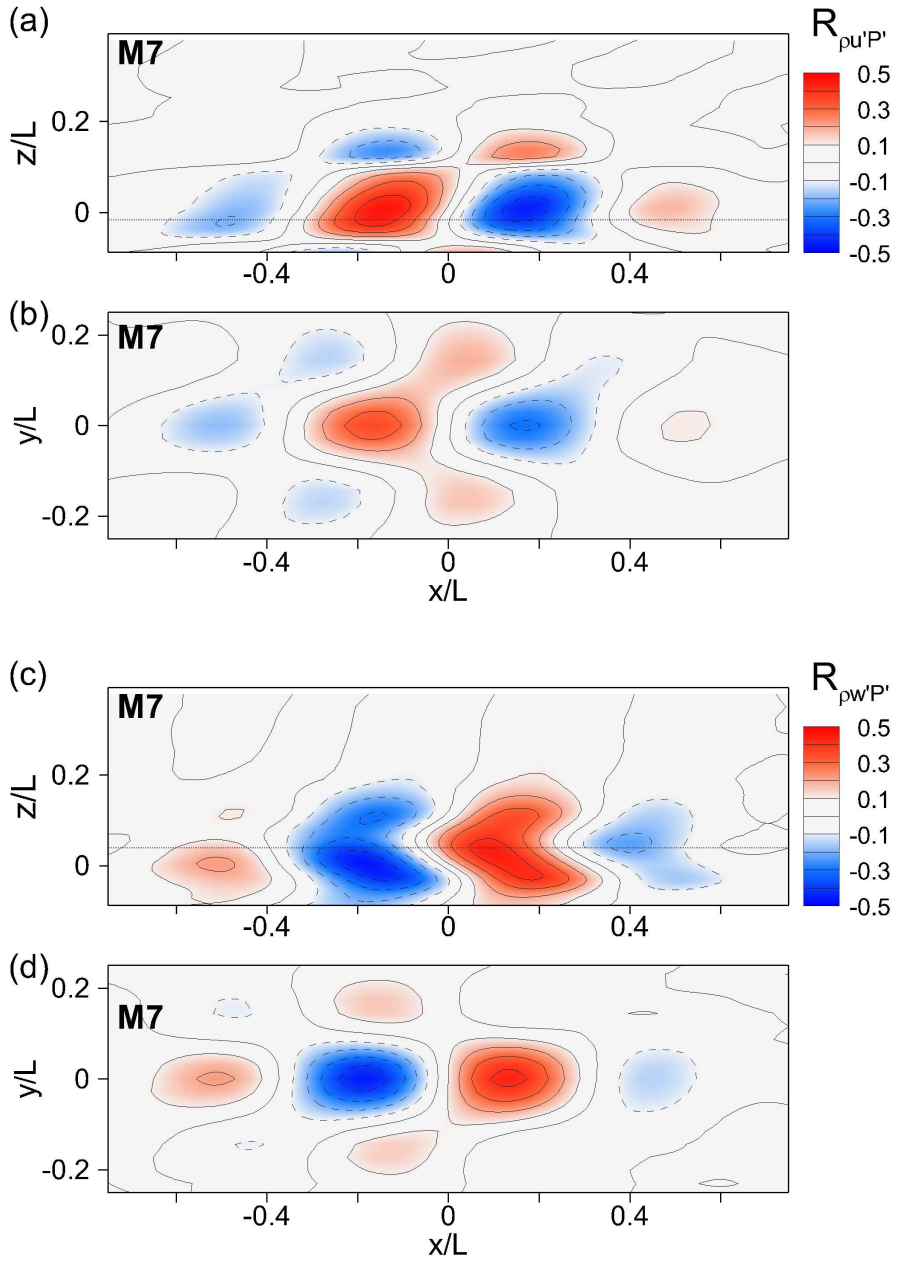

Figure 6.13: Enhanced correlation contours of the Mach 7 convective mixing layer structure. Correlations are of centerline pressure with longitudinal massflux in (a) xz- and (b) xy-planes and centerline pressure with cross-stream massflux in (c) xz- and (d) xy-planes. The horizontal dotted line in the xz-planes indicates the location of the corresponding xy-plane. Time correlations are converted to spatial information using the mixing layer convection velocity (i.e $x/L = tU_c/L$).

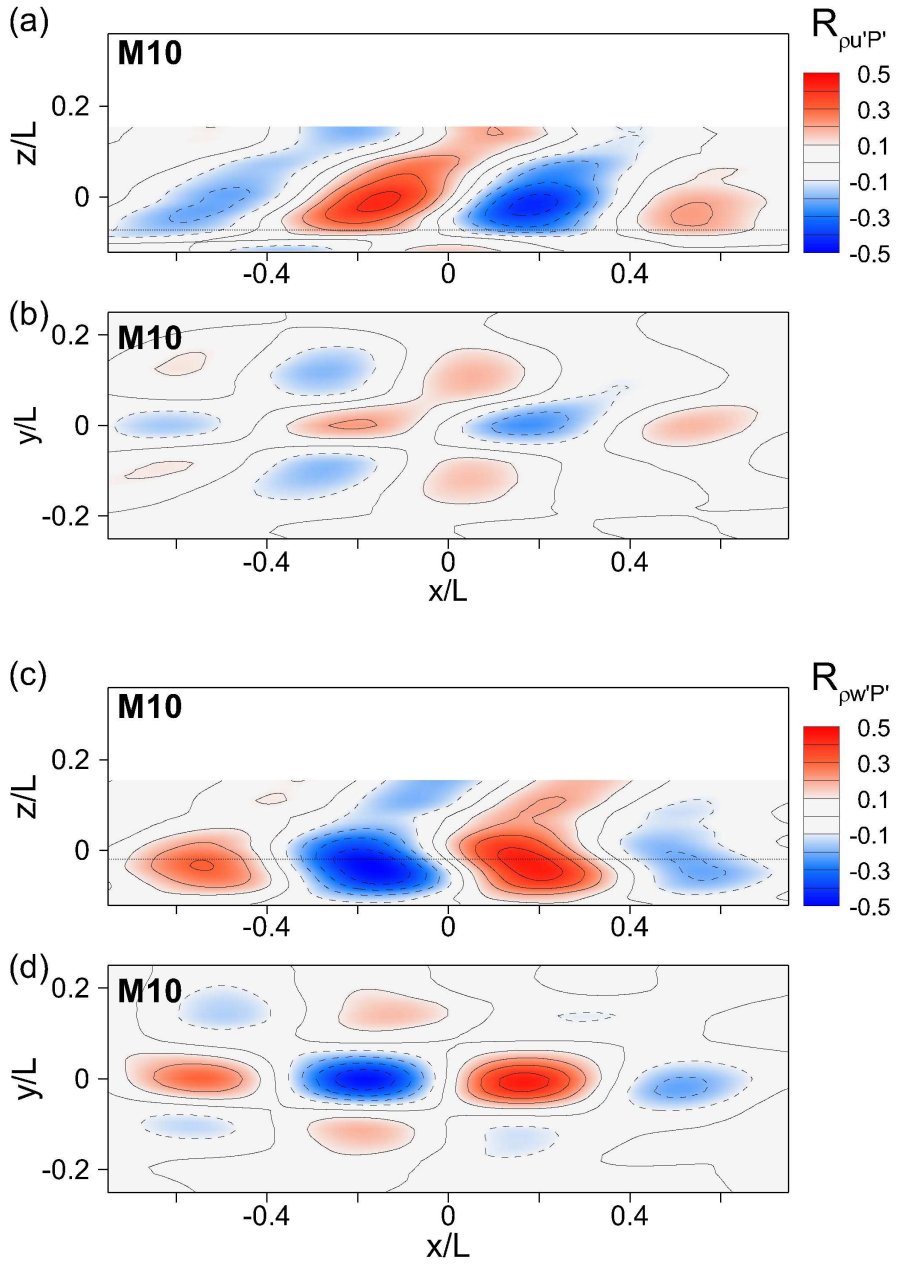

Figure 6.14: Enhanced correlation contours of the Mach 10 convective mixing layer structure. Correlations are of centerline pressure with longitudinal massflux in (a) xz- and (b) xy-planes and centerline pressure with cross-stream massflux in (c) xz- and (d) xy-planes. The horizontal dotted line in the xz-planes indicates the location of the corresponding xy-plane. Time correlations are converted to spatial information using the mixing layer convection velocity (i.e $x/L = tU_c/L$).

is along the mixing layer center line. Note that plotting the values of $R_{f'p'}$ along the line drawn in the xz-plane would result in the same 1D correlation curves as in Fig. 6.10 (d)-(f).

The form of the mixing layer vortices as determined from the two-dimensional (2D) correlation plots is a streamwise periodic structure that exists all through the cross-stream width of the mixing layer. In $R_{(\rho u)'p'}$, the sign of the periodic correlation is reversed in bands both above and below the mixing layer edges. These bands coincide with the position of the separation shock and the reverse flow respectively. In the xz-plane, the coherent structures are tilted "forward" in the correlations of streamwise mass flux and tilted "backwards" in the correlation of the cross-stream mass flux. The horizontal axis in Figs. 6.12, 6.13, and 6.14 is oriented so that positive Δx is "downstream" and negative Δx is "upstream". In the xy-plane, an obvious oblique pattern occurs and the mixing layer structures do not appear as 2D bands in the spanwise direction. This obliqueness in the average signature is consistent with compressible mixing layer research showing increased spanwise variation of the large mixing layer vortices with elevated convective Mach number [128, 129, 130, 131].

The interpretation of the correlation contour plots can be aided by considering the vector field defined by the magnitude of $R_{(\rho u)'p'}$ and $R_{(\rho w)'p'}$. Assuming that a negative fluctuation in pressure coincides with a vortex core, a plot of the vector field defined by $-(R_{(\rho u)'p'}, R_{(\rho w)'p'})$ will provide information on the average motion about a mixing layer vortex center. These are plotted in Fig. 6.15. Also plotted in Fig. 6.15 are the location of the mixing layer center line and the inclination angles of the iso-lines of zero correlation from Figs. 6.12-6.14. The point of crossing of the zero-correlation iso-lines can be interpreted as the center of the vortex. A similar correlation vector plot was

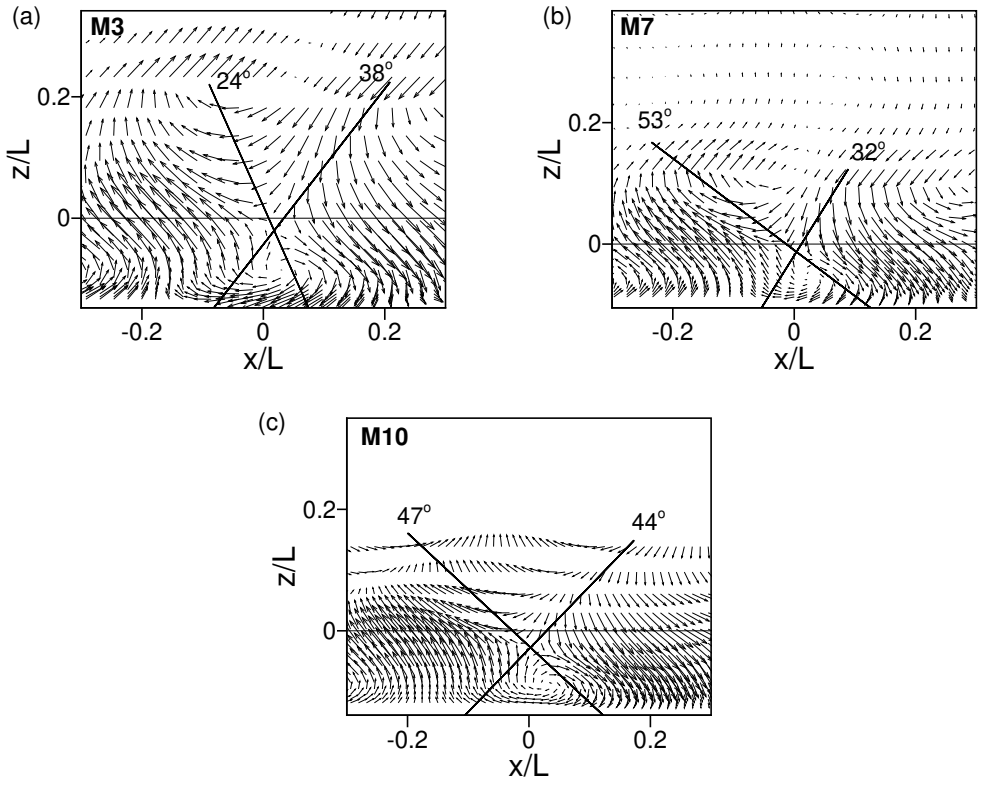

Figure 6.15: Vector fields of $-(R_{(\rho u)'p'}, R_{(\rho w)'p'})$ from Figs. 6.12-6.14 for (a) M3, (b) M7, and (c) M10. The vector field gives information on the averaged massflux motion about a negative fluctuation in pressure. The horizontal line indicates the location of the mixing layer center line. The inclination from vertical of the coherent structures as determined from the iso-line of zero correlation in $R_{(\rho u)'p'}$ and $R_{(\rho w)'p'}$ are also indicated.

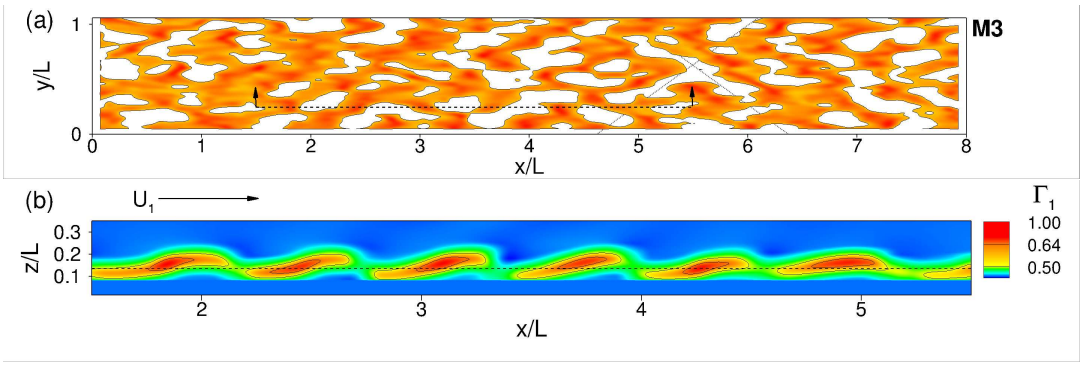

Figure 6.16: Contour of the vortex detector variable Γ_1 for the convective frozen flow from the corner grid plane of the Mach 3 flow. (a) The xy-plane sliced through the mixing layer center and (b) the xz-plane sliced through the section indicated by the dashed lines and arrows in (a). Dotted diagonal lines indicate the vortex angle predicted by equation 6.7.

used by Kiya & Sasaki [152] for an incompressible separation shear layer. Unlike in Kiya & Sasaki, no clear rotational motion is observed around the vortex center in Fig. 6.15. Instead, a saddle point occurs. The vector plot shows that the cross-stream momentum flux is positive to the left of the vortex core and negative to the right, as one would expect based on the (clockwise) orientation of the vortex roll-up. The vectors on the top and bottom of the vortex center, however, are in the opposite orientation from expected. The interpretation of this stems from the fact that the density in the low-speed side of the layer is a factor of two less than on the high speed side for the Mach 3 flow and a factor of four for the Mach 7 and 10 flows. The rotation of the vortex brings the low-momentum, low-density fluid into the high-speed, high-density side causing a negative streamwise correlation component to the left of the vortex center. The opposite occurs for fluid being pulled from the high-speed side into the low-speed side to the right of the vortex center.

Visualizations of the actual mixing layer vortices helps in asserting the interpretation of the enhanced correlation plots. Flow visualizations of individual mixing layer vortices in the raw data of the separated STBLI flows is made particularly difficult by the environment

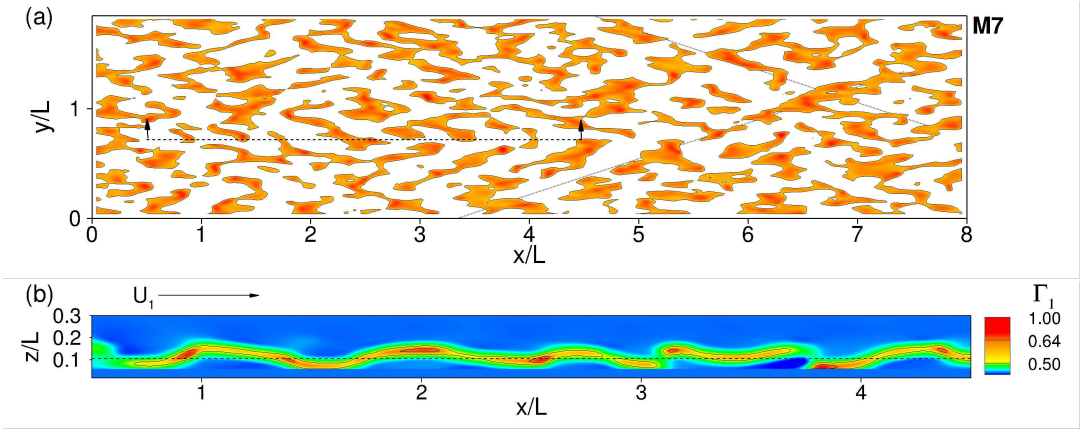

Figure 6.17: Contour of the vortex detector variable Γ_1 for the convective frozen flow from the corner grid plane of the Mach 7 flow. (a) The xy-plane sliced through the mixing layer center and (b) the xz-plane sliced through the section indicated by the dashed lines and arrows in (a). Dotted diagonal lines indicate the vortex angle predicted by equation 6.7.

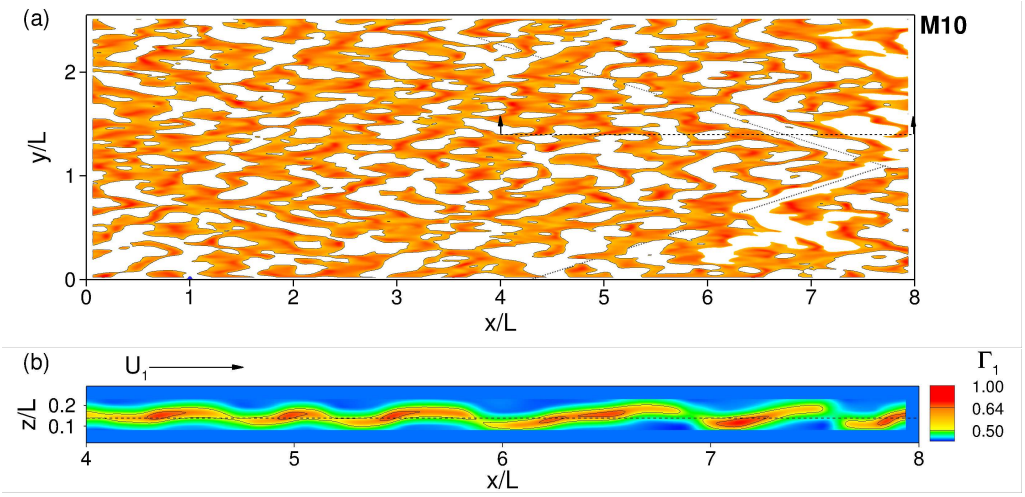

Figure 6.18: Contour of the vortex detector variable Γ_1 for the convective frozen flow from the corner grid plane of the Mach 10 flow. (a) The xy-plane sliced through the mixing layer center and (b) the xz-plane sliced through the section indicated by the dashed lines and arrows in (a). Dotted diagonal lines indicate the vortex angle predicted by equation 6.7.

in which they reside. One must be able to separate specifically the mixing layer rollers from (1) the smaller scale vortical hairpin vortices in the incoming boundary layer turbulence and (2) the separation shock which sits very close to the high speed side of the mixing layer as was shown in Fig. 6.1. We found that vortex detection methods based on the eigenvalues of the velocity divergence, such as swirl strength, were more problematic concerning the first issue. Vorticity methods, on the other hand, are dominated by the strong shear in the separation shock. Ultimately we found the method developed by Graftieaux *et al.* [155] to be the most robust for isolating the mixing layer vortices in the raw data. The Graftieaux method is based on the topology of the velocity field rather than on derivative quantities. It effectively searches the flow for points about which there is a net circulating motion and, because it uses a summation over a search window, it also acts as a spatial filter. This method was successively used by Dupont *et al.* [84] to identify mixing layer vortices in PIV data from their separated reflected shock STBLI experiments.

The Graftieaux method is a vortex search method in a 2D velocity vector field. If P is a point in the flow, S is a specified area surrounding P, and M is a point inside S, the vector detector Γ_1 is defined by

$$\Gamma_1(P) = \frac{1}{S}\int_{\boldsymbol{M}\in S} \frac{(\boldsymbol{PM}\times\boldsymbol{U_M})\cdot\boldsymbol{z}}{|\boldsymbol{PM}|\cdot|\boldsymbol{U_M}|}dS = \frac{1}{S}\int_S \sin\theta_{\boldsymbol{M}}dS \tag{6.5}$$

where $\boldsymbol{PM}$ is the vector connecting points P and M. The velocity vector at point $\boldsymbol{M}$ is $\boldsymbol{U_M}$ and θ is the angle between the vectors $\boldsymbol{PM}$ and $\boldsymbol{U_M}$. The parameter Γ_1 will take on values between -1 and 1 where the sign depends on the direction of rotation. It can be shown that a vortex exists at $\boldsymbol{P}$ if $|\Gamma_1| > 2/\pi$. For a square interrogation area with N

equally spaced discreet points inside the area S, equation 6.5 can be re-expressed as

$$\Gamma_1(P) = \frac{1}{S}\int_S \sin\theta_{\boldsymbol{M}} dS = \frac{1}{N}\sum_N \sin\theta_{\boldsymbol{M}}. \tag{6.6}$$

The band-pass filtered time signals of velocity from the corner profile of the ramp grids were again converted to space via the convection velocity of Section 6.5.2. Thus the 3D velocity field on which Γ_1 operates was generated. The 2D velocity vector $\boldsymbol{U_M}$ is defined as $(u - U_c, w)$ and the Graftieaux vortex detector was applied throughout the volume but always in the xz-plane. A square interrogation window of size $0.5\delta_{bl}$ was used throughout. The results are plotted in Figs. 6.16-6.18. The contour of Γ_1 in the streamwise-spanwise plane sliced along the mixing layer center ($\zeta = 0$) is plotted for a time segment equivalent to $8L$ in length that was randomly selected from the full time signal. This provides a top view of the instantaneous frozen mixing layer structures. In the inset of Figs. 6.16-6.18 (b) is shown a side view of the structures. The location in the span of the 3D volume of Γ_1 is indicated by the dashed line in the xy-plane contour. Similar plots are provided for arbitrarily selected time segments from the M3, M7, and M10 data.

From the top view, one can immediately observe the spanwise angular pattern in the vortices as is consistent with the 2D correlation plots of Figs. 6.12-6.14. From the top plan view, the M3 vortices are visually more coherent than the M7 and M10 flows. Also, in the side view, the M3 vortices appear more regular and resemble a sinusoidal wavy interface between the high and low-speed sides of the mixing layer. The vortex cores appear to occur predominantly at the up-slope of the wave. A similar pattern is seen in the xz-plane slice of the M7 and M10 flows although, in general, the M3 flow is apparently

more regular.

With regard to the spanwise oblique angle observed in both the enhanced correlation contours and the instantaneous vortex visualizations, it is interesting to consider the compressible mixing layer inviscid linear stability analysis by Sandham & Reynolds [131, 134]. These authors showed that an oblique unstable mode becomes dominant over the 2D mode for $M_c > 0.6$. Furthermore, they found that the angle α measured from the 2D mode increased with increasing M_c by

$$M_c \cos\alpha \approx 0.6. \tag{6.7}$$

For the current STBLI shear layers, $\alpha = 54^0$ for the M3 flow and 72^o for M7 and M10. These angles are indicated by the diagonal dotted lines drawn in the top-view contours of Γ_1 in Figs. 6.16-6.18 (a) and prove to be a close representation of the actual structure occurring in these flows.

6.6 Turbulence Scaling

Barre *et al.* [121] used dimensional analysis of the free shear layer to show that the maximum turbulence shear stress $-\langle u'w' \rangle_{\max}$ non-dimensionalized by $U_c(U_1 - U_2)$ varies linearly with the vorticity spreading rate. Specifically

$$\delta' = -\frac{1}{K} \frac{-\langle u'w' \rangle_{\max}}{U_c(U_1 - U_2)} \tag{6.8}$$

where K is a proportionality constant to be determined empirically. The derivation of this relation is independent of M_c and therefore includes both compressible and incompressible layers. Oftentimes equation 6.8 is tested using $U_{c,i}$ for lack of a better estimate, but, as

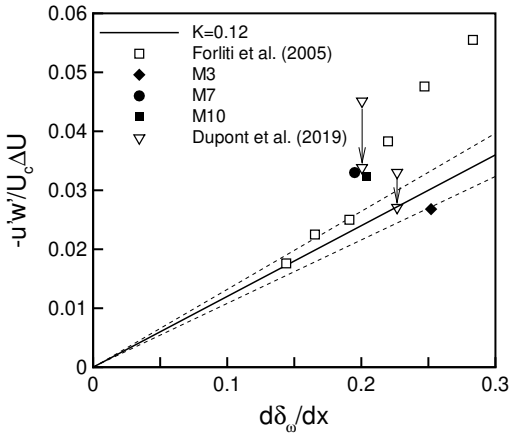

Figure 6.19: Non-dimensional turbulence stress versus the spreading rate. The arrows indicate how the data of Dupont *et al.* [143] changes if ΔU is calculated in the same manner as the current data.

was shown in Section 6.5.2, the actual convection velocity can vary significantly from the theoretical value.

In Fig. 6.19 is plotted the maximum turbulent stress from the profiles in Figs 6.2-6.4 (d) versus the average of the two estimates of spreading rate from table 6.2. The maximum turbulence shear stress and maximum normal stresses are listed in table 6.3. Included in Fig. 6.19 are also the data of the separated STBLI shear layer from the experiments of Dupont *et al.* [143], together with the subsonic counter-current mixing layer data of Forliti *et al.* [150]. It has been shown by Dupont *et al.* [143] using a large compilation of incompressible and compressible shear layer data available from literature that the majority of the co-flowing and single-stream data fall within reasonable error of $K = 0.12$. The line drawn in figure 19 correspond to this value of K. The dashed lines indicate the region of 10% error. The incompressible, counter-current data of Forliti *et al.* show that the turbulence shear stress follows the $K = 0.12$ line for spreading rates below approximately 0.2. Above 0.2, a steeper linear trend occurs. This bifurcation in the

Forliti data occurs between points of $r = -0.13$ and -0.19. Although the spreading rate is above 0.2, the Mach 3 data point with $r = -0.065$ follows the trend of the co-flowing data. The Mach 7 and Mach 10 data points, which have stronger reverse flow ($r = -0.123$ and -0.104) than the Mach 3, lie within the trend of the Forliti data at the same spreading rate. The two data points of Dupont *et al.* have similar velocity ratios ($r = -0.057$ and -0.146) as the present STBLI shear layers and show the same trend of the stronger reversed flow case having a higher non-dimensionalized turbulent shear stress.

The difference between the data of Dupont *et al.* and the current data may be related to the method of determining U_1 and U_2. Dupont *et al.* selected these values from a ζ closer to the mixing layer center thus possibly under-predicting ΔU. If the method of Section 6.4.2 is used to recalculate ΔU of Dupont *et al.*, the two data points move much closer to the current data as indicated by the arrows in Fig. 6.19. This is an intriguing result and suggests that the change in the nature of the shear layer instability for counter-current mixing layers as described by Forliti *et al. et al.* [150] is independent of the level of compressibility.

The Reynolds stress stress anisotropy $\langle w'^2 \rangle / \langle u'^2 \rangle$ is known to be typically around 0.5 for incompressible shear layers and can decrease significantly for M_c above approximately 0.5 [1, 143]. Brown & Roshko [156] used dimensional analysis to propose that the Reynolds stress anisotropy decreases in proportion to $1/M_c^2$. The anisotropy determined from the profiles of Figs. 6.2-6.4 are listed in table 6.3 and are found to lie below the subsonic level of 0.5. The anisotropy of the M7 and M10 data are almost half that of the M3, confirming that the anisotropy decreases significantly with M_c for the STBLI shear layer although not the the extent predicted by the $1/M_c^2$ scaling. The anisotropy at $M_c = 2$ would be approximately 0.083 if calculated by the $1/M_c^2$ law in relation to the anisotropy level of

Case	$-\langle u'w'\rangle/U_c\Delta U$	$\langle u'^2\rangle/\Delta U$	$\langle w'^2\rangle/\Delta U$	$\langle w'^2\rangle/\langle u'^2\rangle$
M3	0.0268	0.0432	0.0108	0.250
M7	0.0330	0.0754	0.0117	0.155
M10	0.0323	0.0786	0.0131	0.167

Table 6.3: Reynolds stresses and anisotropy.

the M3 flow. We note that Forliti *et al.* [150] found that increasing the strength of the counter-current reverse flow increased $\langle w'^2\rangle/\langle u'^2\rangle$ only for $r \leq -0.2$.

The reduction in STBLI shear layer anisotropy is primarily due to an increase in the streamwise turbulence component while the cross-stream component increases only slightly. Values for the cross-stream stress of the M3 shear layer are comparable to the levels experienced in canonical mixing layers near $M_c = 1$. The increase in streamwise turbulence stress from $M_c = 1$ to $M_c = 2$ is opposite to the apparent trends in canonical mixing layer data for which $\langle u'^2\rangle/\Delta U$ is found to decrease or remain constant with increasing M_c. For example, see the data compilations of Barre & Bonnet [126] or Pantano & Sarkar [123] although the data do not extend past $M_c = 1.2$. To make sense of these differences, we turn to the analysis of the turbulent kinetic energy and Reynolds stress budget equations (Appendix A).

Pantano & Sarkar [123] showed in the DNS of temporal mixing layers from $M_c = 0.3$ to 1.1 that the normalized TKE production and transport decreased with increasing M_c while dissipation remained constant. Similar results were obtained by Vreman *et al.* [137] and by Freund *et al.* [125]. Decreased production resulted in decreased TKE thus reducing turbulence mixing and ultimately the spreading rate. Increasing M_c also has the effect of significantly decreasing the pressure-strain rate components in relation to the incompressible values [123]. The pressure-strain terms are primarily responsible for the transfer of turbulence energy from the streamwise direction to the cross-stream direction

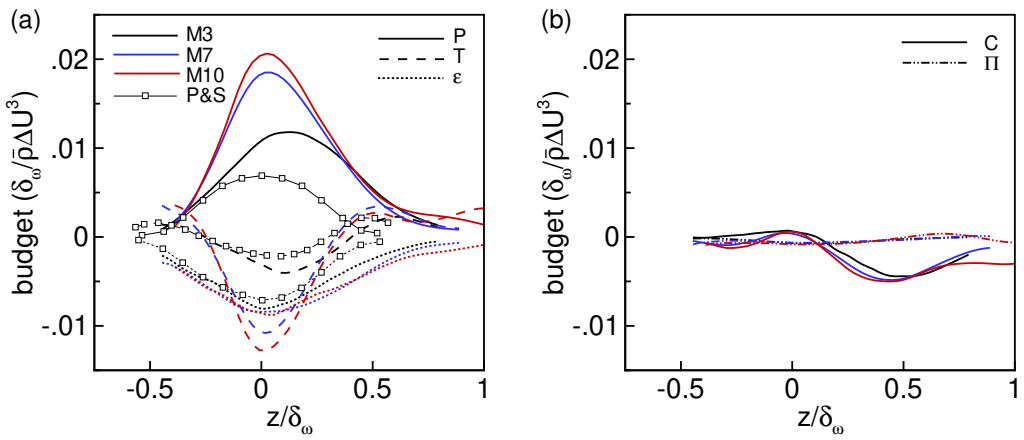

Figure 6.20: Turbulent kinetic energy budgets: Production, transport, and dissipation are plotted in (a), and convection and pressure strain in (b).

as it provides the greatest negative (loss) term in R_{11} and the dominant positive (gain) term in the budgets of R_{33} and $-R_{13}$.

The TKE budgets of the three STBLI shear layers are shown in Fig. 6.20. The Reynolds stress budgets are shown in Fig. 6.21. The budget profiles are plotted as functions of $z/\delta_\omega = \zeta/(d\delta_\omega/dx)$ and were averaged in the x-direction over the region of approximate similarity defined in Section 6.4.1. All budget terms are nearly symmetric with the exception of the convection profiles which are found to be affected by the proximity of the wall on the low-speed side. The asymmetry of the convection term is responsible for the shift in the turbulence peak noted in Section 6.4.1. The level of convection does not change between the three cases and so its influence in shifting the turbulence peak is greatest for the M3 case with the lowest TKE production. The TKE production and transport increase substantially with increasing Mach number. The same is true for the R_{11} budgets. Production and transport are approximately constant across the three cases for R_{33} and increase in magnitude only slightly for R_{13}. The observed increase across cases in $\mathcal{T}_{13}$ and $\mathcal{T}_{33}$ is due to an increase in the pressure diffusion. The increase in $\mathcal{T}_{11}$,

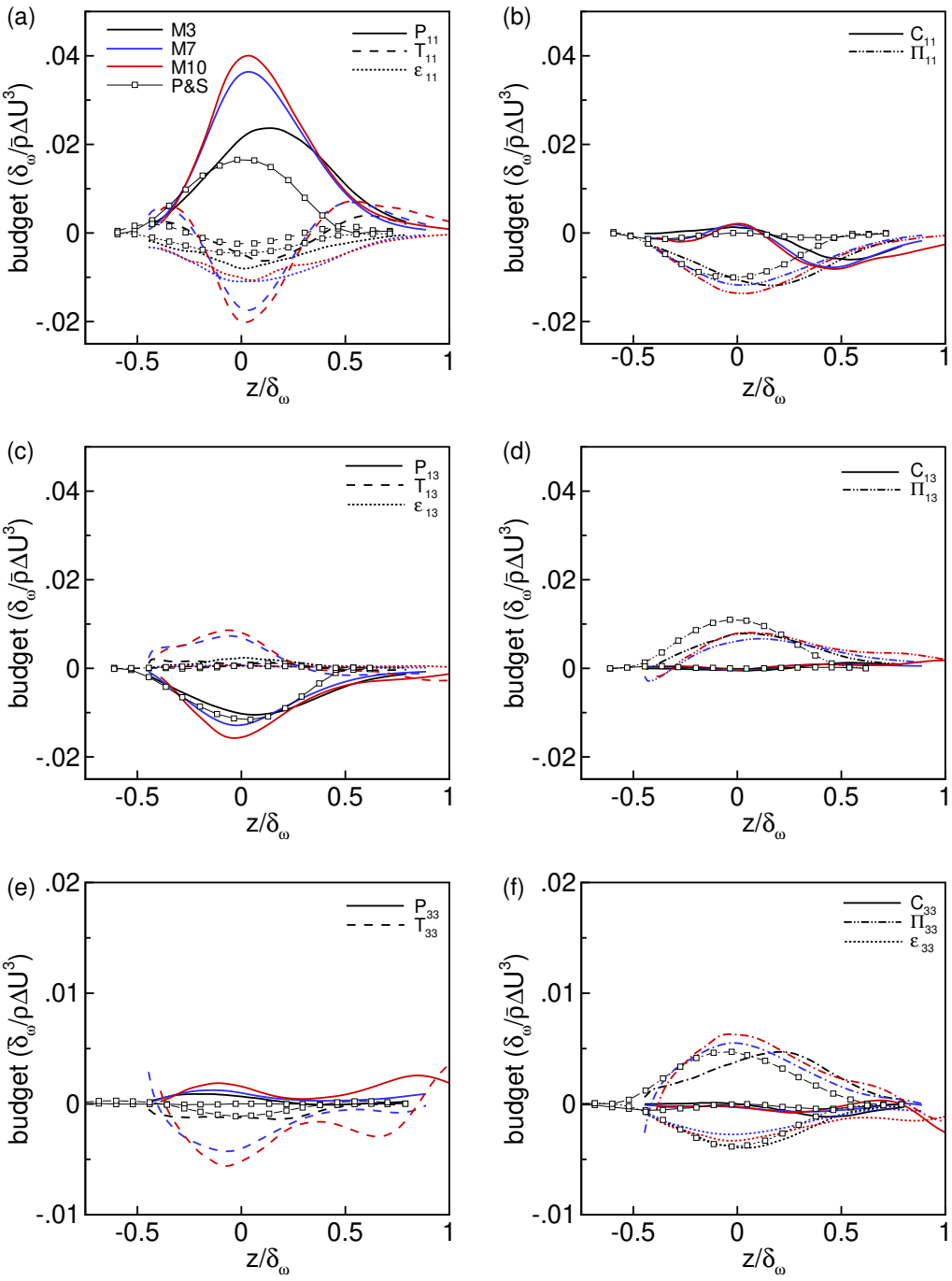

Figure 6.21: Reynolds stress budgets of R_{11} (a)-(b), R_{13} (c)-(d), and R_{33}.

however, is due entirely to increased turbulence transport as the pressure diffusion remains negligible in all three cases for this budget. Not included in these plots is the pressure work terms Σ and Σ_{ij}, which are negligible for all cases.

The data of Pantano & Sarkar [123] for $M_c = 1.1$ and $s = 1$ are included in Figs. 6.20 and 6.21 for comparison. For this purpose, the data of Pantano & Sarkar was rescaled from the normalization by the mixing layer momentum thickness δ_θ to the vorticity thickness δ_ω. The ratio $\delta_\theta/\delta_\omega$ for this data was obtained by noting that, for a planar mixing layer, $\mathcal{P}\delta_\omega/\langle\rho\rangle\Delta U^3 = \frac{1}{2}(\mathcal{P}_{11}\delta_\omega/\langle\rho\rangle\Delta U^3) = -\widetilde{u''w''}/\Delta U^2$. It is obvious that the STBLI shear layers have much higher production and transport rates of TKE and R_{11} than the canonical case. Otherwise, all other budget terms of the M3 shear layer at $M_c = 1$ compare exceptionally well with the data of Pantano & Sarkar, most notably in the pressure-strain terms.

Freund *et al.* [125] studied the TKE and Reynolds stress budgets for self-similar annular jets at M_c from 0.1 to 1.8 and found that the ratios between the integrated pressure-strain terms (Π_{11}/Π_{33}) and also the ratio of integrated pressure-strain components to turbulent shear stress production ($\Pi_{ij}/\mathcal{P}_{13}$) were nearly constant with M_c. The STBLI Π_{ij} and $\mathcal{P}_{13}$ budget profiles were integrated over z/δ_ω and the various ratios were calculated. These are listed in Table 6.4 and the results are compared to the M_c-independent ratios reported by Freund *et al.* [125]. The closeness between the STBLI shear layer ratios and those of Freund *et al.* indicates that the interchange of turbulence energy is very similar between the two configurations.

From the comparison with the budgets of Pantano & Sarkar and with the ratios of integrated budgets of Freund *et al.*, it is apparent that the most significant difference between the separation shear layer and the canonical case is the greatly increased turbu-

Case	Π_{33}/Π_{11}	$\Pi_{11}/\mathcal{P}_{13}$	$\Pi_{33}/\mathcal{P}_{13}$	$\Pi_{13}/\mathcal{P}_{13}$
M3	0.38	1.17	0.45	0.70
M7	0.41	1.12	0.46	0.69
M10	0.40	1.01	0.40	0.74
Freund *et al.* (2000)	0.4	1.0	0.4	0.8

Table 6.4: Comparison of integrated Reynolds stress pressure-strain budgets.

lence production of the separation shear layer. There is more energy in the higher Mach number STBLI flows and therefore more energy is transferred from the mean flow to the turbulence, predominantly through the R_{11} production, but the rate at which the energy is transferred from streamwise to the spanwise component is limited by the pressure-strain rate terms. Both the viscous drain of turbulence energy as well as the transport between the components of turbulence by the pressure strain terms have been shown to be similar to the canonical data suggesting that these properties in the STBLI shear layer are affected by compressibility in the same manner as for the canonical free mixing layer.

6.7 Summary and Conclusions

The results presented in this chapter effectively demonstrate that, even in this assertively non-canonical configuration that is the shear layer in a separated STBLI flow, it is still possible to define a region of approximate mixing layer-like similarity. Perhaps more surprising is the fact that the STBLI shear layer also shows striking consistency with canonical mixing layer theories as they are currently understood. This fact remains even in the case of the hypersonic separation for which the shear layer high speed Mach number is above 5 and the temperature ratio across the layer is also above 5.

Concerning the environment in which the shear layers exist, certain factors that prevent this flow from being canonical in nature are the fact that the shear layer is (1)

embedded in a turbulent boundary layer, (2) is subjected to the low-frequency oscillations of the separation shock unsteadiness, (3) is not aligned with the freestream, and (4) the low-speed side of the layer is produced by the reverse flow of a shallow separation bubble. In spite of these, we have demonstrated the possibility to obtain a reasonable collapse of the mean flow profiles and turbulence stress profiles when plotting against a linearly varying similarity variable. This is consistent with a constant spreading rate. The form of the similarity profiles of U and the Reynolds stresses are also reminiscent of canonical mixing layer topology and exhibit the necessary conditions for the Kelvin-Helmholtz instability. Properties of the shear layers were reported, including the estimated conditions of the two streams, the convective Mach number, the estimated linear spreading rates, and maximum turbulence stress levels. The peak turbulence shear stress was found to be proportional to the spreading rate by the same relation as for canonical mixing layer data with no dependence on the level of compressibility. Variation of the STBLI shear layer properties with convective Mach number were shown to be consistent with known trends observed in the literature. With respect to the variation of mixing layer properties with increased compressibility as classified by M_c, the data is in the direction of the expected trends. The difference in properties of the M7 and M10 data cases at $M_c = 2$ is consistent with an increase in M_c when compared to M3 at $M_c = 1$. Namely, a decrease in spreading rate with M_c was observed and the extent of this decrease, although not to the level of the classic Langley curve, is consistent with other noted properties of the STBLI shear layers that could also affect the spreading rate, specifically, the elevated reverse flow and the adverse pressure gradient. A decrease in turbulence anisotropy was also observed with increasing M_c. The well-documented increase in three-dimensionality of the vortex rollers with increasing M_c was also shown in the current data. A sophisticated conditional av-

eraging method of the two-point correlations was developed for the purpose of extracting specifically the mixing layer vortex signatures from the turbulent environment. This correlation method also allowed for the direct measurement of the mixing layer convection velocity. Instantaneous visualizations of the vortices showed that the oblique angle of the vortices in the spanwise direction is consistent with predictions by inviscid linear stability theory based on M_c.

It was found through turbulent kinetic energy and Reynolds stress budget analysis that the STBLI shear layers have a much greater streamwise turbulence production rate than what is observed in compressible mixing layer data. In spite of this difference, the interchange of turbulence energy among the different turbulence stress components determined from the pressure-strain rate terms was shown to be consistent with mixing layer data at the same M_c. The drain of energy caused by the viscous terms were also consistent. These results inidicate that the STBLI shear layer spreading rate, turbulence shear stress, and anisotropy are dictated by the same compressible flow phenomena as in the canonical configuration.

Mixing layer conditions that are particularly difficult to set up experimentally occur naturally in the STBLI shear layer: high M_c, high reverse flow, and also an adverse pressure gradient. Although it has its limitations as pointed out above, the STBLI shear layer configuration, as demonstrated by this study, can provide useful data capable of expanding the currently available mixing layer condition parameter space, as well as identify accurate generalizations of compressible shear layers for the development of turbulence models and scaling laws. In particular, the conservative energy exchange from the streamwise component is less efficient with increasing M_c thus causing both the spreading rate and the anisotropy to decrease with increasing M_c.

Chapter 7: Summary and Conclusions

Given the current status of hypersonic STBLI research and the complex nature of these flows, there is an undeniable need for high-fidelity numerical simulations of the canonical configurations. Such data can provide a great amount of detail in the flow turbulence, both in three-dimensional space and in time, allowing for sophisticated analysis of the flow physics.

High-fidelity simulations can be achieved either with DNS or LES techniques. The LES technique solves the filtered equations for the conservation of mass, momentum, and energy for which the smallest turbulence scales, which are assumed to be nearly isotropic, are modeled. Because only the smallest scales are modeled, the LES still produces highly detailed flow fields, but the reduction in the computational cost is significant. As shown by the results presented in this thesis, the savings in the LES grid size is approximately 95%-97% of the DNS grid and the LES timestep is typically 3 times that of the DNS. With regard to the STBLI flow, this difference makes both the ability to spectrally converge the low-frequency unsteadiness and the ability to match experimental Reynolds numbers feasible. The necessity of having both experimental data and numerical data at the same conditions has been emphasized in the literature [1, 10, 29, 30].

The application of LES at hypersonic conditions is currently an emerging technology. Only a few attempts have been made so far to simulate STBLI above Mach number of 5. Three attempts are known to the authors and all three are of a Mach 7, 33^o compression

ramp/expansion corner flow. Two were by Schreyer *et al.* [45] and Kim *et al.* [46] and both used an eddy viscosity model for the SGS closure. The third was by Ritos *et al.* [49] who used an implicit LES method where the SGS contribution results from the numerical dissipation properties of the implicit scheme. Significant errors were found in comparison to the available data although the accuracy of the experimental data is not certain.

In the current work, we have demonstrated that our LES technique which uses the dynamic mixed model of Martin *et al.* [52], produces accurate results for STBLI flow including hypersonic conditions. An important conclusion from this work is that, for separated hypersonic STBLI, using an eddy viscosity model for the closure of the shear stress and heat flux terms results in large errors in the separation length and in the spreading rate of the separation shear layer. The error in separation length was also observed in the Mach 3 separated interaction but to a lesser extent.

New LES data of two compression-ramp generated, fully-separated hypersonic STBLI at Mach 7 and Mach 10 were presented and the mean flow statistics were documented. These provide a unique contribution to the available database of hypersonic STBLI, and of particular importance is the reporting of the turbulence data and the wall heat transfer.

Besides the very useful but straight forward documentation of averaged flow properties, these datasets were used in the present work for three specific data analysis projects that have provided insight into several key features of the hypersonic STBLI flow field. These include the analysis of Chapter 4 in which the low-pass filtering operation on the full volume data and in time revealed the form of the low-frequency unstable mode in the hypersonic interaction. The resulting flow visualizations and videos provided essential information in developing the physical model for the separation unsteadiness presented in Chapter 4. The origins of the low-frequency mode in separated STBLI flows has been a

topic of much debate for over five decades [1, 10].

In Chapter 5 was presented for the first time a compilation of hypersonic STBLI separation length and shock strength data from the literature. This compilation also included the new LES data produced from this work at Mach 7 and Mach 10 over a range of compression angles producing a substantial range of both separation length and shock strength data. This enabled the derivation and evaluation of a modified separation length scaling based on that of Souverein *et al.* [14]. The results gave strong evidence that incipiently separated STBLI scale on the incoming boundary layer dynamic pressure and skin friction. The scaling was found to be generic to STBLI of compression ramps, reflected shocks, and axi-symmetric cylinder-with-flare from supersonic to hypersonic conditions with adiabatic, heated, and cold walls. The fully separated regime did not show such a collapse, however, the insights provided by the low-frequency mode study of Chapter 4 could be used for further investigation of this topic in the future.

And lastly, the analysis of the separation shear layer presented in Chapter 6 provided unique insight into the nature of the separation in STBLI as well as the behavior of compressible turbulence in free shear layers. It was shown that the separation shear layer naturally occurs at high convective Mach numbers at and above 1. The Mach 7 and Mach 10 separated flows resulted in convective Mach number of approximately 2. A sophisticated enhanced correlation method was developed to identify the mixing layer-like, spanwise-oriented vortices. By this method it was possible to determine the time scale, averaged three-dimensional form, convection velocity, and instantaneous structure of the vortices. The convection velocity is a particularly useful quantity for the study of mixing layer data but is difficult to determine experimentally [1]. Many scaling relations, such as the spreading rate to turbulence stress, rely on an accurate measurement of convection velocity

and the theoretical value derived from isentropic processes is typically not accurate at high convective Mach number [1]. In particular, it was discovered that the change in turbulence dissipation and pressure-strain rate with convective Mach number was consistent with compressible free mixing layer data. The greater turbulence production in the STBLI shear layers was found to be consistent with greater spreading rate and turbulence stress by compressible mixing layer relations.

Looking forward from the work included in this thesis, topics of interest include the investigation of a separation length scaling for the fully separated case. Most likely this would require the development of a method of quantitative characterization of the low-frequency mode in order to study the dependence of the mode on Reynolds number, Mach number, wall temperature and so on. It would be interesting to explicitly show the flow dynamics in the STBLI data consistent with the low-frequency unsteadiness model discussed in Chapter 4. In addition, all simulations presented here are low enthalpy and non-reacting. For the design of hypersonic vehicles, real gas effects at flight conditions are of interest.

Appendix A: Turbulent Kinetic Energy and Reynolds Stress Budget Equations

The transport equation for the turbulent kinetic energy defined as $k = \langle \rho u_i'' u_i'' \rangle / 2$ can be written as the following.

$$
\begin{aligned}
&\frac{\partial k}{\partial t} = 0 = \mathcal{C} + \mathcal{P} + \mathcal{T} + \Pi + \epsilon + \Sigma, \\
&\mathcal{C} = -\frac{\partial k \tilde{u}_j}{\partial x_i}, \\
&\mathcal{P} = -\langle \rho u_i'' u_j'' \rangle \frac{\partial \tilde{u}_i}{\partial x_j}, \\
&\mathcal{T} = -\frac{1}{2}\frac{\partial \langle \rho u_i''^2 u_j'' \rangle}{\partial x_j} - \frac{\partial \langle p' u_i'' \rangle}{\partial x_i} + \left(\frac{\partial \langle u_i'' \sigma_{ij} \rangle}{\partial x_j} + \frac{\partial \langle u_i'' \tau_{ij} \rangle}{\partial x_j} \right), \\
&\Pi = \left\langle p' \frac{\partial u_i''}{\partial x_i} \right\rangle, \\
&\epsilon = -\left\langle \sigma_{ij} \frac{\partial u_i''}{\partial x_j} \right\rangle - \left\langle \tau_{ij} \frac{\partial u_i''}{\partial x_j} \right\rangle, \\
&\Sigma = -\langle u_i'' \rangle \frac{\partial \langle p \rangle}{\partial x_i}.
\end{aligned}
\tag{A.1}
$$

The Reynolds average is indicated by the angled brackets, a fluctuation about the Reynolds average is indicated by the single prime (e.g. $u = \langle u \rangle + u'$). The Favre average is denoted by the tilde such that $\tilde{u} = \langle \rho u \rangle / \langle \rho \rangle$ and a fluctuation about the Favre average is indicated by the double prime (e.g. $u = \tilde{u} + u''$). The individual budget terms in Eqn. A.1 are the convection $\mathcal{C}$, production $\mathcal{P}$, transport $\mathcal{T}$, pressure strain Π, dissipation ϵ, and pressure work Σ. The three contributions to the transport term are, in order from left to right, the turbulence transport, pressure diffusion, and viscous diffusion. Both the viscous

diffusion and the viscous dissipation are functions of the shear stress tensor, which for an LES solution, includes both the resolved stress σ_{ij} and the unresolved SGS stress τ_{ij}.

Similarly, the Favre fluctuation Reynolds stress budget equation can be written as the following where $R_{ij} = \langle \rho u_i'' u_j'' \rangle$.

$$
\begin{aligned}
&\frac{\partial R_{ij}}{\partial t} = 0 = \mathcal{C}_{ij} + \mathcal{P}_{ij} + \mathcal{T}_{ij} + \Pi_{ij} + \epsilon_{ij} + \Sigma_{ij}, \\
&\mathcal{C}_{ij} = -\frac{\partial R_{ij} \tilde{u}_k}{\partial x_k}, \\
&\mathcal{T}_{ij} = -\frac{\partial \langle \rho u_i'' u_j'' u_k'' \rangle}{\partial x_k} + \frac{\partial \langle p' u_i'' \rangle}{\partial x_k} + \left(\frac{\partial \langle \sigma_{jk} u_j'' \rangle}{\partial x_k} + \frac{\partial \langle \sigma_{ik} u_j'' \rangle}{\partial x_k} + \frac{\partial \langle \tau_{jk} u_j'' \rangle}{\partial x_k} + \frac{\partial \langle \tau_{ik} u_j'' \rangle}{\partial x_k} \right), \\
&\Pi_{ij} = \left\langle p' \frac{\partial u_i''}{\partial x_j} \right\rangle + \left\langle p' \frac{\partial u_j''}{\partial x_i} \right\rangle, \\
&\epsilon_{ij} = -\left\langle \sigma_{jk} \frac{\partial u_i''}{\partial x_k} \right\rangle - \left\langle \sigma_{ik} \frac{\partial u_j''}{\partial x_k} \right\rangle - \left\langle \tau_{jk} \frac{\partial u_i''}{\partial x_k} \right\rangle - \left\langle \tau_{ik} \frac{\partial u_j''}{\partial x_k} \right\rangle, \\
&\Sigma_{ij} = -\langle u_j'' \rangle \frac{\partial \langle p \rangle}{\partial x_i} - \langle u_i'' \rangle \frac{\partial \langle p \rangle}{\partial x_j}.
\end{aligned}
\tag{A.2}
$$

Bibliography

[1] Smits, A. J. and Dussauge, J. P., *Turbulent Shear Layers in Supersonic Flow*, 2nd edn. Springer, 2006.

[2] Dussauge, J. P., Dupont, P., and Debiève, J. F., "Unsteadiness in shock wave boundary layer interaction with separation," *Aeros. Sci. Technol.*, Vol. 10, 2006, pp. 85–91.

[3] Wu, M. and Martín, M. P., "Analysis of shock motion in shockwave and turbulent boundary layer interaction using direct numerical simulation data," *J. Fluid Mech.*, Vol. 594, 2008, pp. 71–83.

[4] Bertin, J. and Cummings, R., "Fifty years of Hypersonics: Where We've Been, Where We're Going," *Progress in Aerospace Sciences*, Vol. 26, 2013, pp. 216–234.

[5] Kostoff, R. and Cummings, R., "Highly cited literature of high speed compressible flow research," *Aerospace Science and Technology*, Vol. 26, 2013, pp. 216–234.

[6] Leyva, I., "The relentless pursuit of hypersonic flight," *Physics Today*, Vol. 70, No. 11, 2017, pp. 31–36.

[7] Gnoffo, P. A., Berry, S. A., and Norman, J. W. V., "Uncertainty assessments of 2D and axisymmetric hypersonic shock wave - turbulent boundary layer interaction simulations at compression corners," *AIAA paper 2011-3142*, 2011.

[8] Roy, C. J. and Blottner, F. G., "Review and assessment of turbulence models for hypersonic flows," *Progress in Aerospace Sciences*, Vol. 42, 2006, pp. 469–530.

[9] Schülein, E., "Skin-friction and heat flux measurements in shock/boundary-layer inter action flows," *AIAA J.*, Vol. 44, No. 8, 2006, pp. 1732–1741.

[10] Gaitonde, D. V., "Progress in shock wave/boundary layer interactions," *Prog. in Aerosp. Sci.*, Vol. 72, No. 80, 2015.

[11] Dupont, P., Haddad, C., and Debiève, J. F., "Space and time organization in a shock-induced separated boundary layer," *J. Fluid Mech.*, Vol. 559, 2006, pp. 255–277.

[12] Priebe, S. and Martín, M. P., "Low-frequency unsteadiness in shock wave-turbulent boundary layer interaction," *Journal of Fluid Mechanics*, Vol. 699, 2012, pp. 1–49.

[13] Dolling, D. S. and Dussauge, J. P., "Fluctuating wall pressure measurements," *AGARDograph 315*, 1989.

[14] Souverein, L. J., Bakker, P. G., and Dupont, P., "A scaling analysis for turbulent shock-wave/boundary-layer interactions," *Journal of Fluid Mechanics*, Vol. 714, 2013, pp. 505–535.

[15] Jaunet, V., Debieve, J. F., and Dupont, P., "Length Scales and Time Scales of a Heated Shock-Wave/Boundary-Layer Interaction," *AIAA Journal*, Vol. 52, No. 11, November 2014.

[16] Beresh, S. J., Clemens, N. T., and Dolling, D., "Relationship between upstream turbulent boundary-layer velocity fluctu ations and separation shock unsteadiness," *AIAA Journal*, Vol. 40, No. 12, 2002, pp. 2412–2422.

[17] Ganapathisubramani, B., Clemens, N. T., and Dolling, D. S., "Low-frequency dynamics of shock-induced separation in a compression ramp interaction," *Journal of Fluid Mechanics*, Vol. 636, 2009, pp. 397–425.

[18] Humble, R. A., Elsinga, G. E., Scarano, F., and van Oudheusden, B. W., "Three-dimensional instantaneous structure of a shock wave/turbulent boundary layer interaction," *Journal of Fluid Mechanics*, Vol. 622, 2009, pp. 33–62.

[19] Erengil, M. E. and Dolling, D. S., "Unsteady wave structure near separation in a Mach 5 compression ramp interaction," *AIAA Journal*, Vol. 29, No. 5, 1991, pp. 728–735.

[20] Thomas, F. O., Putnam, C. M., and Cho, M. C., "On the mechanism of unsteady shock oscillation in shock wave/turbulent boundary layer interactions," *Experiments in Fluids*, Vol. 18, No. 1–2, 1994, pp. 69–81.

[21] Piponniau, S., Dussauge, J. P., Debiève, J. F., and Dupont, P., "A simple model for low-frequency unsteadiness in shock-induced separation," *J. Fluid Mech.*, Vol. 629, 2009, pp. 87–108.

[22] Priebe, S., Tu, J. H., Rowley, C. W., and Martin, M. P., "Low-frequency dynamics in a shock-induced separated flow," *Journal of Fluid Mechanics*, Vol. 807, 2016, pp. 441–477.

[23] Martín, M. P., Priebe, S., and Helm, C. M., "Upstream and Downstream Influence on STBLI Instability," *AIAA Paper No. 2016-3341*, 2016.

[24] Martín, M. P. and Helm, C. M., "The role of inviscid centrifugal instability vortices in shock-separated boundary layers," *Under consideration for publication in Theor. and Comp. Fluid Dyn.*, 2021.

[25] Hildebrand, N., Dwivedi, A., Nichols, J. W., Javonović, M. R., and Candler, G. V., "Simulation and stability analysis of oblique shock-wave/boundary-layer interactions at Mach 5.92," *Physical Review Fluids*, Vol. 3, No. 013906, 2018.

[26] Wu, Y., Yi, S., He, L., Chen, Z., and Wang, X., "Experimental Investigations of Supersonic Flow Over a Compression Ramp Based on Nanoparticle-Tracer-Based Plane Laser Scattering Technique," *Exp. Techniques*, 2015, pp. 651–660.

[27] Elfstrom, G. M., "Turbulent hypersonic flow at a wedge-compression corner," *Journal of Fluid Mechanics*, Vol. 53, 1972, pp. 113–127.

[28] Knight, D., Chazot, O., Austin, J., Badr, M. A., Candler, G., Celik, B., de Rosa, D., Donelli, R., Komives, J., Lani, A., Levin, D., Nompelis, I., Panesi, M., Pezzella, G., Reimann, B., Tumuklu, O., and Yuceli, K., "Assessment of predictive capabilities for aerodynamic heating in hypersonic flow." *Prog. in Aerosp. Sci.*, Vol. 90, 2017, pp. 39–53.

[29] Holden, M. S. and Moselle, J. R., "A Database of Aerothermal Measurements in Hypersonic Flow for CFD Validation," *AIAA Paper No. 92-4023*, 1992.

[30] Holden, M. S., Moselle, J. R., Sweet, S. J., and Martin, S. C., "A Database of Aerothermal Measurements in Hypersonic Flow for CFD Validation," *AIAA Paper No. 96-4597*, 1996.

[31] Settles, G. S. and Dodson, L. J., "Hypersonic shock/boundary-layer interaction database," *Tech. Rep. CR-177577 NASA*, 1991.

[32] Settles, G. S. and Dodson, L. J., "Hypersonic shock/boundary-layer interaction database: New and corrected data," *Tech. Rep. CR-177577 NASA*, 1994.

[33] Settles, G. S. and Dodson, L. J., "Supersonic and hypersonic shock/boundary-layer interaction database," *AIAA J.*, Vol. 32, No. 7, 1994, pp. 1377–1383.

[34] Priebe, S. and Martín, M. P., "Turbulence in a hypersonic compression ramp flow," *Physical Review Fluids*, Vol. 6, No. 034601, 2019.

[35] Bookey, P., Wyckham, C., Smits, A. J., and Martin, M. P., "New Experimental Data of STBLI at DNS/LES Accessible Reynolds Number," *AIAA Paper No. 2005-0309*, 2005.

[36] Volpiani, P. S., Bernardini, M., and Larsson, J., "Effectsof a nonadiabatic wall on hypersonic shock/boundary-layer interactions," *Physical Review of Fluids*, Vol. 5, No. 014602, 2020.

[37] Cao, S., Klioutchnikov, I., and Olivier, H., "Görtler Vortices in Hypersonic Flow on Compression Ramps," *AIAA J.*, Vol. 57, No. 9, September 2019.

[38] Chang, E., Chan, W., McIntyre, T., and Veeraragavan, A., "Hypersonic shock impingement on a heated flat plate at Mach 7 flight enthalpy," *Journal of Fluid Mechanics*, Vol. 908, No. R1, 2021.

[39] Rudy, D. H., Thomas, J. L., Kumar, A., Gnoffo, P. A., and Chakravarthy, S. R., "Computational Laminar Hypersonic Compression-Corner Flows," *AIAA J.*, Vol. 29, No. 7, 1991, pp. 1108–1113.

[40] Simeonides, G. and Haase, W., "Experimental and Computational Investigations of Hypersonic Flow about Compression Ramps," *Journal of Fluid Mechanics*, Vol. 283, 1995, pp. 17–42.

[41] Loginov, M. S., Adams, N. A., and Zheltovodov, A. A., "Large-eddy simulation of shock-wave/turbulent-boundary layer interaction," *Journal of Fluid Mechanics*, Vol. 463, 2006, pp. 377–402.

[42] Touber, E. and Sandham, N. D., "Large-eddy simulation of low-frequency unsteadiness in a turbulent shock-induced separation bubble," *Theor. Comput. Fluid Dyn.*, Vol. 23, No. 2, 2009, pp. 79–107.

[43] Hadjadj, A., "Large-Eddy Simulation of Shock/Boundary Layer Interaction," *AIAA J.*, Vol. 50, December 2012, pp. 2919–2927.

[44] Urbin, G. and Knight, D., "Large Eddy Simulation of a Supersonic Boundary Layer Using an Unstructured Grid," *AIAA J.*, Vol. 39, No. 7, July 2001, pp. 1288–1295.

[45] Schreyer, A.-M., Bermejo-Moreno, I., Kim, J., and Urzay, J., "Separation control in a hypersonic compression ramp interaction," *Proc. of Summer Program, CTR Stanford, CA*, 2016.

[46] Kim, J., Bermejo-Moreno, I., Schreyer, A.-M., and Urzay, J., "LES of hypersonic compression-corner flows with upstream sub-boundary-layer microramp vortex generators," *Proc. of Summer Program, CTR Stanford, CA*, 2016.

[47] Vreman, A. W., "An eddy-viscosity subgrid-scale model for turbulent shear flow: Algebraic theory and applications," *Phys. Fluids*, Vol. 16, 2004, pp. 3670–3681.

[48] Schreyer, A.-M., Sahoo, D., and Smits, A., "Turbulence Measurements with PIV in a Hypersonic Shock Boundary Layer Interaction," *AIAA Paper No. 2011-3429*, 2011.

[49] Ritos, K., Kokkinakis, I. W., and Drikakis, D., "Physical insight into a Mach 7.2 compression corner flow," *AIAA Paper No. 2018-1810*, 1810.

[50] Fang, J., Yao, Y., Zheltovodov, A. A., and Lu, L., "Investigation of Three-Dimensional Shock Wave/Turbulent Boundary-Layer Interaction Initiated by a Single Fin," *AIAA J.*, Vol. 55, No. 2, February 2017.

[51] Moin, P., Squires, K., Cabot, W., and Lee, S., "A dynamic subgrid-scale model for compressible turbulence and scalar transport," *Phy. of Fluids*, Vol. 3, 1991, pp. 2746–2757.

[52] Martín, M. P., Piomelli, U., and Candler, G. V., "Subgrid-Scale Models for Compressible Large Eddy Simulations," *Theoretical and Computational Fluid Dynamics*, Vol. 13, 2000, pp. 361–376.

[53] Helm, C. M. and Martín, M. P., "Large Eddy Simulation of Two Separated Hypersonic Shock/Turbulent Boundary Layer Interactions," *Under Review, Physical Review Fluids*, 2021.

[54] Leonard, A., "Energy cascade in large-eddy simulations of turbulent fluid flows," *Advances in Geophysics*, Vol. 18 A, 1974, pp. 237–248.

[55] Hirsch, C., *Numerical Computation of Internal and External Flows*, Wiley, New York, 1991.

[56] Knight, D., Zhou, G., Okong'o, N., and Shukla, V., "Compressible large eddy simulation using unstructured grids," *AIAA Paper 98-0535*, 1998.

[57] Armenio, V., Piomelli, U., and Fiorotto, V., "Applications of a Lagrangian mixed model in generalized coordinates," *Direct and large-eddy simulation III*, 1999, pp. 135–146.

[58] Martín, M. P., Taylor, E. M., Wu, M., and Weirs, V. G., "A bandwidth-optimized WENO scheme for the effective direct numerical simulation of compressible turbulence," *Journal of Computational Physics*, Vol. 220, 2006, pp. 270–289.

[59] Taylor, E. M., Wu, M., and Martín, M. P., "Optimization of nonlinear error for weighted essentially non-oscillatory methods in direct numerical simulation of compressible turbulence," *Journal of Computational Physics*, Vol. 223, 2007, pp. 384–397.

[60] Wu, M. and Martín, M. P., "Direct Numerical Simulation of Supersonic Turbulent Boundary Layer over a Compression Ramp," *AIAA Journal*, Vol. 45, No. 4, 2007, pp. 879–889.

[61] Martín, M. P., "Shock capturing and the LES of high-speed flows," *In Annual Research Briefs, Center for Turbulence Research, NASA Ames/Stanford University*, 2000.

[62] Williamson, J. H., "Low-Storage Runge-Kutta schemes," *Journal of Computational Physics*, Vol. 35, No. 1, 1980, pp. 48–56.

[63] Xu, S. and Martín, M. P., "Assessment of inflow boundary conditions for compressible turbulent boundary layers," *Physics of Fluids*, Vol. 16, No. 7, 2004, pp. 2623–2639.

[64] Keyes, F. G., "A summary of viscosity and heat-conduction data for He, A, H_2, O_2, N_2, CO, CO_2, H_2O, and air," *Transactions of the American Society of Mechanical Engineers*, Vol. 73, No. 7, 1951, pp. 589–596.

[65] Martín, M. P., "Direct numerical simulation of hypersonic turbulent boundary layers. Part 1. Initialization and comparison with experiments," *Journal of Fluid Mechanics*, Vol. 570, 2007, pp. 347–364.

[66] Taylor, G. I., "Production and dissipation of vorticity in a turbulent fluid," 1938.

[67] Settles, G. S., Fitzpatrick, T. J., and Bogdonoff, S. M., "Detailed study of attached and separated compression corner flowfields in high Reynolds number supersonic flow," *AIAA Journal*, Vol. 17, No. 6, 1979, pp. 579–585.

[68] Schülein, E. and Trofimov, V. M., "Steady longitudinal voritces in supersonic turbulent separated flows." .

[69] Back, L. H. and Cuffel, R. F., "Changes in heat transfer from turbulent boundary layers interacting with shock waves and expansion waves," *AIAA Journal*, Vol. 8, No. 10, 1970, pp. 1871–1873.

[70] Wu, M. and Martín, M. P., "Analysis of shock motion in shockwave and turbulent boundary layer interaction using direct numerical simulation data," *Journal of Fluid Mechanics*, Vol. 594, 2008, pp. 71–83.

[71] Pope, S. B., *Turbulent Flows*, Cambridge University Press, 2006.

[72] Lumley, J. L., "Computational modeling of turbulent flows," *Adv. Appl. Mech.*, Vol. 18, 1978.

[73] Duan, L., Beekman, I., and Martín, M. P., "Direct numerical simulation of hypersonic turbulent boundary layers. Part2. Effect of wall temperature," *Journal of Fluid Mechanics*, Vol. 655, 2010, pp. 419–445.

[74] Duan, L., Beekman, I., and Martín, M. P., "Direct numerical simulation of hypersonic turbulent boundary layers. Part 3. Effect of Mach number," *Journal of Fluid Mechanics*, Vol. 672, 2011, pp. 245–267.

[75] Coleman, G. T. and Stollery, J. L., "Heat transfer from hypersonic turbulent flow at a wedge compressvion corner," *Journal of Fluid Mechanics*, Vol. 56, 1972, pp. 741–752.

[76] Morkovin, M. V., *Effects of compressibility on turbulent flows*, CNRS, 1962, pp. 367–380, Mécanique de la Turbulence.

[77] Guarini, S. E., Moser, R. D., Shariff, K., and Wray, A., "Direct numerical simulation of a supersonic turbulent boundary layer at mach 2.5," *Journal of Fluid Mechanics*, Vol. 414, 2000, pp. 1–33.

[78] Maeder, T., Adams, N. A., and Kleiser, L., "Direct simulation of turbulent supersonic boundary layers by and extended temporal approach," *Journal of Fluid Mechanics*, Vol. 429, 2001, pp. 187–364.

[79] Huang, P. G., Coleman, G. N., and Bradshaw, P., "Compressible turbulent channel flows: DNS results and modeling," *Journal of Fluid Mechanics*, Vol. 305, 1995, pp. 185–218.

[80] Gaviglio, J., "Reynolds analogies and experimental study of heat transfer in the supersonic boundary layer," *International Journal of Heat and Mass Transfer*, Vol. 30, 1987, pp. 911–926.

[81] Rubesin, M. W., "Extra compressibility terms for Favre-averaged two-equation models of inhomogeneous turbulent flows," *NASA CR-177556*, 1990.

[82] Bardina, J., Ferziger, J. H., and Reynolds, W. C., "Improved subgrid-scale models for large eddy simulation," *AIAA Paper No. 80-1357*, 1980.

[83] Helm, C. M., Martín, M. P., and Williams, O. J. H., "Characterization of the shear layer in separated shock/turbulent boundary layer interactions," *Journal of Fluid Mechanics*, 2021.

[84] Dupont, P., Piponniau, S., Sidorenko, A., and Debiève, J. F., "Investigation by Particle Image Velocimetry Measurements of Oblique Shock Reflection with Separation," *AIAA J.*, Vol. 46, No. 6, 2008, pp. 1365–1370.

[85] Ganapathisubramani, B., Clemens, N. T., and Dolling, D. S., "Effects of upstream boundary layer on the unsteadiness of shock-induced separation," *Journal of Fluid Mechanics*, Vol. 585, 2007, pp. 369–394.

[86] Theofilis, V., Hein, S., and Dallmann, U., "On the origins of unsteadiness and three-dimensionality in a laminar separation bubble," *Philos. Trans. R. Soc. Lond.* A 358:3229-46, 2000.

[87] Rodriquez, D. and Theofilis, V., "Structural changes of laminar separation bubbles induced by global linear instability," *Journal of Fluid Mechanics*, Vol. 655, 2010, pp. 280–305.

[88] Rodriguez, D. and Theofilis, V., "On the birth of stall cells on airfoils," *Theoretical and Computational Fluid Dynamics*, Vol. 25, No. 1–4, 2011, pp. 105–117.

[89] Floryan, J. M., "On the Görtler instability of boundary layer," *Progress in Aerospace Science*, Vol. 28, 1991, pp. 235–271.

[90] Helm, C. M. and Martín, M. P., "On the Scaling of Hypersonic Shock/Turbulent Boundary Layer Interactions," *Accepted, Physical Review Fluids*, 2021.

[91] Chapman, D. R., Kuehn, D. M., and Larson, H. K., "Investigation of Separated Flows in Supersonic and Subsonic Streams with Emphasis on the Effect of Transition," *NACA, Rept. 1356*, 1958.

[92] Spaid, F. W. and Frishett, J. C., "Incipient Separation of a Supersonic, Turbulent Boundary Layer, Including Effect of Heat Transfer," *AIAA Journal*, Vol. 10, No. 7, July 1972, pp. 915–922.

[93] Volpiani, P. S., Bernardini, M., and Larsson, J., "Effects of a nonadiabatic wall on supersonic shock/boundary-layer interactions," *Physical Review of Fluids*, Vol. 3, 2018.

[94] Coleman, G. T., "Hypersonic Turbulent Boundary Layer Studies," *PhD thesis, Univ. of London*, 1973.

[95] Brooks, J., Gupta, A. K., Helm, C., Martín, M. P., Smith, M., and E., M., "Mach 10 PIV Flow Field Measurements of a Turbulent Boundary Layer and Shock Turbulent Boundary Layer Interaction," *AIAA Paper No. 2017-3325*, 2017.

[96] Sims, J. L., "Tables for supersonic flow around right circular cones at zero angle of attack," *NASA Technical Report, NASA-SP-3004*, 1964.

[97] Hopkins, E. J. and Inouye, M., "An Evaluation of Theories for Predicting Turbulent Skin Friction and Heat Transfer on Flat Plates at Supersonic and Hypersonic Mach Numbers," *AIAA Journal*, Vol. 9, No. 6, June 1971, pp. 993–1003.

[98] Elfstrom, G. M., "Turbulent Separation in Hypersonic Flow," *PhD thesis, Univ. of London*, 1971.

[99] van Driest, E. R., "The problem of aerodynamic heating," *Aeronautical Engineering Review*, Vol. 15, No. 10, 1956, pp. 26–41.

[100] Korst, H. H. and Tripp, W., "The pressure on a blunt trailing edge separating two-supersonic two-dimensional air streams of different Mach numbers and stagnation pressures but identical stagnation temperatures," *Fifth Midwestern Conference on Fluid Mechanics*, University of Michigan Press, Ann Arbor, Michigan, 1957.

[101] Channapragada, R. S., "Compressible Jet Spread Parameter for Mixing Zone Analyses," *AIAA J.*, Vol. 1, No. 9, September 1963.

[102] Lin, C. C., *NACA Tech. Note*, 1953, 2887.

[103] Pai, S. I., "On Turbulent Jet Mixing of Two Gases at Constant Temperature," *J. Applied Mech.*, Vol. 22, 1955.

[104] Miles, J. W., "The Stability of a Shear Layer in an Unbounded Heterogenous Inviscid Fluid," *J. Fluid Mech.*, Vol. 6, 1959, pp. 538–522.

[105] Birch, S. F. and Eggers, J. M., "Free turbulent shear flows," *NASA Rep.*, 1972, SP-321.

[106] Kline, S. J., Cantwell, B. J., and Lilley, G. M., *Proc. 1980 Conf. on Complex Turbulent Flows, Vol. I*, Stanford University, 1980, pp. 364–366.

[107] Bogdanoff, D. W., "Compressibility Effects in Turbulent Shear Layers," *AIAA J.*, Vol. 21, No. 6, 1983, pp. 926–927.

[108] Chinzei, N., Masuya, G., Komuro, T., Murakami, A., and Kudou, K., "Spreading of two-stream supersonic turbulent mixing layers," *Phys. Fluids*, Vol. 29, 1986, pp. 1345–1347.

[109] Papamoschou, D. and Roshko, A., "The compressible turbulent shear layer: an experimental study," *J. Fluid Mech.*, Vol. 197, 1988, pp. 453–477.

[110] Ikawa, H. and Kubota, T., "Investigation of supersonic turbulent mixing layer with zero pressure gradient," *AIAA J.*, Vol. 13, No. 5, 1975, pp. 566–572.

[111] Elliott, G. S. and Samimy, M., "Compressibility effects in free shear layers," *Phys. Fluids A*, Vol. 2, 1990, pp. 1231–1240.

[112] Goebel, S. G. and Dutton, J. C., "Experimental study of compressible turbulent mixing layers," *AIAA J.*, Vol. 29, No. 4, 1991, pp. 538–546.

[113] Dimotakis, P. E., "Turbulent free shear layer mixing and combustion," Vol. 137, 1991, pp. 265–340.

[114] Lele, S. K., "Compressibility Effects on Turbulence," *Annu. Rev. of Fluid Mech.*, Vol. 26, 1994, pp. 211–54.

[115] Gatski, T. B. and Bonnet, J.-P., "Compressibility, Turbulence and High Speed Flow," *Elsevier*, 2013, pp. 169–229.

[116] Slessor, M. D., Zhuang, M., and Dimotakis, P. E., "Turbulent shear-layer mixing; growth-rate compressibility scaling," *J. Fluid Mech.*, Vol. 414, 2000, pp. 35–45.

[117] Aupoix, B., "Modeling of compressibility effects in mixing layers," *J. Turbulence*, Vol. 5, 2004.

[118] Aupoix, B. and Bézard, H., "Compressible mixing layers: Data analysis and modeling," *ERCOFTAC Bulletin*, Vol. 70, September 2006, pp. 13–17.

[119] Barone, M. F., Oberkampf, W. L., and Blottner, F. G., "Validation case study: Prediction of compressible turbulent mixing layer growth rate," *AIAA J.*, Vol. 44, No. 7, 2006, pp. 1488–1497.

[120] Samimy, M. and Elliott, G. S., "Effects of compressibility on the characteristics of free shear flow," *AIAA J.*, Vol. 28, No. 3, 1990, pp. 439–445.

[121] Barre, S., Quine, C., and Dussauge, J., "Compressibility effects on the structure of supersonic mixing layers: e xperimental results," *J. Fluid Mech.*, Vol. 259, 1994, pp. 47–78.

[122] Debisschop, J.-R., Chambres, O., and Bonnet, J.-P., "Velocity field characteristics in supersonic mixing layers," *Exp. Thermal and Fluid Sci.*, Vol. 9, 1994, pp. 147–155.

[123] Pantano, C. and Sarkar, S., "A study of compressibility effects in the high-speed turbulent shear layer using direct numerical simulation," *J. Fluid Mech.*, Vol. 451, 2002, pp. 329–371.

[124] Gruber, M. R., Messersmith, N. L., and Dutton, J. C., "Three-dimensional velocity field in a compressible mixing layer," *AIAA J.*, Vol. 31, No. 11, 1993, pp. 2061–2067.

[125] Freund, J. B., Lele, S. K., and Moin, P., "Compressibility effects in a turbulent annular mixing layer. Part 1. Turbulence and growth rate," *J. Fluid Mech.*, Vol. 421, 2000, pp. 229–267.

[126] Barre, S. and Bonnet, J.-P., "Detailed experimental study of a highly compressible supersonic turbulent plane mixing layer and comparison with most recent DNS results: "Towards an accurate description of compressibility effects in supersonic free shear flows"," *Int. J. Heat and Fluid Flow*, Vol. 51, 2015, pp. 324–334.

[127] Samimy, M., Reeder, M. F., and Elliott, G. S., "Compressibility effects on large structures in free shear flows," *Phys. Fluids A*, Vol. 4, No. 6, June 1992, pp. 1251–1258.

[128] Clemens, N. T. and Mungal, M. G., "Two- and Three-Dimensional Effects in the Supersonic Mixing Layer," *AIAA J.*, Vol. 30, No. 4, April 1992, pp. 973–981.

[129] Clemens, N. T. and Mungal, M. G., "Large-scale structure and entrainment in the supersonic mixing layer," *J. Fluid Mech.*, Vol. 284, 1995, pp. 171–216.

[130] Rossmann, T., Mungal, M. G., and Hanson, R. K., "Evolution and growth of large-scale structures in high compressibility mixing layers," *J. Turbulence*, Vol. 3, 2002.

[131] Sandham, N. D. and Reynolds, W. C., "Thee-dimensional simulation of large eddies in the compressible mixing layer," *J. Fluid Mech.*, Vol. 224, 1991, pp. 133–158.

[132] Day, M. J., Reynolds, W. C., and Mansour, N. N., "The structure of the compressible reacting mixing layer: Insights from linear stability analysis," *Phys. Fluids*, Vol. 10, 1998, pp. 993–1007.

[133] Kourta, A. and Sauvage, R., "Computaion of supersonic mixing layers," Vol. 14, No. 11, 2002, pp. 3790–3797.

[134] Sandham, N. D. and Reynolds, W. C., "Compressible Mixing Layer: Linear Theory and Direct Simulation," 1990.

[135] Papamoschou, D., "Evidence of shocklets in a counterflow supersonic shear layer," *Phys. Fluids*, Vol. 7, 1995, pp. 233–235.

[136] Lele, S. K., "Direct numerical simulation of compressible free shear flows," *AIAA Paper*, 1989, 89-0374.

[137] Vreman, A. W., Sandham, N. D., and Luo, K. H., "Compressible mixing layer growth rate and turbulence characteristics," *J. Fluid Mech.*, Vol. 320, 1996, pp. 235–258.

[138] Breidenthal, R. E., "Sonic eddy–a model for compressible turbulence," *AIAA J.*, Vol. 30, No. 1, 1992, pp. 101–104.

[139] Strykowski, P. J., Krothapalli, A., and Jendoubi, S., "The effect of counterflow on the development of compressible shear layers," *J. Fluid Mech.*, Vol. 308, 1996, pp. 63–96.

[140] Huerre, P. and Monkewitz, P. A., "Absolute and convective instabilities in free shear layers," *J. Fluid Mech.*, Vol. 159, 1985, pp. 151–168.

[141] Pavithran, S. and Redekopp, L. G., "The absolute-convective transition in subsonic mixing layers," *Phys. Fluids A*, Vol. 1, 1989, pp. 1736–1739.

[142] Jackson, T. L. and Grosch, C. E., "Absolute/convective instabilities and the convective Mach number in a compressible mixing layer," *Phys. Fluids A*, Vol. 2, 1990, pp. 949.

[143] Dupont, P., Piponniau, S., and Dussauge, J. P., "Compressible mixing layer in shock-induced separation," *J. Fluid Mech.*, Vol. 863, 2019, pp. 620–643.

[144] Dupont, P., Muscat, P., and Dussauge, J.-P., "Localisation of large scale structures in a supersonic mixing layer: A new method and first analysis," *Flow Turbulence and Combustion*, Vol. 62, 1999, pp. 335–358.

[145] Thurow, B. S., Jiang, N., Kim, J.-W., Lempert, W., and Samimy, M., "Issues with measurements of convective velocity of large-scale structures in the compressible shear layer of a free jet," *Phys. Fluids*, Vol. 20, 2008.

[146] Tennekes, H. and Lumley, J. L., *A First Course in Turbulence*, The MIT Press, 1972.

[147] Lesieur, M., *Turbulence in Fluids*, Marinus Nijhoff Publishers, Dordrecht, The Netherlands, 1987.

[148] White, F. M., *Viscous Fluid Flow*, McGraw–Hill, 1974.

[149] Mehta, R. D. and Westphal, R. V., "Near-Field Turbulence Properties of Single- and Two-Stream Plane Mixing Layers," *AIAA Paper*, 1984, 1984-0426.

[150] Forliti, D. J., Tang, A. B., and Strykowski, P. J., "An experimental investigation of planar countercurrent turbulent shear layers," *J. Fluid Mech.*, Vol. 530, 2005, pp. 479–486.

[151] König, O., Schulülter, J., and Fiedler, H. E., "Turbulent mixing layer in adverse pressure gradient," *Progress in fluid flow research: Turbulence and applied MHD*, 1998, pp. 15–29.

[152] Kiya, M. and Sasaki, K., "Structure of a turbulent separation bubble," *J. Fluid Mech.*, Vol. 137, 1983, pp. 83–113.

[153] Cherry, N. J., Hillier, R., and Latour, M. E. M. P., "Unsteady measurements in a separated and reattaching flow," *J. Fluid Mech.*, Vol. 144, 1984, pp. 13–46.

[154] Brown, G. L. and Thomas, A. S. W., "Large structure in a turbulent boundary layer," *Phys. Fluids*, Vol. 20, No. 10, 1977.

[155] Graftieaux, L., Michard, M., and Grosjean, N., "Combining PIV, POD and vortex identification algorithms for the study of unsteady turbulent swirling flows," *Measurement Science and Technology*, Vol. 12, 2001, pp. 1422–1429.

[156] Brown, G. L. and Roshko, A., "On the density effects and large structures in turbulent mixing layers," *J. Fluid Mech.*, Vol. 64, 1974, pp. 775–781.